DISCLAIMER

Pacific Northwest
NATIONAL LABORATORY

PNNL-38301

Performance Evaluation of LPBF Manufactured 316H Components

M3CT-25PN1307041

September 2025

CJ Taylor Mason,
Subhashish Meher
James Fitzpatrick
Nathan Barrett
Daniel Yoon
Ankit Roy
Pratikshya Meher
Robert Montgomery
Chris Hutchinson
Isabella van Rooyen

U.S. DEPARTMENT OF ENERGY

Prepared for the U.S. Department of Energy
under Contract DE-AC05-76RL01830

DISCLAIMER

PACIFIC NORTHWEST NATIONAL LABORATORY
operated by
BATTELLE
for the
UNITED STATES DEPARTMENT OF ENERGY
under Contract DE-AC05-76RL01830

Printed in the United States of America

Available to DOE and DOE contractors from
the Office of Scientific and Technical Information,
P.O. Box 62, Oak Ridge, TN 37831-0062
www.osti.gov
ph: (865) 576-8401
fox: (865) 576-5728
email: reports@osti.gov

Available to the public from the National Technical Information Service
5301 Shawnee Rd., Alexandria, VA 22312
ph: (800) 553-NTIS (6847)
or (703) 605-6000
email: info@ntis.gov
Online ordering: http://www.ntis.gov

PNNL-38301

Performance Evaluation of LPBF Manufactured 316H Components

M3CT-25PN1307041

September 2025

CJ Taylor Mason,
Subhashish Meher
James Fitzpatrick
Nathan Barrett
Daniel Yoon
Ankit Roy
Pratikshya Meher
Robert Montgomery
Chris Hutchinson
Isabella van Rooyen

Prepared for
the U.S. Department of Energy
under Contract DE-AC05-76RL01830

Pacific Northwest National Laboratory
Richland, Washington 99354

Summary

This work represents the continuation of a benchmark study that includes modeling, fabrication and characterization as demonstration to support industry's adoption of advanced manufacturing processes in a variety of structures. This comprehensive study investigated the feasibility of using additive manufacturing (AM) technologies, specifically laser powder direct energy deposition (LP-DED) and laser powder bed fusion (LPBF), to produce complex nuclear microreactor components using 316H stainless steel. The research focused on manufacturing an expanded elbow pipe component with transitioning sections, which are traditionally difficult and costly to produce through conventional manufacturing methods. The overall study's primary objectives are therefore demonstrating AM viability for nuclear applications, optimizing process parameters, developing comprehensive material characterization protocols, validating computational modeling approaches, and establishing manufacturing guidelines for complex geometries. Although the initial work included the phased approach of cubical, upscaled cylindrical components, it will contribute towards the knowledge required for the printing of the expanded elbow structure.

The project achieved significant progress in process development by successfully optimizing LP-DED parameters to achieve 99.16–99.97% relative density in 316H stainless-steel components. Through systematic evaluation of sixteen cube samples with varied laser powers (400-700W) and scan speeds (600-900 mm/min), optimal processing windows were identified at 500-550W with 600-700 mm/min or 650–700W with 650–900 mm/min scan speeds. The DED-manufactured 316H demonstrated mechanical properties comparable or superior to wrought materials, with Young's moduli ranging from 153–208 GPa.

Advanced characterization protocols were established using multiple non-destructive evaluation techniques, including ultrasonic testing for elastic property determination, X-ray diffraction for comprehensive residual stress analysis revealing both compressive (up to -47.6 MPa) and tensile stresses (up to +19.2 MPa), and X-ray computed tomography for detailed porosity assessment achieving greater than 99% density validation. The research also developed computational validation capabilities through Flow-3D simulations coupled with machine learning correction models that achieved prediction accuracy below 1% error for porosity estimation, enabling predictive manufacturing approaches that can reduce experimental iteration cycles.

Although multiple components were fabricated using LP-DED and LPBF, which showed already substantial demonstration for industry application, the full comparative matrixes were not yet completed and are planned during the next fiscal year. A Pacific Northwest National Laboratory sponsored 316L wire DED large cylinder was also fabricated using 800 W laser power and 16.8 mm/s wire feed rates to initiate a third manufacturing process for future evaluation and comparison. For LPBF applications, support structure optimization addressed critical manufacturing challenges by reducing build times from 349 to 142 hours while maintaining component integrity, achieved through strategic refinement of support diameter, spacing, and density parameters. The expanded elbow pipe component, though scaled to 40% full size due to equipment limitations, successfully demonstrated proof of concept for complex geometry manufacturing with applications across thirteen identified micro-reactor designs. The characterization and mechanical performance of this LPBF extended elbow will be further determined in the next fiscal year.

The technical impact of this research provides nuclear industry stakeholders already with AM manufacturing options that offer reduced costs, improved design flexibility, and enhanced material utilization compared to traditional manufacturing methods. Furthermore, the international Generation IV Advanced manufacturing and materials engineering working group activities will stimulate global research in this field, during which more data will be generated and shared amongst member countries. The established process parameters, comprehensive characterization protocols, and computational modeling tools enable accelerated qualification pathways for nuclear applications while supporting implementation across diverse microreactor designs with demonstrated scalability from laboratory specimens to functional component sizes. This work significantly advances the Advanced Materials and Manufacturing Technologies program's mission by providing industry-ready manufacturing solutions, contributing to international benchmarking efforts, and establishing technical foundations for nuclear AM qualification standards, ultimately supporting the development and deployment of next-generation nuclear energy systems with reduced timelines and cost structures.

Acknowledgments

The research presented here was supported by the Advanced Materials and Manufacturing Technology program of the U.S. Department of Energy (DOE) Office of Nuclear Energy. Pacific Northwest National Laboratory is a multi-program national laboratory operated for the DOE by Battelle Memorial Institute under Contract No. DE-AC05-76RL01830. Professor Xiao Lou and Qianwen Zhang from Purdue University are acknowledged for printing the 316H stainless-steel Laser Powder Direct Energy Deposition (LP-DED) component series and the Laser Powder Bed Fusion 40%-sized extended elbow component and for developing and measuring the residual stresses through etched features for the cylindrical LP-DED component. Wire DED fabrication of the 316H stainless-steel cylinder was completed by Tanner Covert and Joseph Gill at the Pacific Northwest National Laboratory machine shop. Cary Counts is thanked for his editorial review of this report. Dr Lei Li is thanked for his technical review of the report contents.

Acronyms and Abbreviations

AMMT	Advanced Materials and Manufacturing Technologies
AMME WG	Generation IV International Forum Advanced Manufacturing Materials Engineering Working Group
AM	Advanced Manufacturing
ANL	Argonne National Laboratory
MARVEL	Microreactor Application Research, Validation and Evaluation Project
DED	directed energy deposition
DIC	digital image correlation
EBSD	electron backscattering diffraction
EDM	electron discharge machining
FEA	finite element analysis
FFT	Fast Fourier Transform
FY	fiscal year
GIF	Generation IV International Forum
INL	Idaho National Laboratory
ID	inner diameter
KAM	kernel average misorientation
LANL	Los Alamos National Laboratory
LPBF	laser powder bed fusion
MSR	molten-salt reactors
NDE	nondestructive evaluation
OD	outer diameter
PNNL	Pacific Northwest National Laboratory
SEM	scanning electron microscopy
SLM	selective laser melting
SS	stainless steel

Contents

Figures

Tables

1 Introduction

This report is a status update for fiscal year (FY) 2025 work relative to Benchmark Study Matrix for Microreactor Geometries Relevant to Multiple Developers for the Advanced Materials and Manufacturing Technologies (AMMT) Program.

This task is a continuation of the manufacturing, characterization, and demonstration of selected samples of the component geometry complexity series leading to the fabrication of an agnostic microreactor component identified during the FY24 benchmark study. The series of components will demonstrate comparative fabrication properties between different geometries of laser powder bed fusion (LPBF) 316H stainless-steel (SS). A detailed introduction, technical background, and results from last year's work are included in last year's end-of-year reports and are not presented in this brief update (van Rooyen et al. 2024). The design of the agnostic extended elbow component, although completed in FY24, is expanded below to emphasize the rational and applicability of this design for future use by industry.

The overall objective of the collaborative project is shown in Figure 1 with the specific scope for FY25 shown in Figure 2.

	Cube	Solid Disk	Tube/ Small Diameter	Large Diameter Cylinder	PNNL Non-Proprietary Design: Mockup	Full Scale Micro Reactor Heat Exchange Liner
316H (Powder DED)	Completed	Completed	Completed	Completed	Future	N/A
316H (LPBF)	Print completed	FY26	FY26	FY26	Print Completed	N/A
316L (Wire DED)	N/A	N/A	N/A	Completed (training model)	Future work	FY26
316H (Wire DED)	Future work	Future work	Future work	Future work	Future work	Future work

Additionally, 316L (LPBF) work can be carried out with international collaborators.

Figure 1. Matrix outlining the manufacturing schedule to demonstrate powder directed energy deposition (DED) geometry complexity

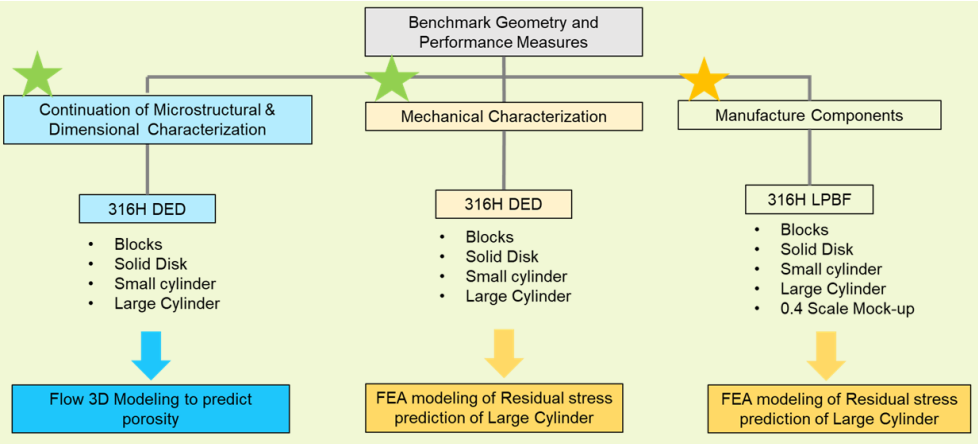

Figure 2. Schematic presentation of the work performed in FY25 and reported in this document. The yellow star indicates that although various geometries were initially planned, this task will continue in FY26 as only the blocks and 0.4 extended elbow component were manufactured.

A matrix of five microreactor component geometries—including small cube samples, small disks, small cylinder, large cylinder, and a non-proprietary mock-up component—was proposed as benchmarking geometry components. Figure 3 shows schematically the part dimensions for the demonstration matrix. This project proposed using an expanded pipe that leads into an elbow as the non-proprietary mock-up design. This component is extremely difficult and costly to manufacture through traditional methods, and it also can reduce the space needed for traditional transition areas. The powder DED technique was identified as the technique for the FY24 benchmark study and preliminary analysis was conducted on 316H SS cube samples and the large 316L SS cylinder (van Rooyen et al. 2024).

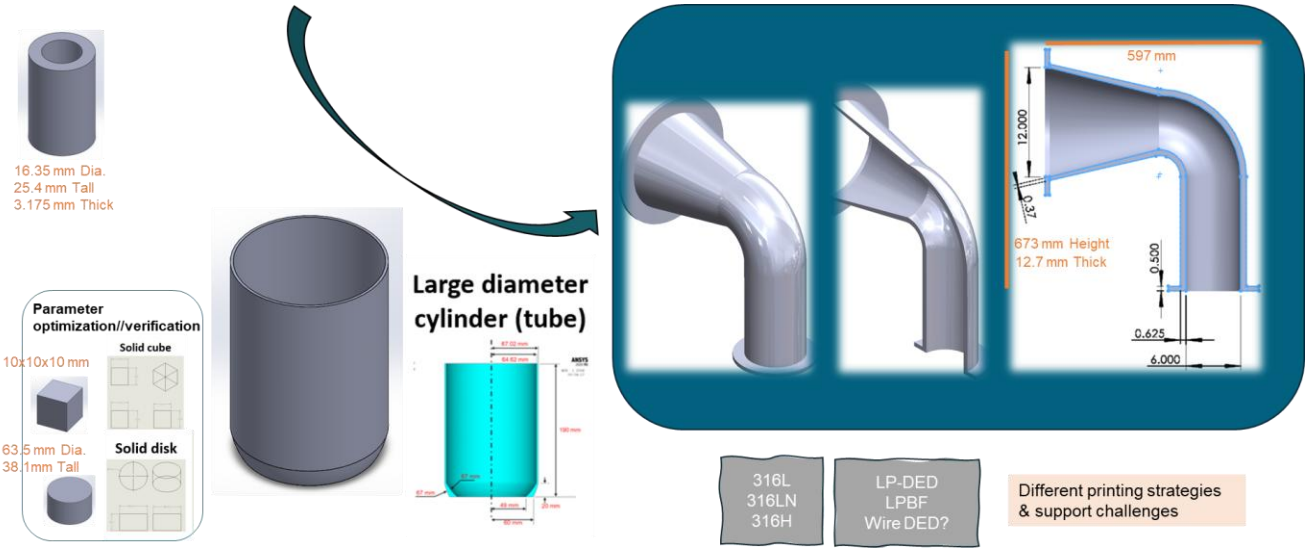

Figure 3. Schematic presentation of the different geometries considered for the benchmark matrix and the scale-up dimensions

A finite element model to predict residual stress in DED fabricated components was developed in Ansys. The finite element model used a thermal model that then informed the structural model. Because experimental process parameters were unknown, two different build patterns were investigated using assumed build parameters.

Specifically, the work in FY25 focused on a second manufacturing material combination relevant to the industry and is aligned with the AMMT program's qualification effort namely LPBF of 316H SS. As this material-manufacturing (LPBF-316H) combination has been studied in prior years in the AMMT program, more focus will be given to geometrical, dimensional and residual stress and performance consistency. The LPBF powder was co-purchased with the other qualification activities and therefore initially held back to determine the specific size and oxygen level requirements and to ensure that the funds available cover all the needs for all projects. This scheduling approach therefore limited the LPBF manufacturing time and choices during this fiscal year to only the small blocks and the 40% sized extended elbow component. The choice to fabricate this elbow component prior to the cylinder was strategically influenced by lessons-learned during method development for residual stresses determination and the possible iterations that will be needed based on the support structures for the larger-scale extended elbow component. The timeline for full completion of the benchmark matrix is a function of external international collaboration and each member country's contribution.

Following is a brief overview of the designed agnostic additive manufacturing (AM) component for use in conceptual microreactors.

Microreactors are compact nuclear reactors small enough to transport via ground transportation methods, like shipping containers, that enable them to be used in remote or underdeveloped areas. Development of these microreactors provides a unique opportunity for the application of AM technologies, such as DED, to manufacture reactor components. Descriptions of several microreactors that are currently in development are provided in Table 1. Because of the small size constraints for these microreactor designs, it is crucial that all available space is optimally used. This makes AM technologies like DED, prime candidates to produce complex parts at reduced costs and materials compared to traditional manufacturing methods. This project aims to select a common microreactor component that is traditionally costly and difficult to make to be manufactured through DED.

Table 1. Microreactor concepts that potentially can use the expanded elbow

Developer	Reactor Name	Type	Fuel	Coolant	Moderator
Aalo Atomics	Aalo One	STR	U-Zr-H	Sodium	H
Alpha Tech Research Corp	ARC Nuclear Generator	MSR	LEU	Fluoride salt	Not Provided
Antares Industries	R1	Heat Pipe	TRISO	Sodium	Graphite
BWXT	BANR	HTGR	TRISO	Helium	Graphite
General Atomics	GA Micro	HTGR		gas	Not Provided
HolosGen	HolosQuad	HTGR	TRISO	Helium/CO2	Not Provided
Micro Nuclear, LLC	Micro Scale Nuclear Battery	MSR/heat pipe	UF4	FLiBe	YH
Nano Nuclear	Zeus/Odin	HTGR/MSR	UO2	Helium	Not Provided
NuGen, LLC	NuGen Engine	HTGR	TRISO	Helium	Not Provided
NuScale Power	NuScale Microreactor	LMTM/heat pipe	metallic	Liquid Metal	Liquid Metal
Radiant Nuclear	Kaleidos Battery	HTGR	TRISO	Helium	Graphite
Westinghouse	eVINCI	heat pipe	TRISO	Sodium	Graphite
X-Energy	XE-MOBILE	HTGR	TRISO	Helium	Graphite

Previous effort was made to determine a prime design candidate to be replaced with additively manufactured DED component based on several factors including industry interest level, applicability, and difficulty manufacture via traditional manufacturing methods. This project proposes that the selected component to be an expanded pipe that leads into an elbow, shown in Figure 4. This component is not only extremely difficult and costly to manufacture through traditional methods; it also can reduce space needed for traditional transition areas. This design allows for a smooth transition from a larger pipe to a smaller pipe at the location of a 90° bend and has potential to increase fluid flow and reduce turbulence. Thus, the expanded elbow pipe is an excellent candidate for demonstrating the ability to use DED for manufacturing microreactor components.

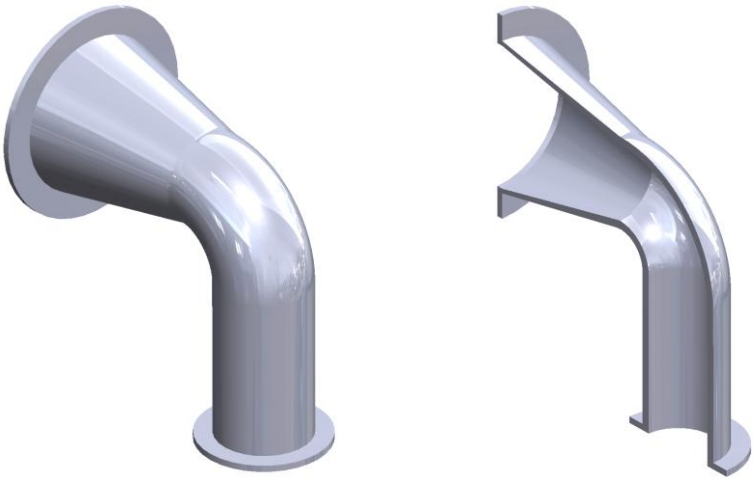

Figure 4. Draft Schematic of Expanded Elbow Pipe

Although there are not publicly available microreactor design schematics, one can infer the sizing for the parts. Standard shipping containers are 8 × 8.5 × 20 feet. Thus, it is reasonable to assume that the max pipe diameter would be 2 feet in diameter, with most of the piping being 1 foot in diameter and smaller. It is proposed that the approximate dimensions for the expanded elbow pipe have a 1-foot inner diameter (ID) at the larger end with 0.375 inch wall thickness, and a 6-inch ID, 0.625- inch wall thickness at the smaller end. The proposed approximate flange size is 16-inch outer diameter (OD) at the larger end and 10-inch OD at the smaller end, with flange thicknesses of 0.5 inch. These dimensions are simply realistic placeholders that can easily be changed to fit various microreactor design needs.

Because of equipment limitations at the time this report was prepared, a smaller scale expanded elbow has been designed based on these original dimensions. This component is scaled down to 40% of the original design, with dimensions reduced by a factor of exactly 0.4. While this does not result in diameters that are identical to current standard pipe sizes, this smaller scale component still provides proof of concept for 5-inch ID and 2.5-inch ID piping that could easily still be used in the microreactors listed in Table 1. The full size and 0.4 scale dimensions are described in Figure 5 and Table 2.

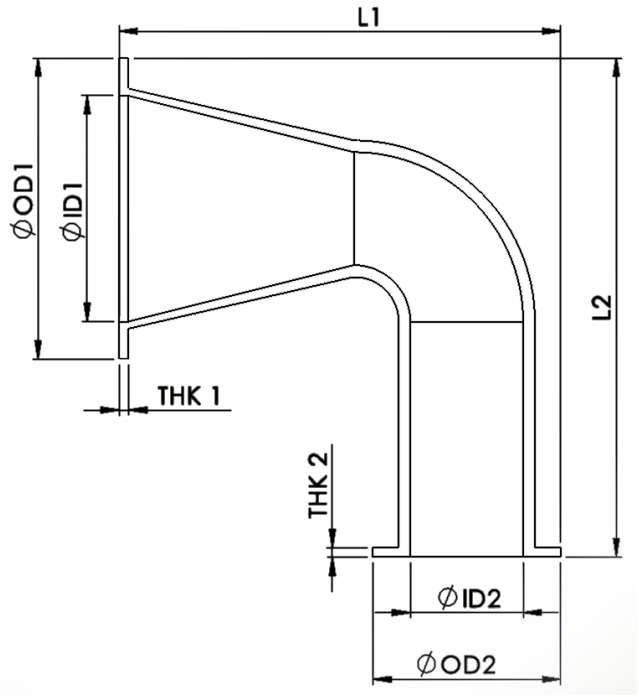

Figure 5. Dimensional labels for the expanded elbow component

Table 2. Expanded elbow dimensions for full size and 0.4 scale components

Dimension Label	Full Size Nominal Dimension (mm)	0.4 Scale Nominal Dimension (mm)
ØOD1	16.0 (406.4)	6.4 (162.6)
ØID1	12.0 (304.8)	4.8 (121.9)
ØOD2	10.0 (254.0)	4.0 (101.6)
ØID2	6.0 (152.4)	2.4 (61.0)
L1	23.5 (673.1)	9.4 (269.2)
L2	26.5 (596.9)	10.6 (238.8)
THK 1	0.5 (12.7)	0.2 (5.1)
THK 2	0.5 (12.7)	0.2 (5.1)

2 316H LP-DED Component Analysis

During FY24, various 316H LP-DED components were fabricated as shown in Figure 6 to Figure 8 and the respective characterization of these parts are shown in subsequent subsections.

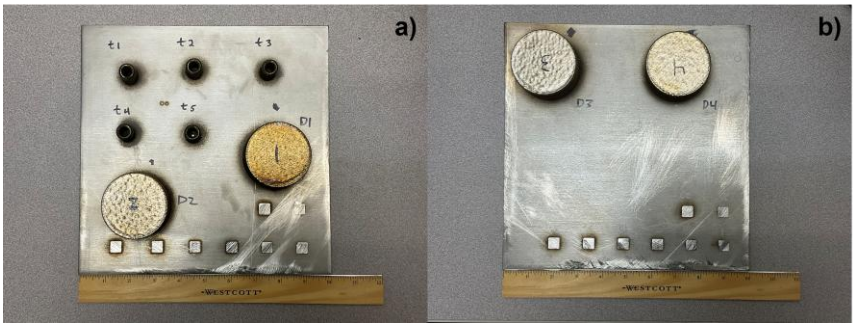

Figure 6. a) Top view of five 316H DED printed small tubes and two 316H DED printed disks. a) Top view of two additional 316H DED printed disks.

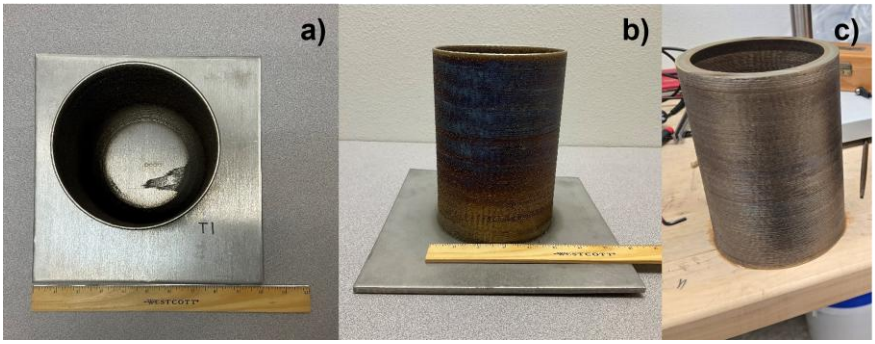

Figure 7. a) Top view of the 316H DED printed large cylinder attached to build plate. a) Side view of the large cylinder attached to the build plate. c) Semi-iso view of the large cylinder machined from the build plate.

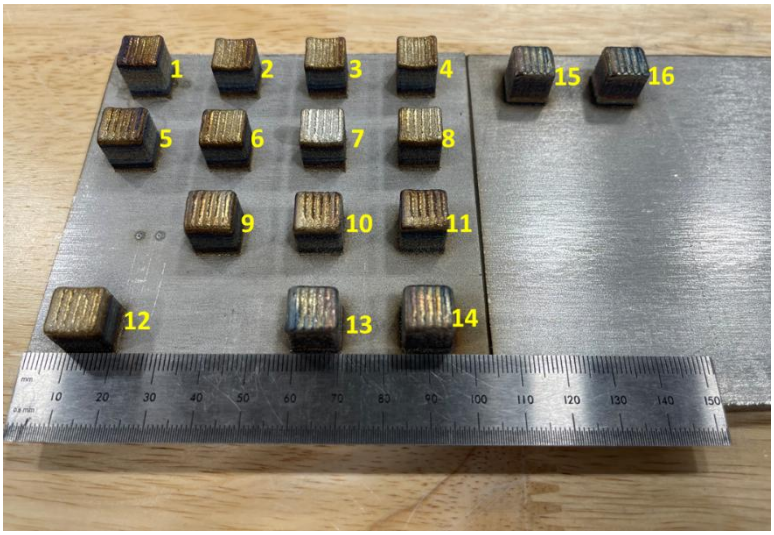

Figure 8. 16 individually DED-fabricated cubes of 316H SS

2.1 SS316H DED Cube Characterization

Additive manufacturing part structural density and porosity can be a critical parameter for nuclear component performance. Moreover, investigations into 316H SS DED are lacking in established qualification metrics. Many reports of academic research exist on optical microscopic image analysis (e.g., optical density), X-ray computer tomography (XCT), and Archimedes' method (Westphal and Seitz 2025). These methods impact the ability to directly or indirectly measure the pore size range, resolution, accuracy, and destructive/non-destructive nature. In this section, we highlight such methods in detail, as well as the benefits and limitations each method has. In the previous FY24 report, 16 316H SS cube samples (Figure 8) were fabricated using the process parameters provided in Table 3.

Table 3. AM processing parameters used to fabricate 316H SS cube samples in this study

Sample	Power (W)	Scan Speed (mm/min)	Hatch spacing (mm)	Relative Density (%)
1	400	600	0.9	99.668
2	400	700	0.9	99.160
3	400	800	0.9	99.591
4	400	900	0.9	99.599
5	500	600	0.9	99.958
6	500	700	0.9	99.960
7	500	800	0.9	99.900
8	500	900	0.9	99.555
9	600	600	0.9	99.880
10	600	700	0.9	99.918
11	600	800	0.9	99.904
12	600	900	0.9	99.938
13	700	600	0.9	99.936
14	700	700	0.9	99.970
15	700	800	0.9	99.962
16	700	900	0.9	99.668

Evaluating the relative density values during optical images, the 500 W and 700 W laser power yields >99.8% relative density. It can be inferred that laser power impacts relative density to a greater extent than scan speed (Sharma et al. 2024). Based on relative density values, either 500–550 W and 600–700 mm/min or 650–700 W and 650–900 mm/min as initial parameter sets, can be used as a baseline. In short, the plot can be used to identify which process parameter set to be used to print parts with optimized density and microstructure. However, further process parameter optimization may be required (e.g., laser beam diameter, powder flow rate, powder particle size, etc.) (Jardon et al. 2021). As evidenced, a large sample set is required to get a refined view to see where deviations occur. A suggestion would be to implement machine-learning (ML) techniques to use existing experimental results as training data to run and optimize it further (Xiao et al. 2025; Lim et al. 2021).

2.1.1 Non-Destructive Evaluation (NDE) using Archimedes' Principle and Ultrasonics

316H SS powder density was calculated using the 316H chemical composition profile by taking the sum of the individual chemical element percentages multiplied by their known densities (Table 4). Density is ~7.906 g/cm^3. This density is compared to the Archimedes' density and relative density (Table 4). The density measurements of the cubes used the Archimedes' method with water. The densities measurements were repeated 10 times for each cube, and the reported values are the linear average of the 10 measurements. The standard deviation for each sample was less than 0.2% with most less than 0.1%.

Table 4. 316H SS chemical composition (Linde, formerly Praxair)

	C	Cr	Fe	Mn	Mo	N	Ni	O	P	S	Si
316H	0.05	17.0	66.72	1.07	2.50	0.01	12.1	0.03	0.006	0.00	0.48

The elastic mechanical properties of the material coupons were obtained by measuring the longitudinal and shear velocities using ultrasonic methods. Because of the coupons size, the elastic mechanical properties were obtained in a single direction/dimension that afforded the ability to measure the ultrasonic velocities. The surface area of the coupon limited the examinations to the sides large enough to accommodate the ultrasonic probes. Generally, the longitudinal velocities were measured perpendicular to the build direction. Two shear velocities (parallel and perpendicular to the build direction) were measured as shown in Figure 9.

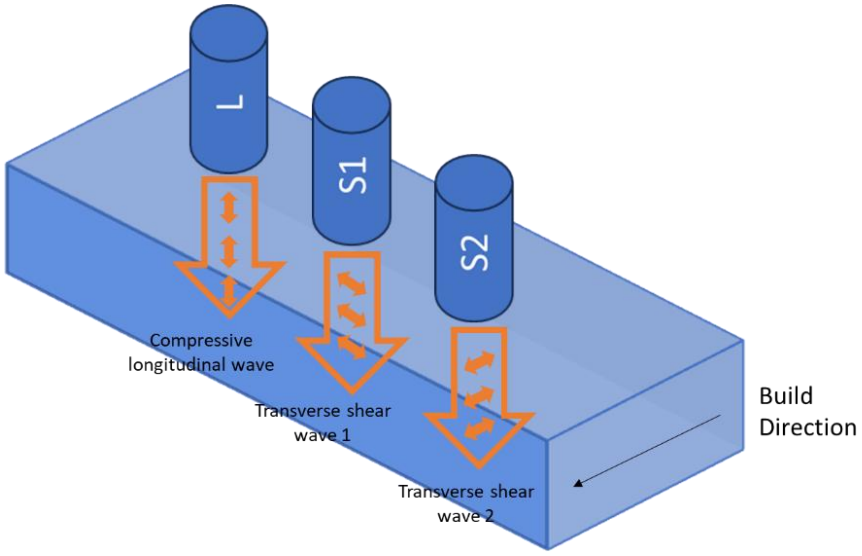

Figure 9. Schematic of longitudinal and shear time-of-flight and velocity measurement approach in relationship to the build direction for the coupons

Ultrasonic velocity measurements were obtained using a longitudinal (compression) wave probe and a normal incidence shear (transverse) wave probe that was used at 0 and 90-degree orientations. Pulse-echo mode was used to determine the time-of-flight, which was combined with the dimensional measurement of the sample thickness to calculate the longitudinal (V_l), and shear (V_{S1} and V_{S2}) velocities.

Once the ultrasonic velocities were obtained for the different material coupons or specimens, the elastic mechanical properties were computed using relationships for isotropic material behavior (Krautkrämer 1990). For an isotropic material, the Poisson's ratio (υ) can be estimated from the longitudinal (Vl) and shear velocities (VS) by:

$$\upsilon = \frac{1 - 2\left(\frac{V_s}{V_l}\right)^2}{2 - 2\left(\frac{V_s}{V_l}\right)^2} \quad (1)$$

The shear modulus (G) is calculated from the shear velocity (VS) and material density (ρ) using:

$$G = \rho V_s^2 \quad (2)$$

The elastic (Young's) modulus (E) is calculated using the longitudinal velocity (V_l), the material density (ρ) and Poisson's ratio (υ) using the following relationship:

$$E = \frac{V_l^2 \rho (1+\upsilon)(1-2\upsilon)}{(1-\upsilon)} \quad (3)$$

Ultimately, the bulk modulus is calculated using the longitudinal and shear velocities and the material density with the following relationship:

$$B = \rho\, V_l^2 - \frac{4}{3}(\rho V_s^2) \quad (4)$$

Acoustic velocity measurements were obtained on the 13 remaining. These remaining coupons were used to calculate the elastic mechanical properties for each of the blocks. The pulse echo technique was used to measure the velocities perpendicular to the build direction. Preliminary results are shown in (Table 5).

Table 5. Ultrasonic NDE elastic mechanical properties measurements

Sample No.	Density (g/cm3)	Young's Modulus (GPa)	Bulk Modulus (GPa)	Shear Modulus (GPa)	Poisson's Ratio	Acoustic Impedance (MRayls)	Laser Power (W)	Scan Speed (mm/min)
1	7.935	204.3	161.4	79.26	0.289	46.04	400	600
2	7.936	152.9	124.3	59.04	0.295	40.14	400	700
3	7.934	201.3	165.2	77.61	0.297	46.17	400	800
4	7.933	198.8	167.4	76.33	0.302	46.21	400	900
5	7.948	205.6	162.8	79.71	0.29	46.25	500	600
6	7.953	NA	NA	NA	NA	NA	500	700
7	7.945	200.3	171.8	76.69	0.306	46.66	500	800
8	7.949	201.5	169.3	77.43	0.302	46.54	500	900
9	7.961	201	162.5	79.01	0.291	46.18	600	600
10	7.962	207.5	162.1	80.63	0.287	46.34	600	700
11	7.959	202.1	164.8	77.99	0.296	46.25	600	800
12	7.958	201.6	166.3	77.64	0.298	46.34	600	900
13	7.961	199.3	167.1	76.6	0.301	46.29	700	600
14	7.956	NA	NA	NA	NA	NA	700	700
15	7.959	201.7	158.1	78.35	0.287	45.71	700	800
16	7.962	NA	NA	NA	NA	NA	700	900

The biggest outlier is Sample #2 which is reported to have the lowest density. Some variation is seen between the other samples, but the differences are small. Compared to a 316H wrought block that we have done the same measurements on previously, the Youngs' Modulus and Bulk Modulus are higher for the DED 316H cubes (excluding Sample #2).

As indicated in the literature, it is likely the porosity directly affects the modulus but not the hardness. The NDE density measurements correlated well with increasing laser power (Figure 10); porosity decreased with increasing laser power. Westphal and Seitz (2025) report on multiple 316L SS AM studies, highlighting each method and measured porosity range. Optical density on fused deposition printed 316L SS measured a 0.5-1.7% porosity, hence attaining nearly 99.5%-part density (Damon et al., 2023). Another fused deposition modeling based 316L SS study measured a 1.9–2.1% porosity using optical imaging (Caminero et al. 2022). However, optical density is investigated in a localized region, not the whole sample region. While it can provide a generalized value, XCT and Archimedes' method are more desirable for their ability to capture the bulk sample density. Like in Salmi's study, increasing laser power decreases porosity by 0.073% (Aversa et al. 2021). Porosity was measured using optical microscopy. Salmi et al. measured 316L SS DED printed parts with a porosity level <0.26% using XCT. The study found that laser power predominantly impacted part porosity. Laser power can be increased to decrease porosity towards a higher limit. Conversely, scan speed did not influence part porosity.

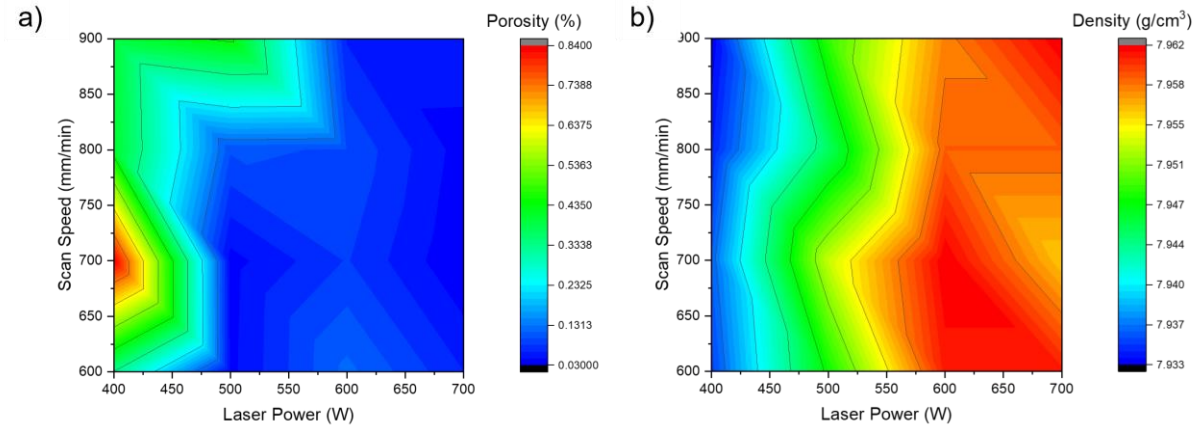

Figure 10. Two-dimensional (2D) gradient color maps comparing two input print parameters, laser power (W) and scan speed (mm/min), to an output print parameter, 316H SS density (g/cm^3)

As scan speed increases from 600 mm/min to 900 mm/min, the overall relative density decreases 0.1029%. As laser power increases from 400 W to 700 W, the overall relative density increases 0.4495%. Whereas increasing scan speed had little to minimal impact on 316H SS microstructure, suggesting scan speed is nearly independent of increasing or decreasing laser power. 316L SS studies on laser power nearly agree increasing laser power decreases porosity (Salmi et al. 2024). Aversa reported increasing laser power resulted in lower porosity and denser material (Aversa et al. 2021). Kumaran et. al., 2021 found by increasing laser power from 400 W to 600 W, resulting in less porous, finer grain structures and higher microhardness value. However, there are conflicting results regarding the effect of scan speed on 316L SS porosity. Majumdar et al., 2005 observed as scan speed increased, porosity decreased (Majumdar et al. 2005). Amar et. al., 2023 found scan speed did not affect porosity in comparison to laser power (Kartikeya Sarma et al. 2021; Amar et al. 2023). Despite SS316H

having higher carbon content, it did not greatly impact general trends in porosity, more so the microstructural phases because of DED.

However, there are further sub-porosity parameters that may prove critical, which could require a greater in-depth porosity study. E. Garlea et al. compared 316L SS LPBF printed sample elastic properties and formulated them to the microstructure, porosity, and other defects. As laser power decreased, porosity increased and density decreased (Garlea et al. 2019). Furthermore, the study defined the pores by their size, shape (spherical, elliptical), and orientation. In general, the elastic properties were affected by grain orientation, pore orientation relative to the build direction, and pore shape. This suggests that acquiring a bulk porosity value may not reveal the full characteristics of each sample.

2.1.2 Microstructural Analysis

A JOEL IT800 SEM (Peabody, MA) is used to examine the grain size and microstructure (Figure 11). Micrographs were taken at 20 kV operating voltage, 50× magnification, OA1 aperture with 3-µm step size. Images were analyzed using Aztec Crystal software. Grain size is measured using Max Feret Diameter, an area-weighted mean metric.

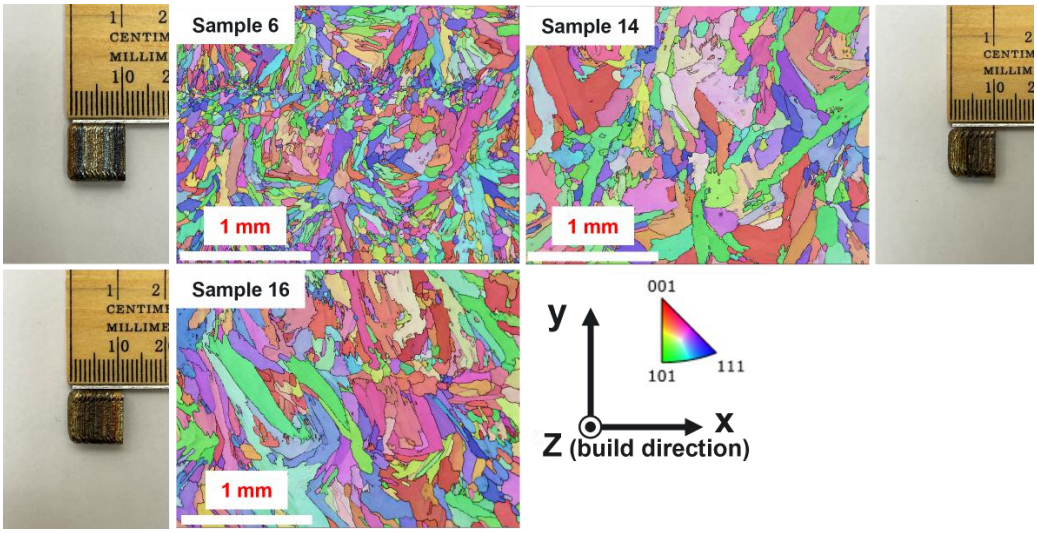

Figure 11. Cube sample, corresponding EBSD image, crystallographic orientation. Build direction is defined as the rolling direction (out of the page).

Quantitative microstructural analysis reveals significant variations in grain morphology and size across the processed samples. Sample 6 exhibits an average grain size of 208 µm, while samples 14 and 16 demonstrate substantially coarser microstructures with average grain sizes of 461 µm and 523 µm, respectively. This progression represents a 2.2-fold and 2.5-fold increase in grain size compared to sample 6, indicating a strong correlation between processing parameters and resulting microstructural characteristics.

The 316H SS cube sample microstructure was further evaluated and observed a distinct cellular structure Figure 12). ImageJ is used to approximately measure cell size. Sample 6 (Figure 12a) ~3.23 um, sample 14 (Figure 12b) ~6.01 um, and sample 16 (Figure 12c) ~6.17 um cell sizes.

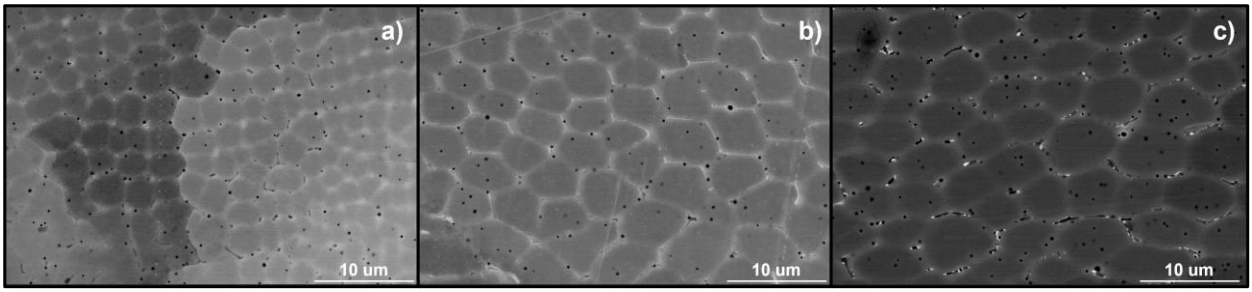

Figure 12. Cellular structure present in 316H SS samples. a) Sample six-cell structure at 500 W. b) Sample 14 cell structure at 700 W. c) Sample 16 cell structure at 700 W.

This phenomenon has been well documented and observed in AM printed parts. Cells tend to have a unique “honeycomb” structure and are oriented in the build direction or the <001> crystallographic direction due to the preferred FCC crystal direction. Generally, as laser power increases, cell size increases (Wang 2024). However, cell size also is greatly dependent on the heating/cooling rates. The study hypothesizes both the liquid-solid transformation and thermal strain contribute to the cellular morphology observed, creating a large dislocation network further induced by thermal strain. Liu et al. used scanning transmission electron microscopy and energy-dispersive spectroscopy maps to characterize highly dense dislocations along the walls with precipitation strung about the network (Liu et al. 2023). Additionally, transmission electron microscopy showed elemental segregation and depletion within and along the cellular regions (An et al. 2023). A distinction is these studies use 316L SS. Also, transmission electron microscopy is necessary to fully characterize cell morphology and understand the phenomena occurring within the cellular region, as they have on the 316H SS DED printed material and mechanical performance.

2.1.3 X-Ray Diffraction (XRD) Analysis of Cube Samples

Residual stresses originate in the melted powder or wire area known as the melt pool, which undergoes a rapid thermal heating/cooling process. After the current layer has been melted and cooled, the next layer is set up and powder is deposited onto the newly formed layer. The laser beam moves directly above the cooled layer along the scanning direction and moves with defined spot size and point distance. The melted powder layer expands across subjacent to the cooled layer below, creating a non-uniform temperature gradient. The cooled layer restricts the melting flow expansion by creating compressive forces, generating compressive stresses. The upper part of the cooled layer counteracts by applying opposing forces, creating tensile stresses, which results in tensile stress on the lower part of the cooled layer to counter act the compressive stresses. After expansion, the melted layer rapidly cools at a faster rate than the layer subjacent to it, generating tensile stresses. As shown in Figure 13, this results in permanent plastic deformation due to lattice strains and subsequently, residual stresses (Bartlett and Li 2019; Mercelis and Kruth 2006).

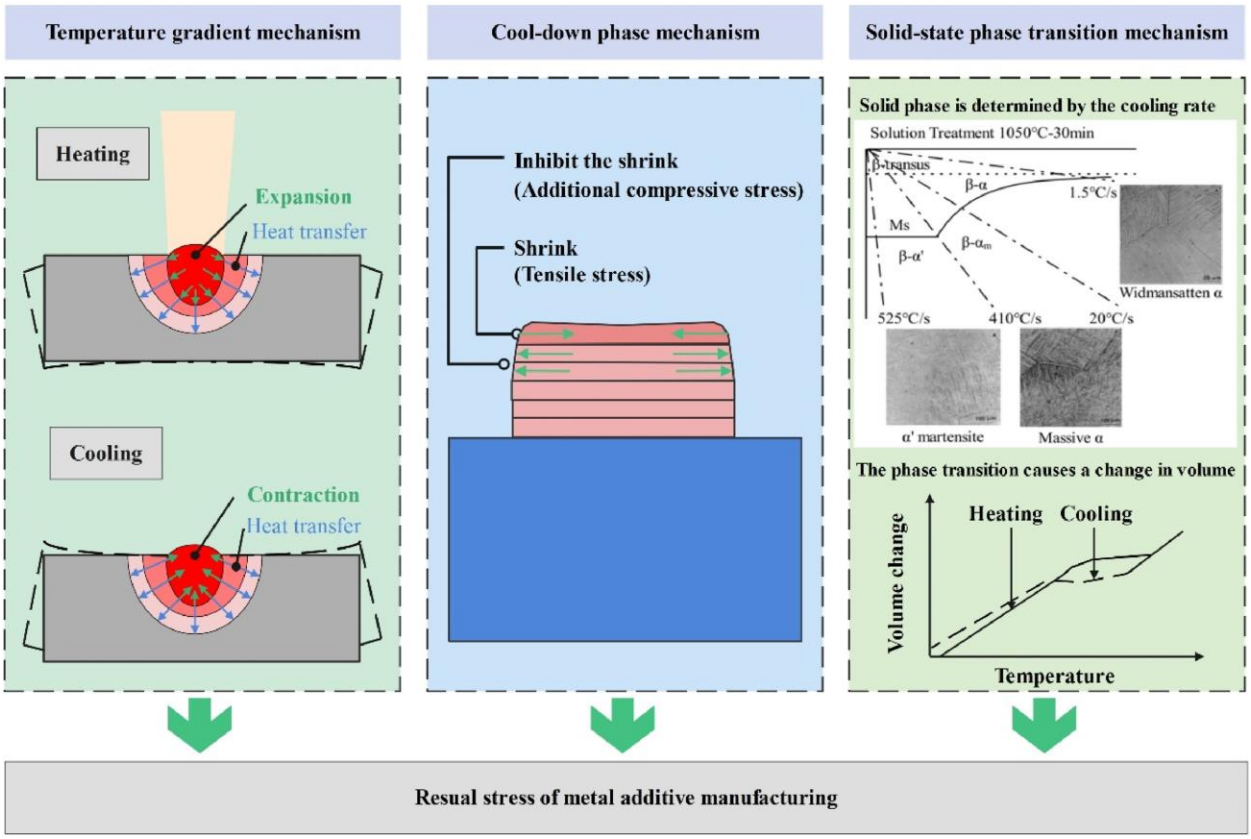

Figure 13. Mechanisms of residual stress formation in MAM. Note. From Chen, et. al., 2022. CC-BY

Residual stresses affect metal additive manufacturing (MAM) part fabrication and geometry such as cracking and warping. In addition, it has a significant impact on corrosion resistance, microstructure, and mechanical properties of the material (Romano et al. 2018; Chen et al. 2022). Zhang et al. 2020 discusses how residual stresses in DED affect tensile stresses as higher residual stresses causes higher compressive stresses to resist crack propagation (Huang et al. 2009; Moon et al. 2018; Zhang et al. 2020). Zhou et al., 2020 studied corrosion resistance in LPBF 316L SS samples and found residual stresses affect corrosion resistance due to the formation of melt-pool boundaries, creating additional inner compressive stresses (Zhou et al. 2020). Residual stresses are affected by MAM process parameters. MAM review studies find laser power, scanning speed, scan strategies, melt pool size, thermal gradient, and material type all impact residual stress (Chen et al. 2022).

Piscopo et. al., 2021 conducted a 316L SS LP-DED process parameter study by varying laser power and scan speed. Their results found that either increasing laser power decreased residual stresses due to a lower thermal gradient value or decreasing travel speed decreased residual stresses due to a smaller melt pool and greater interaction between the laser and material (Piscopo et al. 2021). Support structures are often used for LPBF whereas LP-DED techniques can directly print onto the substrate with no support structures. The high substrate rigidity increases residual stresses (Lu et al. 2021; Wei et al. 2021). Ding et al. (2023) conducted a DED scanning strategy study and their effects on residual stresses and deformations. X-ray diffraction measures the distance between lattice spacings within the sample's microstructure at surface-level diffractions (Schröder et. al. 2021), penetrating steels at several microns (Noyan et. al. 1995). Another study reported penetration to about 0.2 mm

(Rossini et. al. 2012). In NDE, a monochromatic neutron beam was focused on the sample, spreading the neutrons and projecting a diffraction pattern. The diffraction pattern determines the changes in lattice spacing. The elastic strains are derived from the changes in lattice spacings of the crystalline material using Bragg's law, generating a strain map. The stresses are calculated through the incorporation of the elastic properties of the material given by Hooke's law. (Lee et al. 2024). However, XRD can only find two stress components (Phan et al. 2019; Rossini et al. 2012).

Similarly, XRD detects and measures the distance between lattice spacings within the sample's microstructure. However, XRD is limited because its ability to penetrate beyond the surface is limited. A monochromatic X-ray beam is shot onto the sample, projecting a diffraction pattern. The diffraction pattern picks up diffraction peaks that correspond to lattice planes (Figure 14) (Huan et al. 2020). The stressed lattice spacings are measured using Bragg's law based on the X-ray beam wavelength, plane angle, and lattice spacing. Strains are calculated relative to stress-free lattice spacings. Hooke's law is used to calculate compressive and tensile stresses. (Zhang et al. 2023).

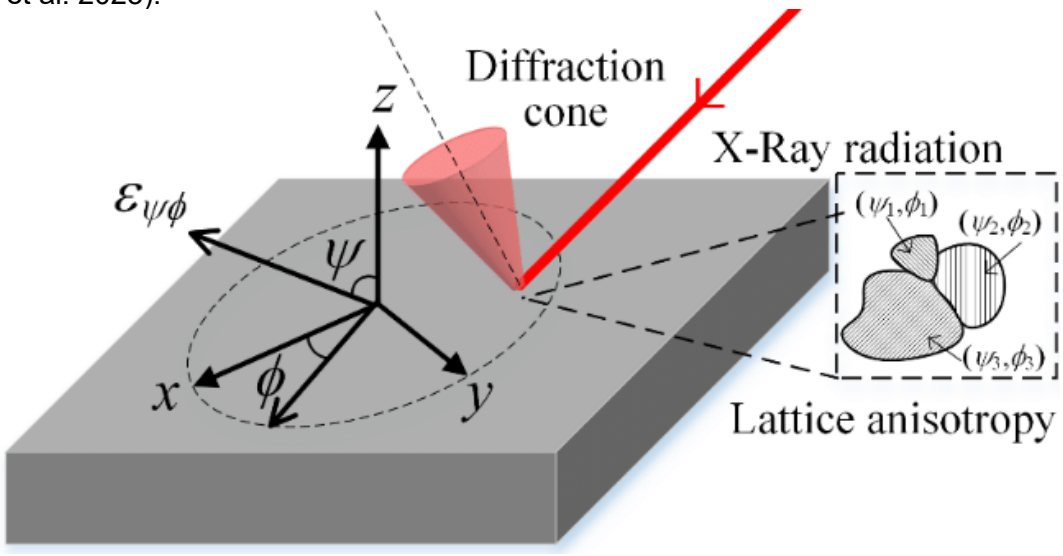

Figure 14. X-ray diffraction schematic to determine residual stresses. Note. From Huan et. al., 2020. CC-BY

A Bruker D6 Phaser (Bruker, Madison, WI) is used to measure the cubes' residual stresses as a one-dimensional stress analysis. X-rays are shot using a 1.54 Å X-ray Copper tube source at 40 kV high voltage and 30 mA current. The measurement method, omega mode, gave the ability to adjust the sample rotation (e.g. Azimuth angle). This would indicate if the sample were isotropic or anisotropic. Given 316H SS is an austenitic Fe-based material, Fe is selected from a metals material database, courtesy of Bruker's built-in software. The mentioned values are listed in Table 6.

Table 6. Residual stress XRD experimental parameters and estimated material properties.

Measuring method	Omega mode (iso inclination)
$\sin^2(\psi)$ angles (psi)	$12\ (-45°\ to\ 45°)$
2θ angles (±0.01°)	$132.761° - 142.721°$ (0.2 step size)
Azimuth (φ) angles (phi)	$(0°,\ -45°,\ -90°)$
Material element	Fe
Young's modulus (E)	220,264 (MPa)
Poisson's ratio (v)	0.28

The cube sample is mounted into a blue, malleable putty material to hold it in place (Figure 15C). The sample holder is mounted onto the sample stage (Figure 15B). Parameters are set in the Bruker software. Three measurements are taken at each Azimuth angle. The average and standard deviations are calculated and plotted (Table 7; Figure 16).

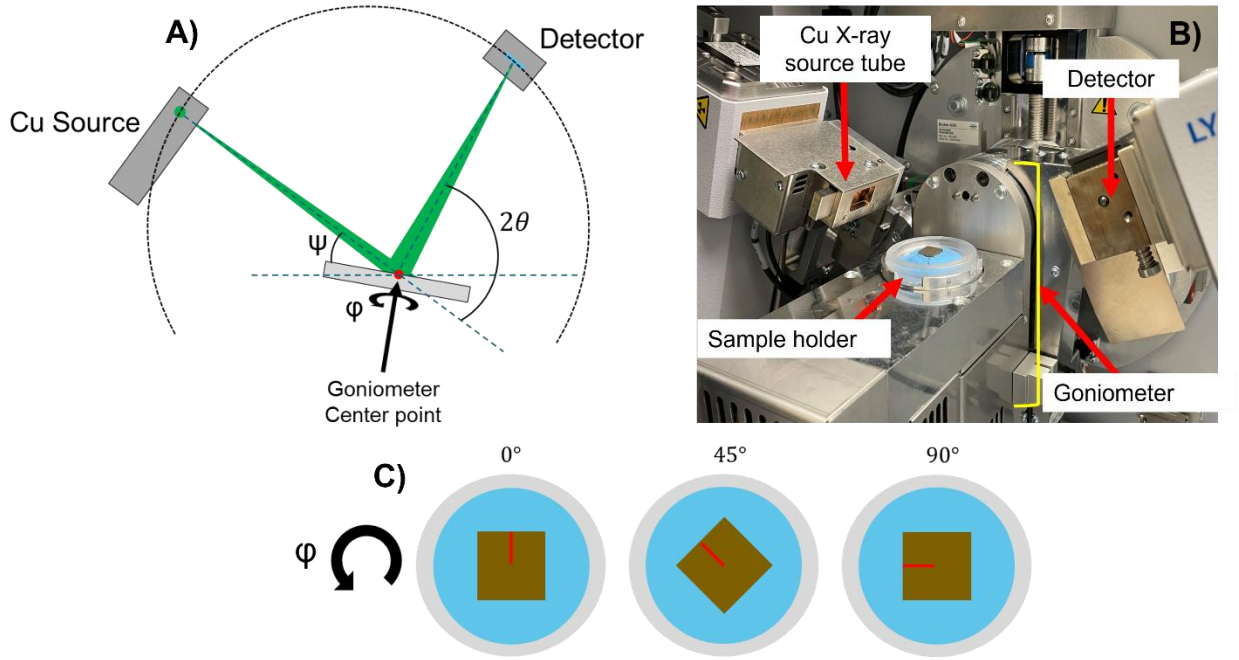

Figure 15. A) Iso-inclination mode diagram for residual stress measurements. B) Bruker D6 Phaser sample stage setup. A cut cube sample is placed in the sample holder. The Cu X-ray source tube shoots X-rays onto the sample and are captured using an LYNX-EYE detector to find changes in the d-spacing. C) Pictorial diagram of a mounted (blue putty) cube sample (brown) orientation (red line) in XRD scans. After the 0° initial scan, the sample is automatically rotated in the Bruker scanner, ensuring greater precision.

Table 7. Residual stress (normal stress) XRD values at the rotation angle (Phi)

	Phi (φ)	Normal stress (σ_{33}, MPa)	Average (MPa)
6	0°	-9.27	-7.08
	45°	-8.07	
	90°	-3.90	
14	0°	14.0	19.2
	45°	29.8	
	90°	13.7	
16	0°	-31.2	-47.6
	45°	-64.9	
	90°	-46.8	

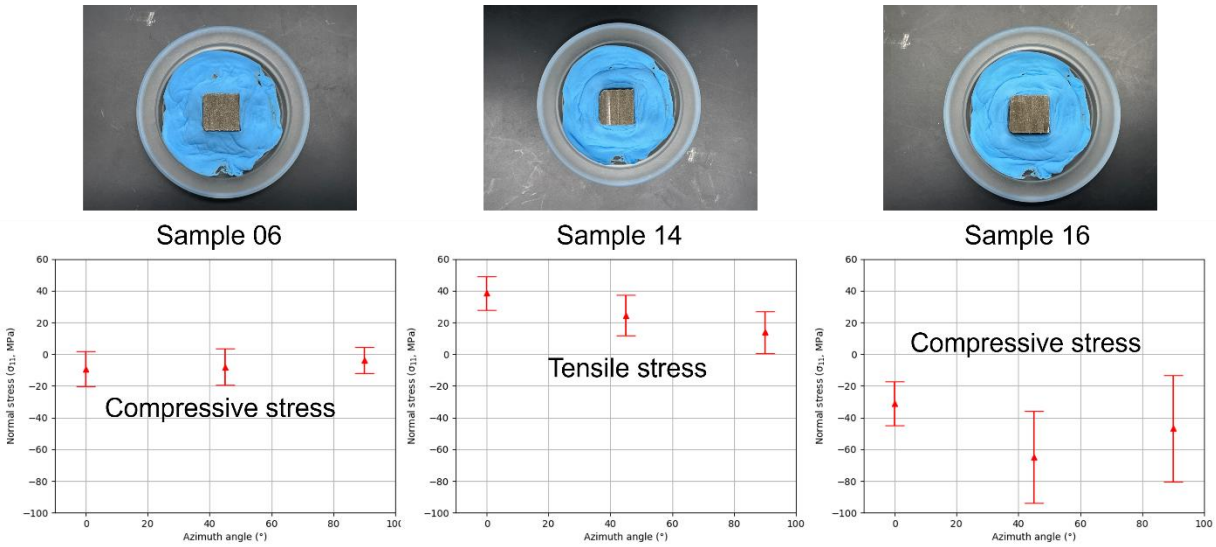

Figure 16. Residual stress XRD results. Negative stresses are compressive and positive stresses are tensile.

Samples 6 and 14 do not exhibit high variance between angles (Table 7; Figure 16). Conversely, sample 16 has the greatest variance. The EDM cutting process resulted in an uneven cut surface, which may interfere with the measured d-spacing and consequently, the calculated stresses. Samples 6 and 16 are under a compressive stress state, while sample 14 is under a tensile stress state. For further data analysis, the ASTM E2860-20, “Standard Test Method for Residual Stress Measurement by X-Ray Diffraction,” is consulted (International 2021). Based on the DED manufacturing and imaging data, three possible reasons for stress deviation could be given:

- The presence of stress relaxation due to EDM sample sectioning, thereby altering stress and strain states (Ablyaz et al. 2022).
- The sample microstructure has a large grain size presence that can reduce the number of grains available for diffraction at a given orientation.
- DED printing’s creates repeated heating/cooling cycles, which leads to a high possibility of creating an internal temperature gradient that can significantly change the strain state.

Further research was conducted to determine if residual stresses were connected to mechanical properties like Vicker hardness. A model to understand the relationship between residual stress and hardness based on plastic deformation found compressive stress results in higher hardness than tensile stress due to yielding or plastic deformation (Schroeder et al. 1995). However, it is challenging to make a definitive statement due to the lack of data. Had the samples not been cut, the stress magnitude may have been potentially greater. Another note to make is currently there is no ASTM procedure with a standard test method for residual stress measurements on AM material.

2.1.4 Vicker Hardness

Vickers microhardness is measured on all 16 316H SS cube samples. A Clark CM-402AT microhardness tester is used: 300 lbf indentation force, a 10 second dwell time, and a 5 × 5 indent matrix with a 5-mm indent gap to avoid interference from surrounding existing indents. Hardness values are measured and averaged. Figure 17 is a colored 2D contour plot used to find the optimal laser power and scan speed to Vickers hardness.

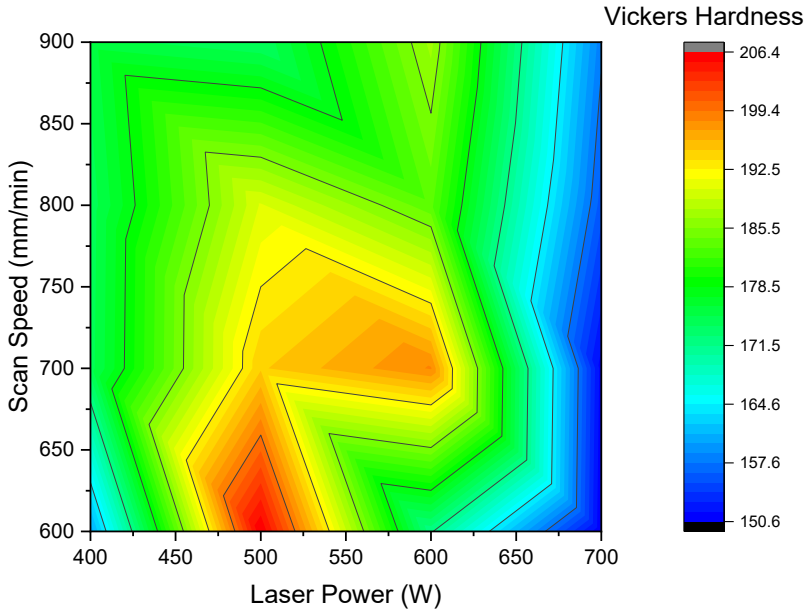

Figure 17. Relative density vs. Vickers microhardness plot relative to laser power at 400 W (dark/navy blue), 500 W (orange), 600 W (green), and 700 W (light blue)

The hardness evolution across different laser power settings demonstrates the complex interplay between microstructural features and mechanical properties. Between 400 W and 500 W, a notable hardness improvement is observed, stemming primarily from enhanced densification and porosity reduction. However, further increases in laser power beyond the 500-W threshold result in a progressive decline in hardness values. This deterioration can be directly attributed to the formation of increasingly coarser grain structures at higher power levels.

2.1.5 Relationship between Elastic modulus, hardness, laser power, and scan speed

Figure 18 shows Vickers hardness does not directly correlate to Young's modulus measurements. The hardness measurement for Sample 2 is an outlier.

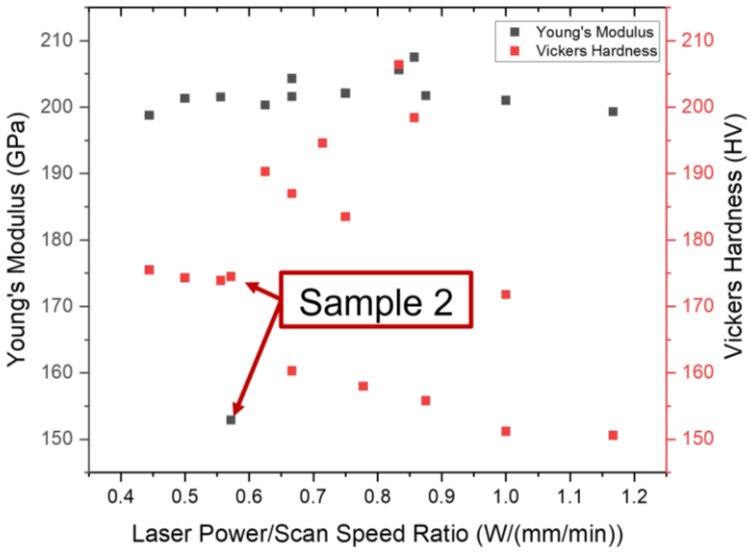

Figure 18. Scatterplot comparing NDE elastic properties of Young's modulus, direct measurement of Vickers Hardness, and 316H DED laser power and scan speed parameters

Kan et al. conducted a literature review on the impact of porosity on mechanical properties. The study found decreasing porosity improves elastic modulus, tensile strength, and elongation at fracture (Kan et al. 2022; Zhang et al. 2017; Leicht et al. 2020). However, at lower porosity levels, the relationship is not as apparent (Kan et al. 2022). Additionally, a lack of fusion pores greatly impact the elastic modulus and strength of vertically built samples oriented in the print direction (Suryawanshi et al. 2017; Alsalla et al. 2018; Röttger et al. 2016; Ronneberg et al. 2020; Choo et al. 2021; Wood et al. 2019; Carlton et al. 2016). The study concludes that the tensile properties, elastic modulus, and strength are predominantly affected by pore morphology and the number of pores. Therefore, it is important to conduct mechanical property tests to verify if these claims hold and apply to all SS types, such as 316H SS, not just 316L SS.

2.2 SS316H DED Small Cylinder Characterization

XCT analyses were done on a Zeiss Xradia Versa 610 with a 9.5 um voxel resolution, 160 kV tube voltage with 2 seconds/projection scanning time. A total of 1,600 projections were taken.

In Figure 19, two slices were selected to examine and measure the internal pore present in the tube. However, it does not give a full analysis of the actual pore size, pore morphology, and estimated porosity. These parameters must be calculated to determine the full tube density and porosity profile. Volumetric energy density is defined as $E_V = P/(v\sigma t)$; P is laser power; v is scan speed; sigma is laser diameter; and t is layer thickness. As E_V increased, porosity decreased (Sun et al. 2024). Even with five different process parameter sets, density remained >99% (DelRio et al. 2023). Additionally, higher layer thickness results in lack of fusion and poor layer bonding, resulting in irregularly large pores (AlFaify et al. 2018).

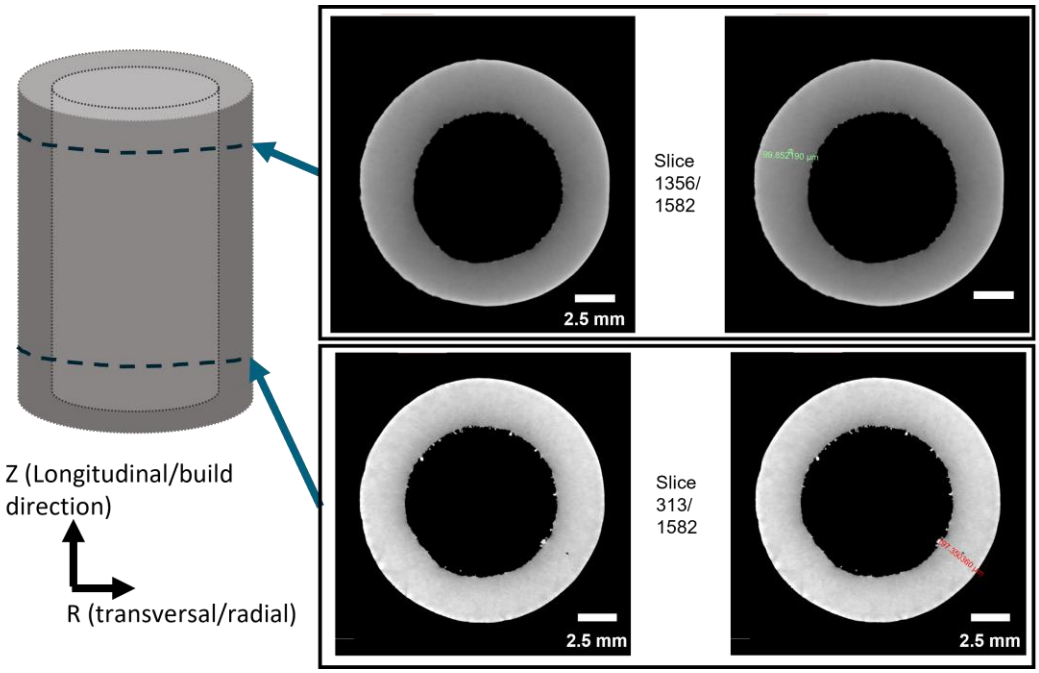

Figure 19. Small tube (T3) XCT at the top and bottom portions of the part

Tan et al., 2019 used XCT to detect pore diameter in 316L SS DED printed samples to find >99.8% density; a higher density was observed in the top zone than the bottom zone, which could be improved by dynamic control of laser power input and pre-heating the build plate (al. 2019).

2.3 SS316H DED Large Cylinder Residual Stress Measurement

Tests to determine the residual stress distribution in a DED 316H SS pipe component were performed. Stress components (both axial direction [build direction] and hoop direction) were measured by XRD based on ASTM E2820. Through-thickness profiles of residual stresses on the pipe wall also were evaluated by electro-etching from pipe surface up to ~600 µm depth.

Residual stress was measured by using PROTO iXRD residual stress measurement system. The project assesses residual stress distribution in a 316H SS pipe component printed by LP-DED AM. Figure 20 shows the measured locations around the pipe. Stress components, along both axial direction (build direction) and hoop direction at each location, were measured by XRD based on ASTM E2820. Four sides around the pipe were examined. At each side, the examination was performed at four equally spaced locations from the bottom to the top. Circumstantial stress distribution was reported, Through-thickness profiles of residual stresses on the pipe wall also were evaluated by electro-etching from pipe surface up to ~600 um depth.

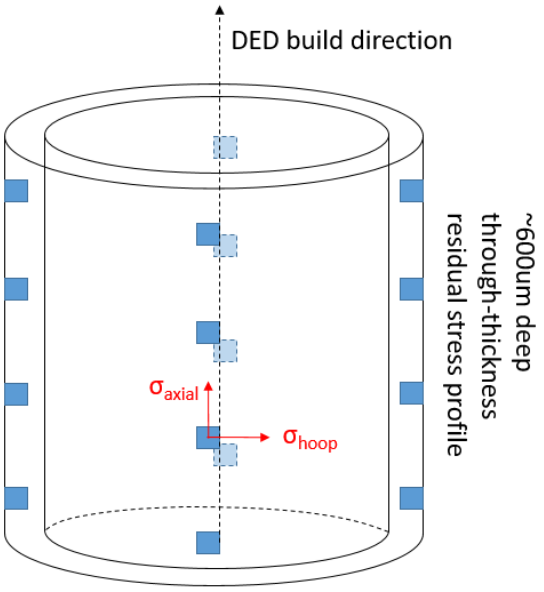

Figure 20. Locations of XRD measurement for the large 316H cylinder

Electro-etching was used to remove material from different locations across the pipe with a known material removal rate. Figure 21 shows the etching set-up. An etching cell apparatus was Three-dimensionally (3D) printed to fit the pipe curvature with an O-ring seal at the bottom. The contact diameter of the etching cell on the pipe is ~8.5mm. The electrolyte was 10 vol% HCl with the pipe serving as the anode and a 316 SS plate serving as a cathodic counter electrode. Electro-etching was conducted at 20 V DC for 1 minute to achieve approximately 100 μm material removal. After etching, the surface of work piece was thoroughly cleaned with acetone and dried. The removal depth at each pit was measured by caliper. The etching process may be repeated if needed to achieve the targeted depth.

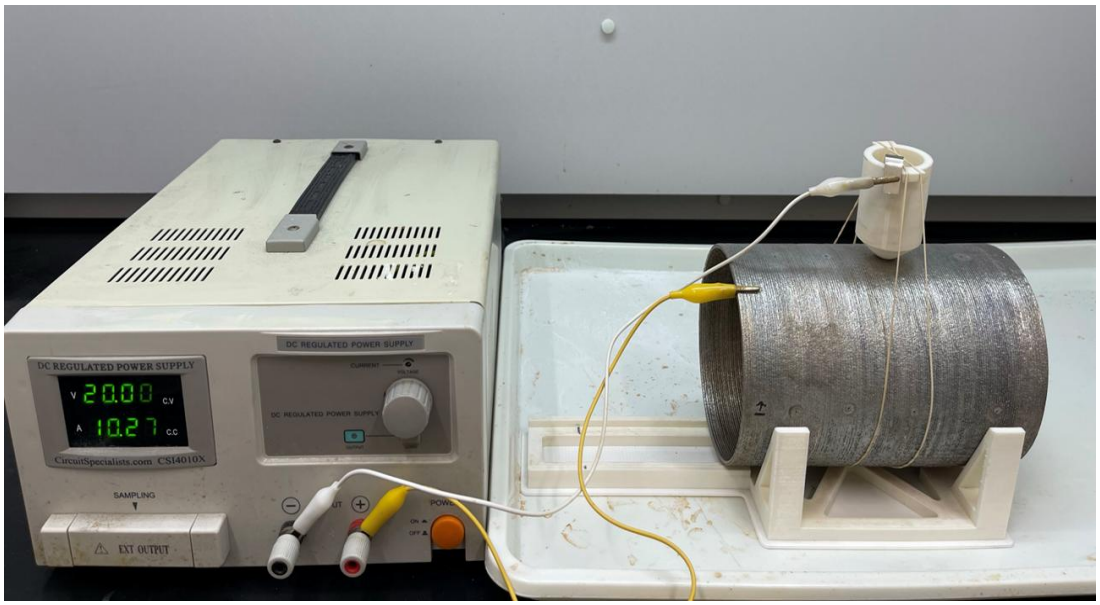

Figure 21. Electro-etching set-up

The XRD residual stress measurement was performed based on ASTM E2820. Mn_K-Alpha X-ray tube (wavelength 2.103 Å) was used with the peak analysis targeting FCC {Amar, #12}. Figure 22 shows the experimental set-up. Stress along hoop direction and axial direction were evaluated.

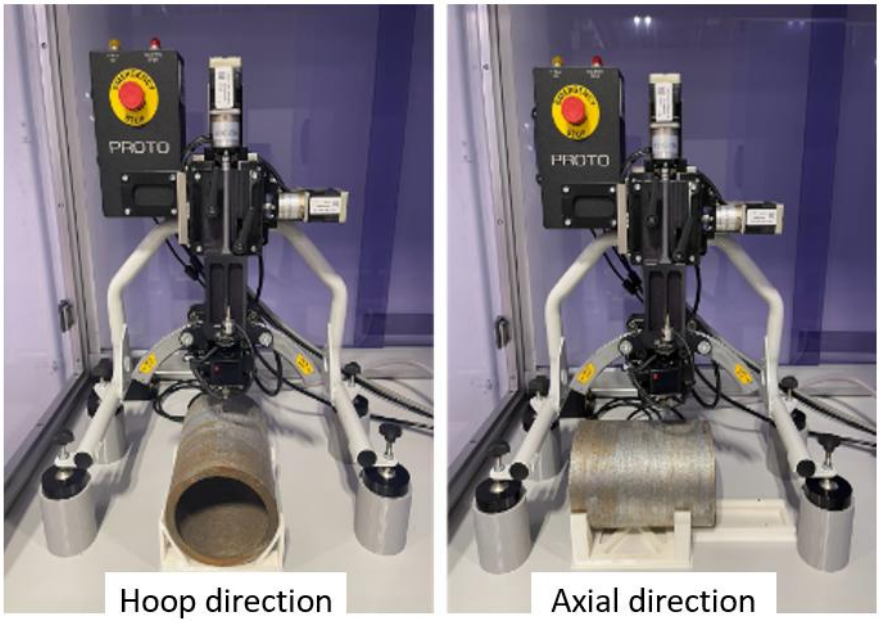

Figure 22. XRD residual stress measurement set-up

Figure 23 shows the detection method of omega mode diagram for measurement in σ_{11} direction based on ASTM E2820.

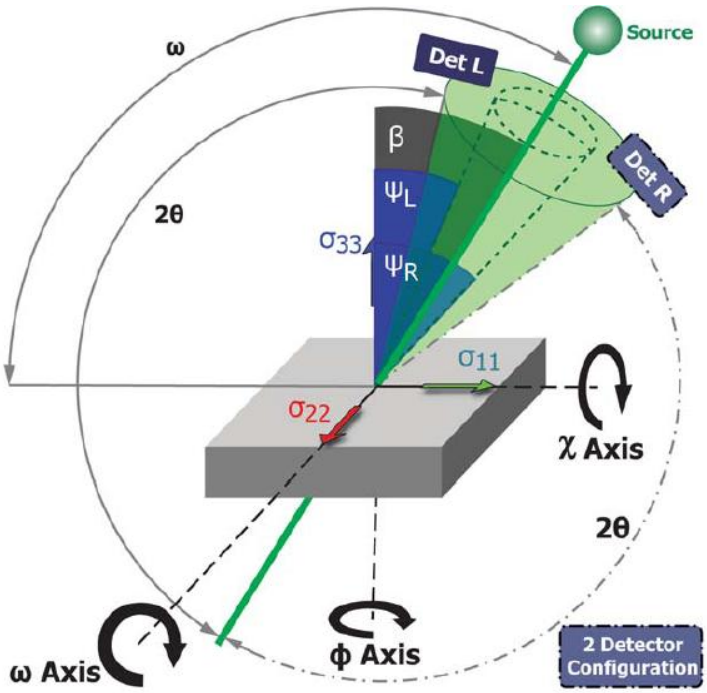

Figure 23. Omega Mode Diagram for Measurement in σ11 Direction (from ASTM E2820)

Stress normal to the surface (σ_{33}) is assumed to be insignificant because of the shallow depth of penetration of X-rays at the free surface. This assumption is applied to reduce the stress-strain relationship to the following formula.

$$\varepsilon_{\varphi\psi}^{\{hkl\}} = \frac{1}{2} s_2^{\{hkl\}} \left[\sigma_{11} \sin^2\psi + \tau_{13} \sin(2\psi)\right] + C$$

Figure 25 shows an example dataset of d (2θ) vs. $Sin^2\psi$ relationship. The value, the normal stress σ_{11} usually influence the overall slope of the data, while the shear stress τ_{13} is related to the direction and degree of elliptical opening. By fitting the measured curve, both σ_{11} and τ_{13} can be obtained.

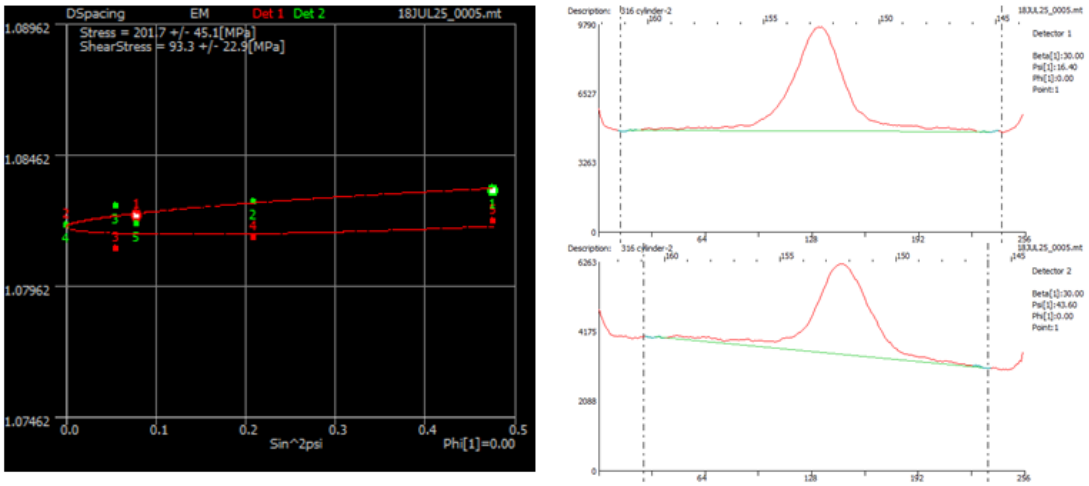

Figure 24. Example dataset of d (2θ) vs. Sin2ψ relationship

The measurement errors from the XRD system and from the operator were evaluated. Table 8 shows the system error by measuring the same spot without relocating work piece three times. Table 9 shows the operator error by relocating the work piece three times to measure the same spot.

Table 8. System measurement error on the etched surface

Measurement	Stress (MPa)	Deviation (MPa)
First	248.89	97.6
Second	247.43	96.01
Third	247.3	95.27

Table 9. Operator measurement error on the etched surface

Measurement	Stress (MPa)	Deviation (MPa)
First	248.89	97.6
Second	257.96	74.95
Third	275.38	79.81

Surface roughness has significant influence on residual stress measurement. Table 10 shows the validation of operator error on an unetched surface. Significant change was observed as compared to Table 9.

Table 10. Operator measurement error on the unetched surface

Measurement	Stress (MPa)	Deviation (MPa)
First	35.62	15.03
Second	28.06	18.64
Third	28.26	18.43

Figure 25 shows the morphology of pits on the pipe at different etching times. The etching depths of each pit are reported in Table 11. After the first etching, deeper pits were reported due to the large surface roughness. Based on etch 2 and etch 3, each etching step removed roughly 100–200 um materials from the pits.

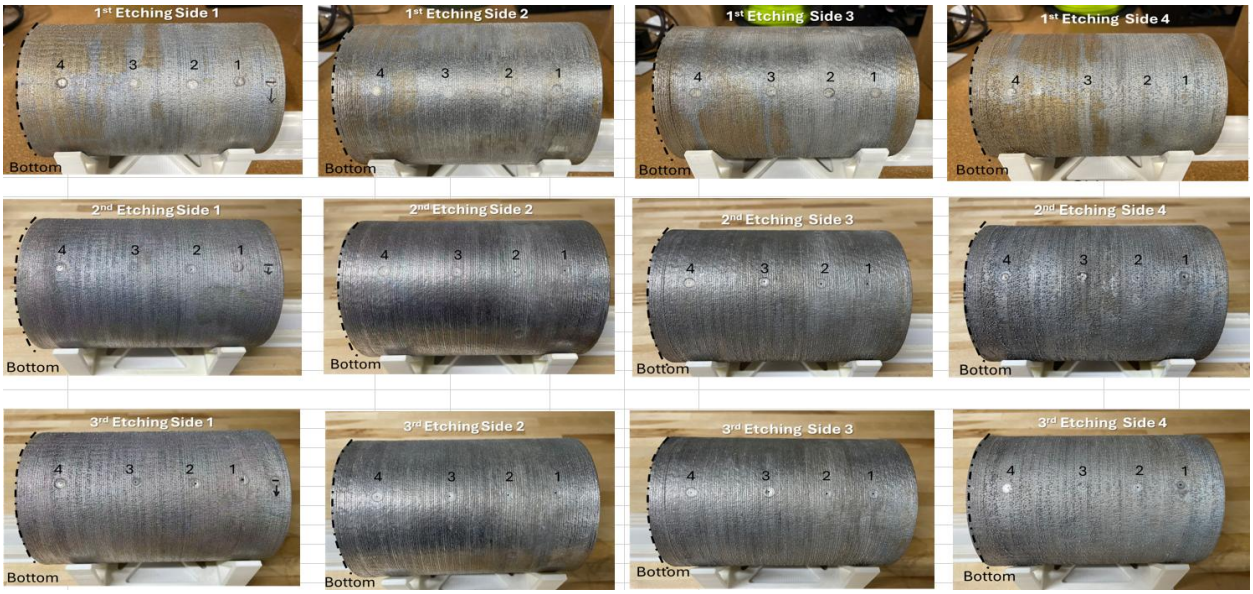

Figure 25. Morphology of pits on the pipe

Table 11. Summary of pit etching depth after the etching process

Etch 1	**Distance from bottom (mm)**	**Point #**	**Side 1**	**Side 2**	**Side 3**	**Side 4**
	150	1	0.5	0.29	0.3	0.69
	120	2	0.56	0.2	0.33	0.23
	80	3	0.22	0.26	0.32	0.71
	30	4	0.35	0.24	0.23	0.45
Etch 2	**Distance from bottom (mm)**	**Point #**	**Side 1**	**Side 2**	**Side 3**	**Side 4**
	150	1	0.58	0.38	0.38	0.72
	120	2	0.63	0.28	0.44	0.54
	80	3	0.37	0.33	0.44	0.66
	30	4	0.55	0.34	0.31	0.59
Etch 3	**Distance from bottom (mm)**	**Point #**	**Side 1**	**Side 2**	**Side 3**	**Side 4**
	150	1	0.71	0.52	0.52	0.81
	120	2	0.75	0.44	0.58	0.62
	80	3	0.48	0.44	0.56	0.74
	30	4	0.63	0.5	0.44	0.61
Etch 4	**Distance from bottom (mm)**	**Point #**	**Side 1**	**Side 2**	**Side 3**	**Side 4**
	150	1	0.8	0.61	0.57	0.87
	120	2	0.85	0.53	0.63	0.72
	80	3	0.6	0.55	0.6	0.8
	30	4	0.8	0.63	0.48	0.75

Figure 26 through Figure 29 summarize the residual stress σ_{axial} and σ_{hoop} after the first, second, third, and fourth etchings.

Y-axis shows the stress in MPa and X-axis shows the location of the pit from the bottom of the pipe. Four sides were compared in the same plot. Most stress measured were tensile stress. However, the four sides showed different trends in stress profile along both build direction and wall thickness. As expected, the hoop stress showed lower stress than the axial stress at the same location, with the stress magnitude of hoop stress is mostly within 200 MPa. With the increase of etching time, σ_{hoop} switched from tensile to compressive stress while σ_{axial} did not show clear trend.

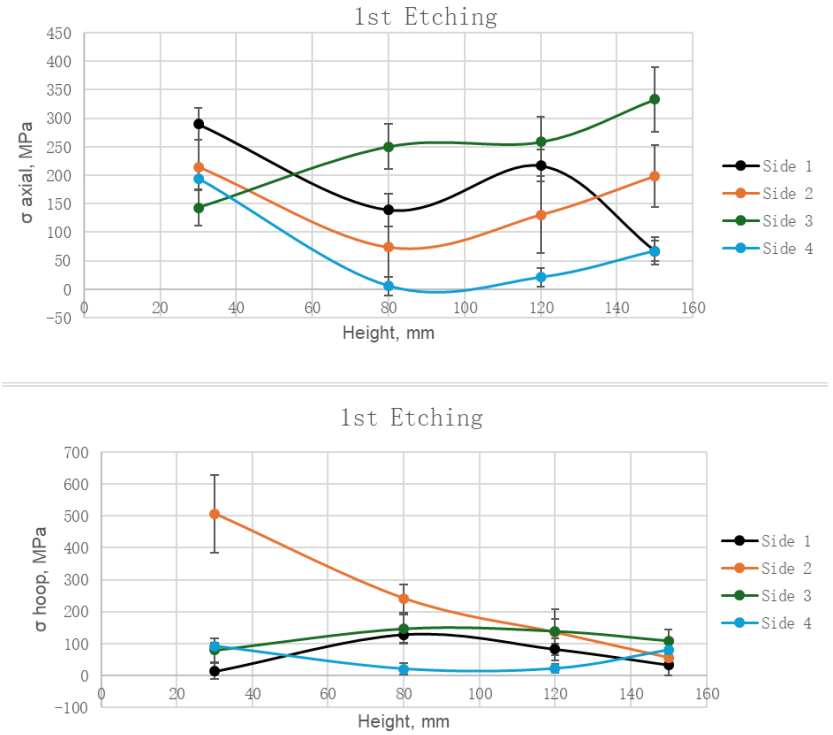

Figure 26. σ_{axial} and σ_{hoop} after the first etching

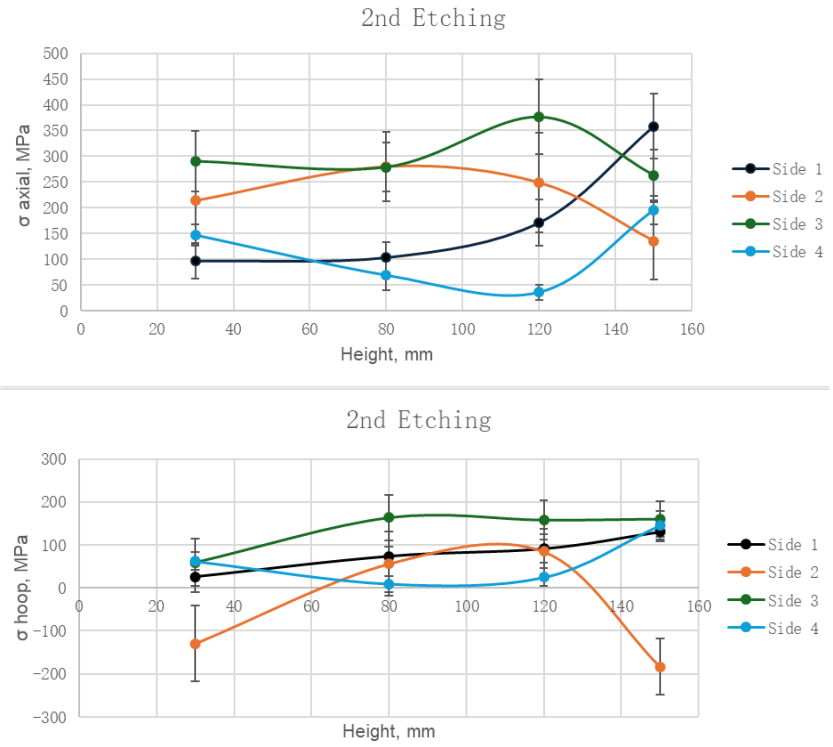

Figure 27. σ_{axial} and σ_{hoop} after the second etching

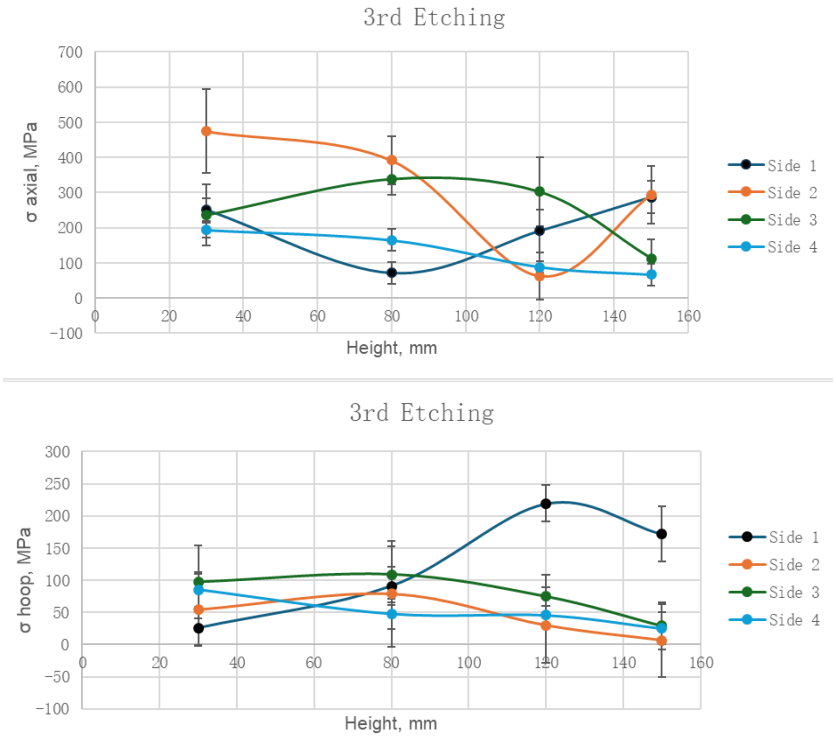

Figure 28. σ_{axial} and σ_{hoop} after the third etching

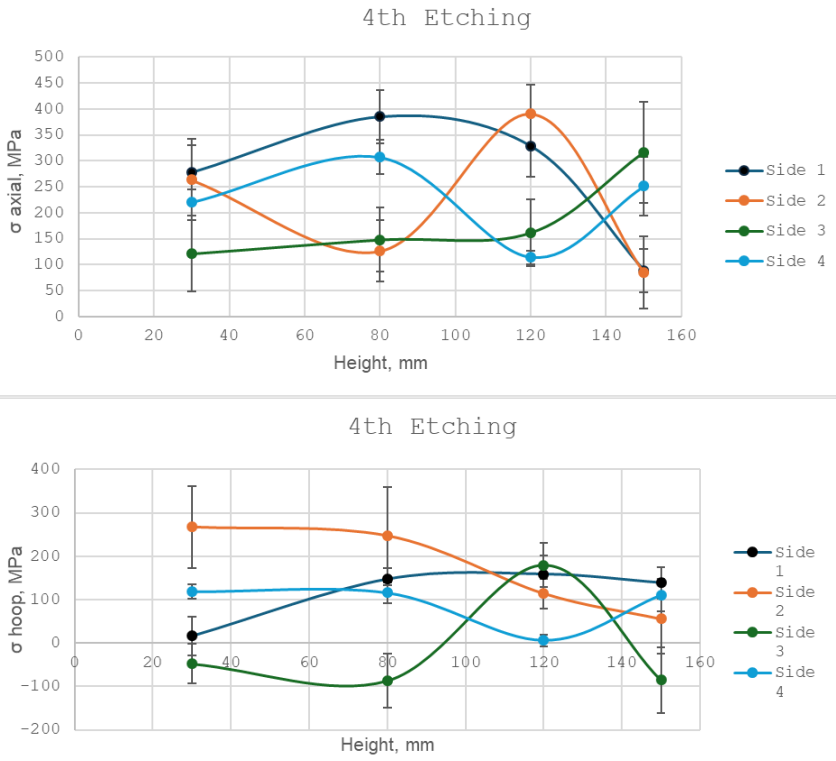

Figure 29. σ_{axial} and σ_{hoop} after the fourth etching

2.4 Flow 3D Simulation

Another methodology is to predict porosity in additively manufactured samples before even printing out samples and experimentally characterizing them. Porosity prediction can be done using finite element methods, analytical models, and numerical models. However, depending on the process parameter of interest, care must be taken to determine the best method. Mahmood et al. (2025) used a volumetric energy density model to do a process parametric study and a finite element model to predict thermal conditions, melt pool, and resulting porosity. Recently, ML and neural networks are newer, novel approaches to process parameter optimization of porosity and mechanical property predictions (Era et al. 2022; Zhang et al. 2024b; Alamri et al. 2025). Alamri et al. (2025) compared five different ML studies and determined AlSi10Mg AM samples were most favorable with a laser power and scan speed combination that achieved >99% relative density and >120 HV hardness. The studies are evident that the ML methods are just as valuable, if not more valuable than the multitude of experimental process parameter studies existing in literature. From them, experimental data is ML input data to further optimize and improve the models. In this case, The Purdue experimental process parameters (i.e., laser power, scan speed, and experimental porosity) of the 316H SS cubes to the Flow 3D simulations. Table 12 compares experimental and simulated porosities.

Table 12. Porosity results from simulation and experiment

Laser Power (W)	Scan Speed (mm/min)	Simulated Porosity (%)	Experimental Porosity (%)
400	600	0.039	0.332
400	700	0.040	0.840
400	800	0.042	0.409
400	900	0.048	0.401
500	600	0.037	0.042
500	700	0.038	0.040
500	800	0.03979	0.100
500	900	0.04190	0.445
600	600	0.03468	0.120
600	700	0.03916	0.082
600	800	0.03655	0.096
600	900	0.03760	0.062
700	600	0.03500	0.064
700	700	0.03690	0.030
700	800	0.04260	0.038
700	900	0.04813	0.061

Flow-3D simulations of the LP-DED process were conducted for 316H SS to assess the printability and to investigate whether computationally predicted porosity can be quantitatively correlated with experimentally observed defects. The primary objective to capture the melt pool dynamics, solidification behavior, and defect formation mechanisms and enable a predictive understanding of process–structure relationships. The simulation outputs are used for developing a corrector model, which aims to bridge the gap between physics-based simulations of Flow-3D and experiments by accounting for discrepancies arising from unmodeled physical effects. By using these corrections, the predictive accuracy of porosity distribution and magnitude can be significantly improved. The corrected outputs can then be used to optimize process parameters to minimize defects and improve mechanical performance of DED-manufactured 316H SS components.

Sixteen cubic specimens (1 cm³ each) of 316H SS were fabricated using a powder-fed laser DED process. The process variables consisted of four laser powers (400 W, 500 W, 600 W, 700 W) and four scan speeds (600, 700, 800, and 900 mm/min). The Flow-3D software was used to replicate the 16 parameter combinations. The DED process was modeled as a sequence of 10 layers deposited by scanning the laser over the substrate.

$$\text{Simulated porosity} = \frac{V_{void}}{V_{total}}$$

where V_{void} is the total pore volume and V_{total} is the total track volume. Following experimental data (Table 13) were captured in Flow 3D to replicate the simulations in addition to laser power and scan speed.

Table 13. Experimental input for Flow-3D simulations

Experimental Parameters	Values
Powder feed rate	5 g/min
Carrier gas flow rate	7 L/min
Powder capture efficiency	30–35%
Laser spot diameter	1.2 mm
Particle Size Distribution	53–150 micrometers

Thermo-calc was used to compute distribution of physical variables—viscosity, thermal conductivity, density, specific heat, surface tension as well as solidus and liquidus temperature for SS 316 H. Due to non-availability of some experimental data, few assumptions were made for the simulation (e.g. exact particle distribution, working distance, diameter of powder stream, etc.). The simulated porosity and experimental porosity are tabulated in Table 14.

Table 14. Comparison of simulated and experimental porosity values for two processing conditions

P (W)	S (mm/min)	SimP (%)	Experimental (%)	Predicted (%)	Error (%)
400	700	0.040	0.840	0.846	+0.006
500	900	0.04190	0.445	0.454	+0.009

LP-DED was simulated by melting 316H SS powder from a nozzle using a laser power source to form a melt pool on the substrate. For each simulation, the laser was scanned 10 times over the substrate to print 10 layers. Because of incomplete experimental information, several assumptions were made. For example, the exact particle size distribution was kept within the 53–150 µm range.

Figure 30 illustrates the simulated temperature field distribution during a single-track deposition event. The melt pool boundary is sharply delineated, with peak temperatures exceeding the liquidus by ~400–600°C to ensure complete melting in the central bead region.

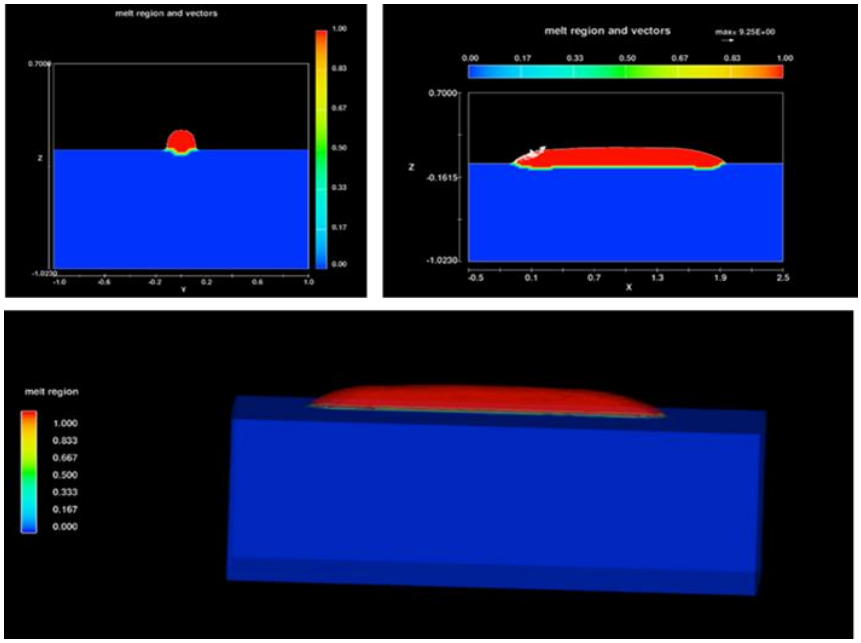

Figure 30. Simulated results of melt pool for 316 H SS using (a) laser power 500 W and scan speed 700 mm/min, (b) laser power 700 W and scan speed 700 mm/min, and (c) laser power 700 W and scan speed 900 mm/min

Table 14 presents the key process parameters used in the simulation alongside predicted porosity metrics. Process parameters include laser power (P) and scan speed (V). From the simulation outputs, pore size distribution, average porosity volume fraction, and melt pool dimensions (i.e., width, depth, and length) were extracted. The table compares predicted porosity fractions with experimental values from metallographic cross sections.

From the simulations, for constant power and other parameters, the height and length of tracks printed is dependent on scan speed. Lower scan speed produced shorter and higher tracks, while higher scan speed produced longer and flatter track prints. We observed a similar trend with simulated porosity too, because a constant power scan speed seemed to influence the simulated porosity. Further optimized simulations are required to solidify these observations.

While Flow-3D provides a physical representation of melt pool dynamics, discrepancies arise between computational predictions and experimental results due to uncertainties in input parameters, powder size distribution, and process variability. These discrepancies show in predicted porosity volume fraction, pore morphology, and spatial distribution. For this reason, we are developing a corrector model that is a post-processing ML adjustment layer that leverages experimental data to refine Flow-3D predictions. This approach will add fidelity to the computational outputs to quantitatively match experimental observations. The corrector model thus bridges the gap between high-fidelity physics simulations and real-world manufacturing conditions.

A multivariate polynomial regression model was developed using 14 of the 16 datapoints in Table 3 to quantify the influence of the parameters power P, scan speed S, and simulated porosity SimP—along with their higher-order and interaction terms on the dependent variable of interest. The general form of the fitted model is:

$$Porosity_{exp} = 4.58 - 8.54 \times 10^{-3}P + 1.71 \times 10^{-2}S - 4.08 \times 10^{2}SimP + 7.06 \times 10^{-6}P^{2} - 7.21 \times 10^{-6}P.S + 1.26 \times 10^{-1}(P.SimP) + 2.23 \times 10^{-6}S^{2} - 4.27 \times 10^{-1}(S.SimP) + 8.33 \times 10^{3}SimP^{2}$$

The very large positive coefficient (8.33×10^{3}) indicates that small deviations in simulated porosity are magnified in their contribution to experimental porosity which is not surprising as the SimP is the calculated quantity. Interaction effects from negative coefficient for S·SimP implies that higher scan speed in combination with higher simulated porosity tends to reduce experimental porosity. Model validation was performed on two randomly selected data points that were excluded from training:

The prediction error in both validation cases is below 1% absolute, demonstrating the model's preliminary ability to map simulation outputs to experimental values. Caution must be exercised in interpreting the model's generality. The dataset comprises only 16 data points, all from a single material (316H SS) and a narrow range of process parameters. A second-order polynomial model with multiple interaction terms can potentially overfit such a small dataset, capturing noise or experimental variability as though it were a true underlying trend. This risk is amplified by the large coefficient magnitudes for certain terms, such as $SimP^{2}$, which may cause the model to extrapolate poorly outside the training range.

To improve robustness and applicability across a broader range of AM scenarios, future work should incorporate more experimental cases spanning wider laser powers, scan speeds and powder feed rates and extend the training set to include alloys such as 316L SS, which would allow the model to capture material-specific porosity mechanisms.

3 Manufacturing Laser Powder Bed Fusion Components

Because of increased interest from industry partners and the AMMT program, LPBF has been identified as the next manufacturing process to undergo the benchmarking study of the five 316H SS components identified in FY24. Specifically, in FY25 the AMMT program's contribution to the international Generation IV Advanced manufacturing and materials engineering working group benchmark study will focus on a second manufacturing-material combination—namely LPBF-316H—that is relevant to the industry and aligned with the AMMT program's qualification effort. As this material-manufacturing combination has been studied in prior years in the AMMT program, more focus will be given to the geometrical and its dimensional consistency in this task. The results of this benchmark study will facilitate the understanding of manufacturing options and knowledge to enable accelerated readiness for new or replacement designs. This effort also will provide a direct comparison of key differences between components manufactured through powder DED and LPBF.

3.1 Support structure design

A significant portion of the build time is attributed to generating support structures. For example, the total part volume of the elbow is 547,790 mm³, while the total support volume for Support #1 is 569,592 mm³.To reduce build time while still maintaining sufficient supports for the elbow overhang, we designed several support structures, as shown in Table 15 and Figure 31. Designs for these were generated using the QuantAM build preparation software. QuantAM can place grits on curved surfaces to enable support generation. Although manual grid selection could further reduce build time, we used the "Auto Generate" function to ensure reliable support placement and a successful build.

Table 15. Support structure design

	Support#1	Support#2	Support#3
Build time	178h	142h	349h
Cross Section	square	square	hexagon
Diameter	1.15 mm	1.25 mm	0.4 mm
Critical Angle	46	46	46
Cap Diameter	0.75	0.5	0.2
Cap Height	0.3	1	0.2
Conical Angle	70	70	85
Cluster Spacing	1.4	1.5	0.5
Support Count	3	5	5
Support Spacing	0.87 mm	1 mm	0.5 mm
Area Spacing	1.4 mm	2 mm	0.5 mm
Edge Offset	0.37	0.5	0.1

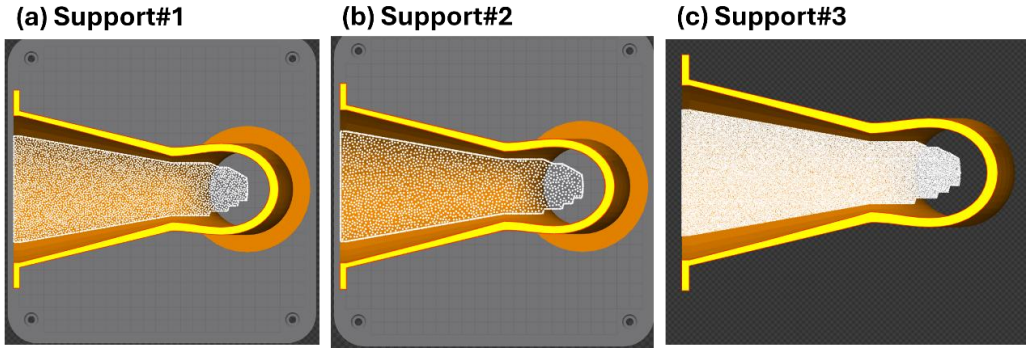

Figure 31. Morphology of support structures with different parameters

Therefore, our focus shifted to refining the parameters that govern support generation. The key parameters are:

- *Support diameter*, which defines the size of individual supports
- *Support spacing and area spacing*, which determine support density.

Support #3 corresponds to QuantAM's default "Fine Support" setting, which produces very dense supports but results in an impractical 349-hour machine time. By refining the support design, Support #2 achieves a more practical balance, requiring 142 hours of build time while maintaining sufficient support density.

The printing will be performed on a Renishaw AM400 system at the Purdue Manufacturing and Materials Research Laboratories (MMRL).

The elbow was oriented in the build configuration shown in Figure 32 to ensure:

- *Recoat stability*: The long axis of the elbow is aligned so the re-coater blade moves along its length, thus reducing the chance of blade crashes or powder piling against tall overhangs.
- *Gas flow clearance*: Positioning the open end of the elbow downstream of the gas flow prevents spatter and condensate trapping in the narrower part of the component.

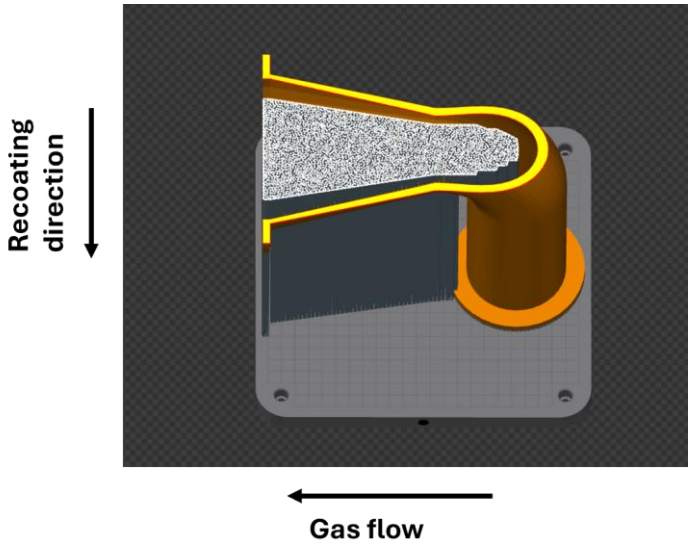

Figure 32. Build configuration of the elbow component

3.2 316H LPBF Cube Parametric Study

Previously, within the AMMT program, researchers at Argonne National Laboratory (ANL), Oak Ridge National Laboratory, and Los Alamos National Laboratory (LANL) focused on optimizing LPBF parameters for 316H SS. Table 16 (Zhang et al. 2024a) compares LPBF build settings used by several laboratories and machines. It shows both pulsed (Renishaw AM400) and continuous (GE Concept Laser and EOS M290) modes, with laser powers from 195 to 290 W and spot sizes of 70–130 µm. Scan speeds range from 0.58 to 1.5 m/s, hatch spacing from 75 to 140 µm, and most builds use a 50-µm layer height and a 67° rotation, except the LANL/EOS M290 case with a 30-µm layer and 47° rotation. The resulting volumetric energy

densities span roughly 52–95 J/mm³, with most builds in the 52–76 J/mm³ range and the LANL/EOS M290 condition producing the highest value.

Table 16. Machine, site, build designation, laser mode and printing parameters used in this study (Zhang et al. 2024a)

Lab/ machine	Build designation	Laser mode	Laser Power (W)	Spot size (µm)	Scan speed (m/s)	Hatch spacing (µm)	Layer height (µm)	Rotation angle (°)	Energy density (J/mm³)
ANL/Renishaw AM400	ANL-B1; ANL-B2	Pulsed	195	70	0.67	110	50	67	53
ORNL/GE Concept Laser	ORNL-B1	Continuous	200	125	0.75	75	50	67	71
ORNL/GE Concept Laser	ORNL-B2	Continuous	290	130	1.5	75	50	67	52
ORNL/Renishaw AM400	ORNL-ANL-best	Pulsed	195	70	0.67	110	50	67	53
ORNL/Renishaw AM400	ORNL-ORNL-best	Pulsed	200	70	0.58	90	50	67	76
LANL/EOS M290	LANL-B2	Continuous	275	100	0.69	140	30	47	95

A detailed process parameter study was carried out at ANL (Zhang et al. 2023). Figure 33 shows the details of the process parameter optimization results. Sample #51 represents one of the “sweet-spot” processing conditions on the screening plate (Figure 33a). In the laser power–scan speed map in Figure 33(b), it sits in the cluster that yields the lowest defect content, at a moderate laser power and scan speed that balance lack-of-fusion and keyholing. Metallography of #51 in Figure 33(c) shows only 0.05% porosity, indicating nearly full density. The EBSD map in Figure 33(d) reveals a fine, heterogeneous but largely equiaxed grain structure without a dominant texture, consistent with stable melt-pool solidification. Overall, sample #51 is an optimized LPBF setting that produces clean, well-consolidated material and is a strong candidate for baseline mechanical testing.

Furthermore, the ANL study by (Zhang et al. 2023) found that despite chemistry variations among several powder batches within specification, the optimal printing window was essentially unchanged, and the resulting parts displayed similar tensile behavior from room temperature to 750°C. For the current study, the following process parameter mentioned in Table 17 will be used that was used in AMMT program (Zhang et al. 2023).

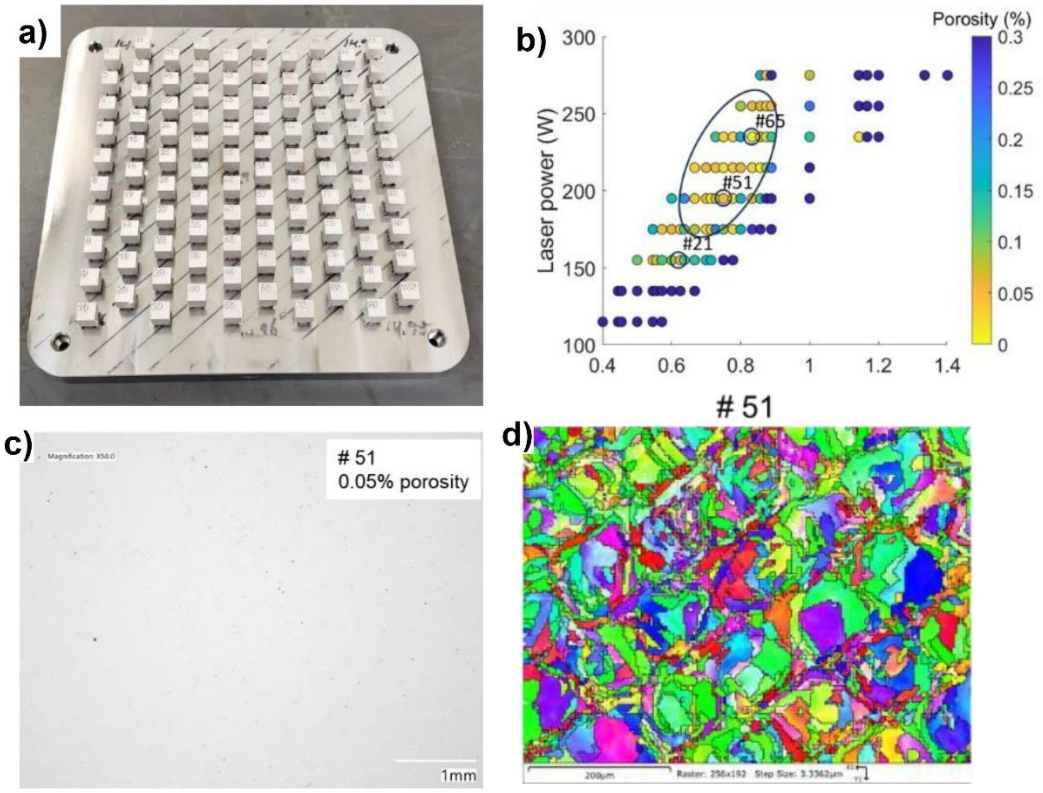

Figure 33. Parameter development and characterization of LPBF 316H coupons. a) Build plate with a matrix of cubic coupons printed across a range of parameters. b) Process map of laser power versus scan speed with porosity (%) shown by color; the low-porosity window is outlined and the selected setting (#51) is indicated. c) Polished cross-section of coupon #51 with 0.05% porosity, d) EBSD inverse pole figure map of coupon #51 showing the as-built grain structure (Zhang et al. 2023)

Table 17. Optimized LPBF process parameters for 316H

Laser Power (W)	Laser spot size (µm)	Point Distance (µm)	Exposure Time (µs)	Hatch Spacing (µm)	Rotation Angle (deg)	Layer Thickness (µm)
195	70	60	80	110	67	50

A parameter study was carried out to optimize the laser parameter for the received 316H SS powder. 10 × 10 × 10 cubes were built for density assessment. Table 18 shows results that confirm the parameters samples #5 and #6 can produce high-density samples. Figure 34 shows the appearance of the samples. Sample #5 parameters also were recommended by ANL for mechanical testing (Zhang et al. 2023). Therefore, sample #5 parameters were down selected for elbow component fabrication in this task.

Table 18. Laser parameter study of 316H stainless steel

	Scan Strategy	Laser Power(W)	Layer Thickness (um)	Hatch Spacing (um)	Point Distance (um)	Exposure Time (us)	Effective Speed (m/s)	Volume Heat Input (kJ/mm3)	Linear Heat Input (J/m)	Relative density (%)
#3	Meander	195	50	110	60	70	0.86	41.36	227.50	99.83
#4	Meander	195	50	110	60	75	0.80	44.32	243.75	99.2
#5	Meander	195	50	110	60	80	0.75	47.27	260.00	99.96
#6	Meander	195	50	110	60	85	0.71	50.23	276.25	99.97
#7	Meander	195	50	110	60	90	0.67	53.18	292.50	99.92
#8	Meander	195	50	110	60	95	0.63	56.14	308.75	99.96

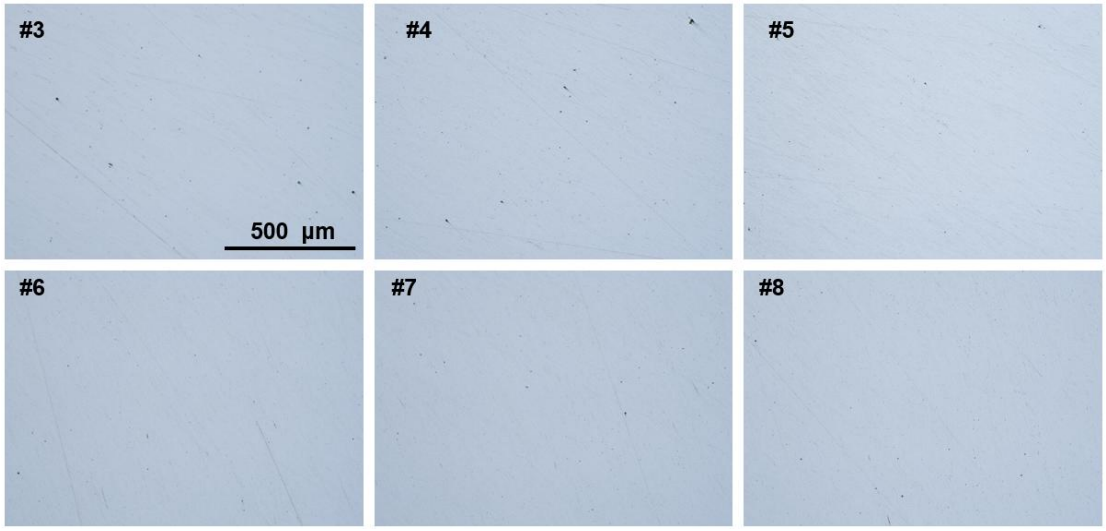

Figure 34. Optical micrograph showing the density of AM 316H produced using the laser parameters in Table 18.

3.3 316H LPBF of 0.4 Extended Elbow Component

The 316H SS powder used in this study was procured from Sandvik®. The powder was produced using gas atomization, resulting in spherical particles with an average size of 45 µm. The chemical composition of the 316H powder is detailed in Table 19, which shows compliance with standard specifications for this austenitic SS grade. Critical interstitial element contents were measured and found to be within acceptable limits: the nitrogen content was 0.026%, and oxygen content was 0.017%.

Table 19. Chemical analysis of the 316H powder provided by Sanvik®

C	Al	Si	P	S	Ti	Cr	Mn	Fe	Ni	Mo
0.07	<0.01	0.50	0.009	0.004	0.01	17.1	0.91	67.0	11.9	2.39

Figure 35a shows the machine setup for the LPBF printing job. Two cameras were mounted to view the build plate and the Renishaw LPBF control panel, enabling remote supervision and layer by layer video capture for post process analysis. Figure 35b is a snapshot of the LPBF process in action, showing the interior of a Renishaw AM400 powder-bed fusion system. The bright circular feature visible in the center of the build platform represents the laser actively scanning and melting the 316H SS powder according to the programmed geometry. This snapshot is taken from a comprehensive 15-hour video recording of the entire build process,

which will be analyzed later to understand detailed process dynamics and layer-by-layer progression and to identify any anomalies or variations that may have occurred during manufacturing. Recycled powder was used to reduce material consumption; the recycled-to-fresh powder ratio for each of the five refills was recorded over the 6 day-print and varies from 30kg to 17 kg used powder) as well as the build height (layer number) at each powder refill was recorded. This will further be utilized when the characterization of the printed part is analyzed in FY26.

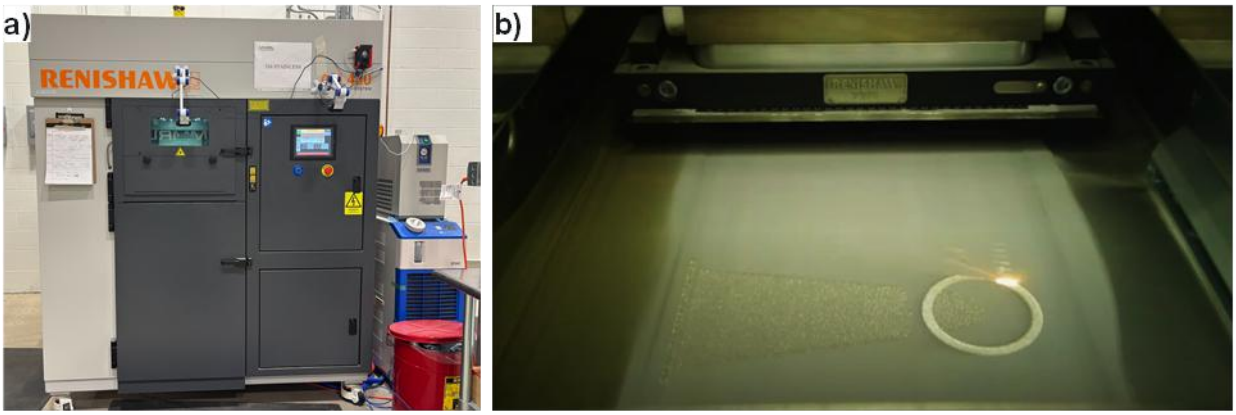

Figure 35. Renishaw AM400 equipment printing a mock-up elbow component in 316H steel.

Figure 36(a-e) shows the completed component. The build ran to completion without interruption and the part was sized to nearly fill the build envelope (248 × 248 × 285 mm). Overall quality is high, but the support at the large elbow-flange opening delaminated from the part. The root cause is under investigation; likely contributors include (1) spatter/residual buildup along the part edge, (2) the heavy weight of the side near large elbow flange, (3) non-uniform powder spreading near the edge of the build plate. Ongoing work will further assess part quality and compare the effects of recycled versus fresh powder.

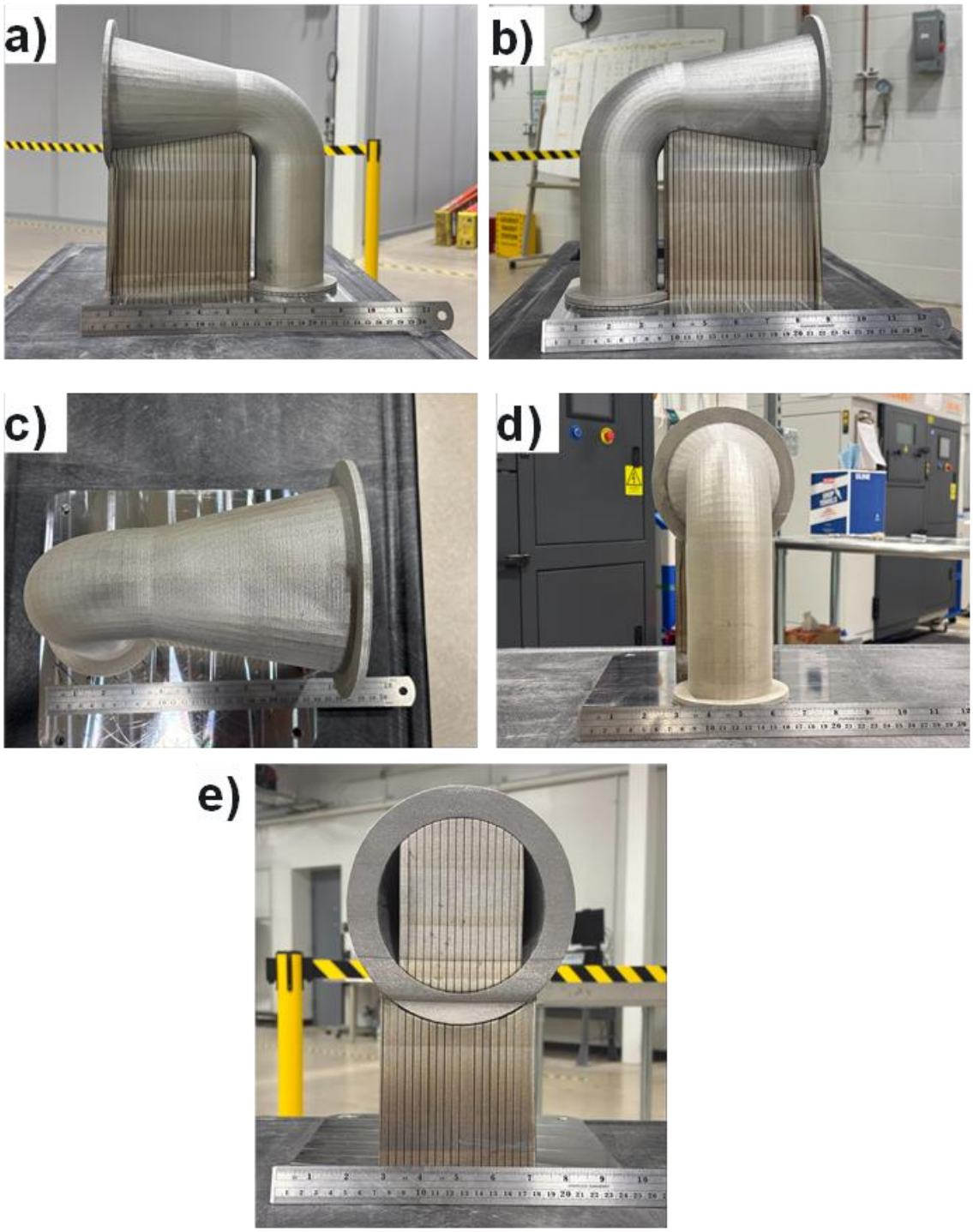

Figure 36. Laser powder bed fusion fabrication of the 0.4 extended elbow componenet. a) Renishaw LPBF machine used for the build. b) Side view of the as-built part on the baseplate showing the tall block supports that carry the overhanging elbow. c) Opposite side view. d) Top view highlighting the wall contour. e) End view. f) End view of the supported end with the support block visible through the bore. Rulers are included for scale.

4 Wire DED

Although not part of the current project, PNNL team printed a 316L SS cylinder as part of the in-house training procedure for the new equipment. A 316L SS cylinder was printed using PNNL's newly acquired in-house wire DED AM equipment, the Meltio Engine CNC Integration w/Phillips 3-axis Additive Hybrid machine. The machine is equipped with a 1.2-kW infrared laser source and a controlled Argon inert gas environment. Feedstock consumables range from 0.8–1.2 mm wire from either BS300 spools or wire drums (Figure 37).

Figure 37. Image of the Hybrid wire-DED equipment at PNNL.

The cylinder is modeled using Solidworks (Dassult Systemes) at 7.45 inches tall, 5.33-inch OD, 5.09-inch ID, 2.59-inch inner fillet, and a 3.73-inch bottom opening ((Figure 38a-b). The cylinder is printed at 800 W laser power, 0.0373-inch layer height, 0.040-inch wire diameter, and 16.8-mm/s wire feed rate (Figure 38c-d).

A high thermal gradient (dark blue color) was observed at the part-build plate interface along with build plate warpage on the bottom part. This suggests the presence of high residual stress in the part and plate, which could raise concerns regarding how the part will react to EDM cutting. A suggestion is to increase the build plate thickness from 0.5 to 1.0 inches to minimize residual stress effects. The print file initially had the cylinder height value set at a dimension that was not a multiple of 0.0373 inches per layer. This resulted in overbuilding and part failure. The cylinder height was revised to accommodate for the layer height restriction, resulting in a complete cylinder build. The printed part highlights the printer's ability to print tall and large parts. In addition, it is the tallest part built. In short, this section demonstrates PNNL's new AM capabilities to further AMMT's mission and future tasks and collaboration, if the program decides to pursue this further, particularly to build this cylinder in the same dimensions using 316H SS wire and the elbow pipe geometry mock-up.

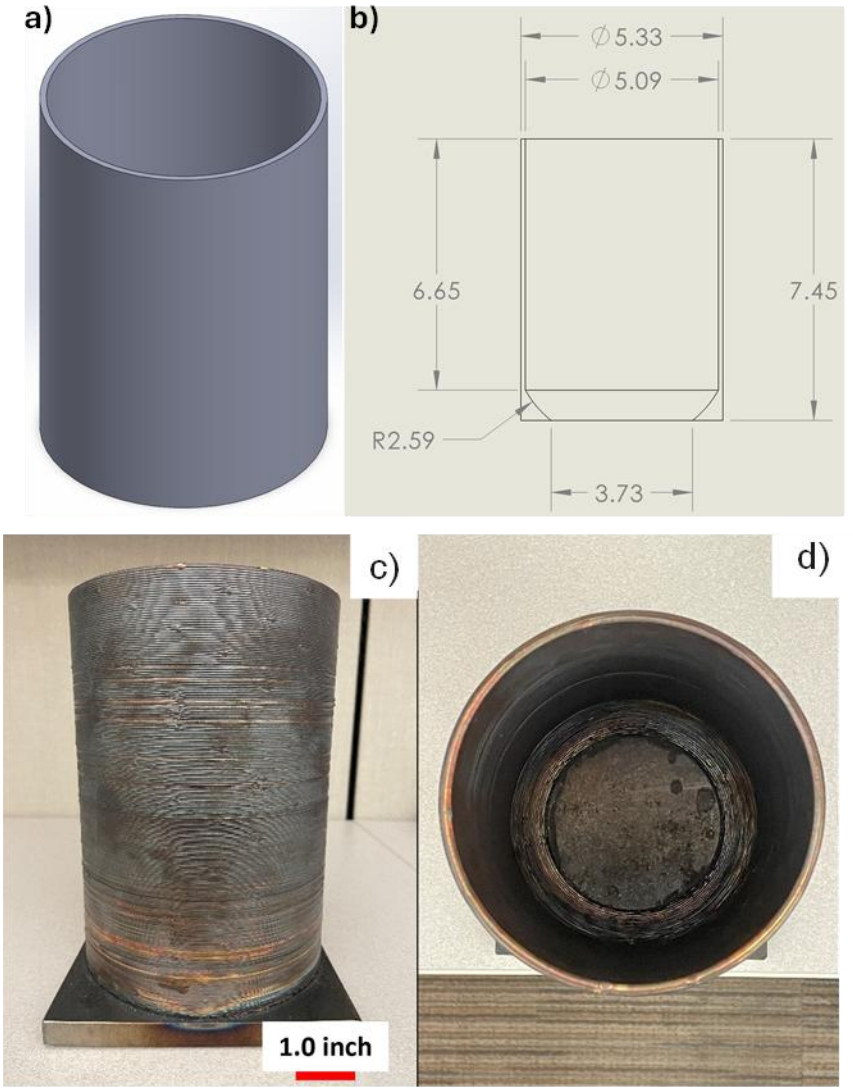

Figure 38. a) 316L SS cylinder side view, b) Cylinder top view, c) Lower view of the cylinder-build plate interface.

5 Finite Element Modeling Prediction of Resulting Residual Stresses in Additively Manufactured Components

In FY25, a modeling process was developed for the simulating DED and LPBF fabrication processes for residual stress predictions in a 316H SS cylinder of varying wall thickness. The part also was fabricated experimentally at Purdue University using wire DED processes. In future work, we intend to fabricate the same cylinder using LPBF processes. This part then will be used to validate results from the model. In this section, the effect of DED and LPBF fabrication processes are investigated for residual stress and distortion in the part.

5.1 Experimentally Fabricated 316H Cylinder

This section introduces the experimentally fabricated 316H SS cylinder that is intended for future model validation. Figure 39 illustrates the cross-sectional geometry of the 316H SS cylinder and associated print bed (baseplate).

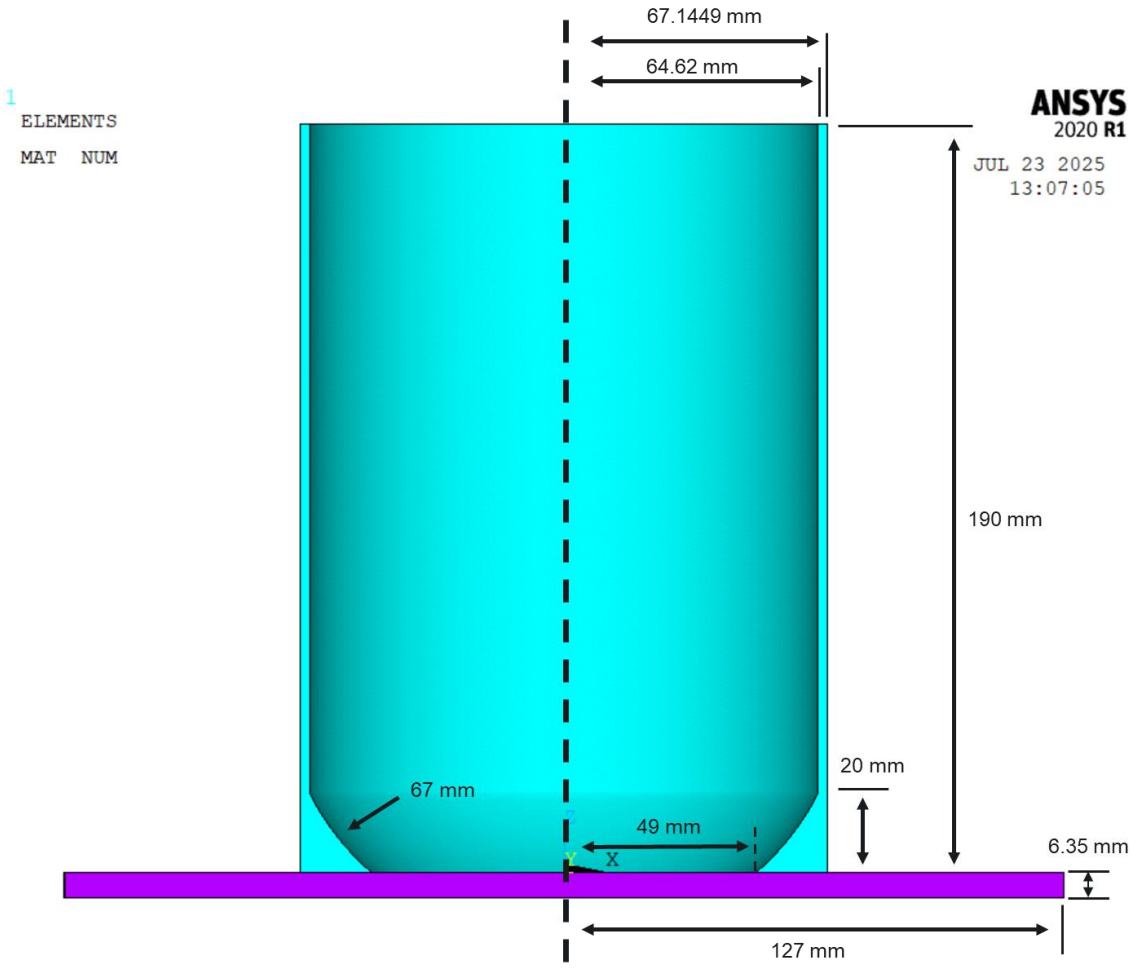

Figure 39. 316H SS cylinder geometry

The cylinder is unique in that it has varying wall thickness and inner radius in the lower portion of the part. The upper portion of the part has constant wall thickness and inner and outer radius. The lower-most inner and outer radius are 49 mm and 67.1449 mm, respectively. The varying wall thickness of the lower portion of the part is described by a curved inside wall of radius of 67 mm. The lower portion of the geometry transitions to a constant inner and outer radius at a height of 20 mm. The constant inner and outer radius are 64.62 mm and 67.1449 mm, respectively. The overall height is 190 mm. The baseplate was 254 mm in length and 254 mm in width with a thickness of 6.35 mm. The DED experimentally fabricated cylinder was fabricated with a mean laser commanded power of 699.9 W, and the mean scan speed was 9 mm/s and 22.2 mm/s for the contour pass and infill pass, respectively. See Section 5.2.1.3 for a description of the contour and infill passes and a simplified description of the G-CODE build path for the DED fabricated cylinder.

5.2 Finite Element Modeling for DED and LPBF Fabrication Processes

This section introduces the finite element modeling effort for DED and LPBF fabrication processes. This work aims to develop a modeling methodology/framework for the simulation of transient temperature fields and corresponding macro residual stresses in microreactor parts fabricated through DED and LPBF. The modeling process attempts to simulate the entire build process of the part as well as post-build cooling and baseplate removal. The simulation of such processes could provide valuable insight into the optimum build parameters to reduce residual stress and distortion of the part prior to fabrication. These build parameters include deposition size, deposition speed, deposition pattern, ambient environment conditions, baseplate preheat conditions and other build specific thermal transient events. The adopted approach to the simulation of DED and LPBF fabrication processes was inspired by the approach used by the ANSYS Additive Manufacturing Suite (ANSYS Additive Manufacturing, Release 2025 R2, LPBF Simulation Guide; ANSYS Additive Manufacturing, Release 2025 R2, DED Simulation Guide). The approach is described below.

5.2.1 Transient Thermal Model

This section introduces the transient thermal model used to predict the temperature fields from the building process of the 316H cylinder described in Section 5.1 using DED and LPBF. The modeling approach is subdivided into two sequential analyses: a transient thermal analysis and a static structural analysis. The transient thermal analysis serves to predict the transient temperature fields from material deposition and post-build cooling. The static structural analysis (Section 5.2.2) is then used to predict the evolution of residual stresses from the transient temperature fields solved in the transient thermal analysis. Both analyses were conducted using the commercial finite element software ANSYS Mechanical APDL 2020 R1. The remainder of this section will discuss the transient thermal model in detail. The geometry, loads and boundary conditions, contact conditions, and material properties are presented.

5.2.1.1 Geometry and Mesh

The geometry of the 316H cylinder is discussed previously in detail in Section 5.1. The finite element mesh for both the DED and LPBF simulations is shown in Figure 40.

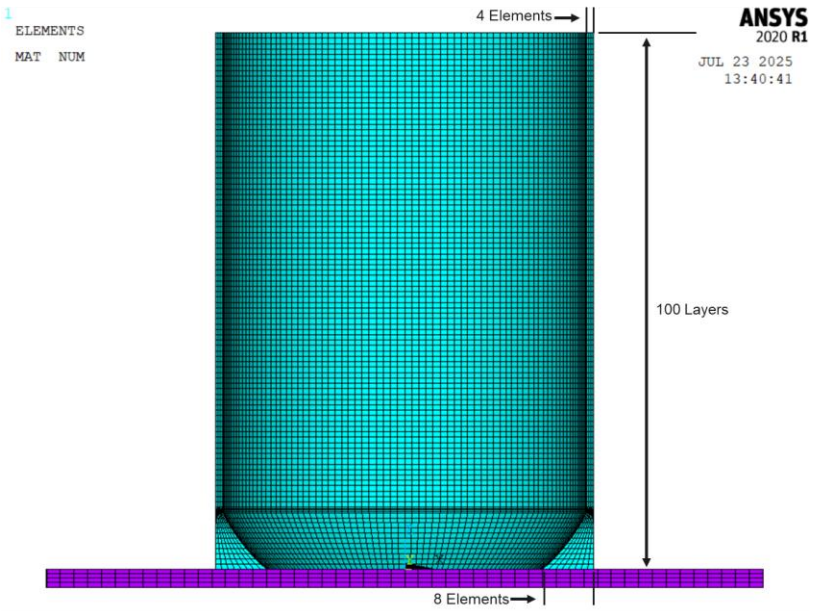

Figure 40. 316H SS cylinder finite element model geometry and mesh

The height of the cylinder was discretized into 100 through-height element layers. The lower region of the part was discretized with 8 through thickness elements which transition to four through-thickness elements in the upper, constant wall thickness of the part. The entire part was discretized into 160 elements around the circumference. It is noted that the discretization of the mesh and through-height build layers is coarse in comparison to the material deposition size in the experimentally fabricated cylinders. Future work is intended to validate that an approximate global stress behavior is accurately captured with this coarse representation. The baseplate was discretized with four through-thickness elements and a planar mesh size of 4.9 mm.

Temperature-dependent thermal material properties for 316L SS were implemented in the analyses. The use of 316L SS material properties for 316H is suitable being their thermo-mechanical properties are similar. The cylinder and baseplate are assumed to share the same material properties. A tabulated list of the thermal material properties is given in Table 20.

Table 20. 16L SS thermal material properties (Kim 1975)

Temperature (K)	Thermal Conductivity $\frac{W}{m \cdot K}$	Heat Capacity $\frac{J}{kg \cdot K}$	Density $\frac{kg}{m^3}$
300	13.96	498.97	7,954.00
400	15.53	512.37	7,910.00
500	17.10	525.76	7,864.00
600	18.68	538.74	7,818.00
700	20.25	552.13	7,771.00
800	21.82	565.53	7,723.00
900	23.39	578.92	7,674.00
1,000	24.96	591.90	7,624.00
1,100	26.53	605.30	7,574.00
1,200	28.10	618.69	7,523.00
1,300	29.67	632.09	7,471.00
1,400	31.25	645.06	7,419.00
1,500	32.82	658.46	7,365.00
1,600	34.39	671.85	7,311.00
1,700	35.96	685.25	7,256.00

5.2.1.2 Element Types

The 3D solid elements that comprise the 316H cylinder and baseplate were generated using SOLID278 elements. Default element key options were used for the SOLID278 elements.

The thermal contact between the 316H SS cylinder and baseplate was employed using CONTA174 elements on the bottom of the 316H SS cylinder and TARGE170 elements on the top of the baseplate. The convection on the top of each through-height layer was employed using SURF154 elements overlayed on the top of each through-height layer.

5.2.1.3 Loads and Boundary Conditions

The build process of the part is simulated using the element birth-and-death technique, and the geometry of the part is subdivided into a series of deposition segments that are activated according to the fabrication process of interest. In the DED simulation, the deposition segments are activated according to the scan deposition path across a layer. In the LPBF simulation, each through height layer is activated at once (i.e., no path followed).

The deposition segments and build path for the DED simulation was approximated using G-CODE from the experimentally fabricated cylinder. An approximation of the G-CODE path was implemented due to computational efficiency and the coarse representation of the finite element mesh but captures some of the main features of the build path. The build path for the DED simulation differs between the lower, variable wall thickness of the part and the upper, constant wall thickness of the part. The DED build path for the lower and upper portion of the part is shown in Figure 41(a) and (b) respectively.

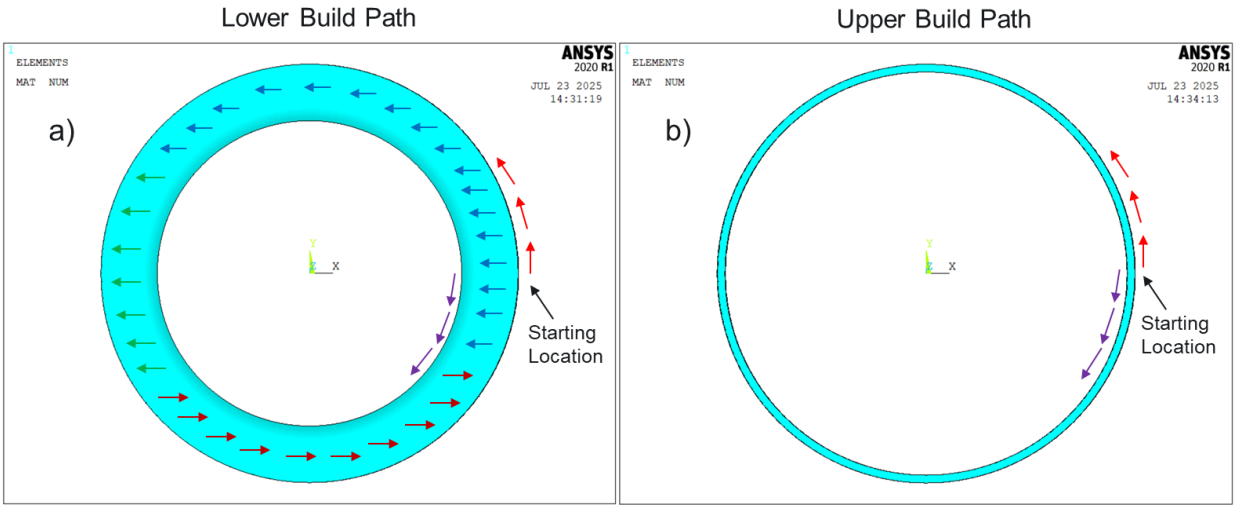

Figure 41. DED Deposition paths. Lower Build Path (a) and Upper Build Path (b)

At the starting location, the lower portion of the build begins with an outside contour pass (counterclockwise), followed by an opposite direction inside contour pass (clockwise). The inside backfill path begins at the starting location side, inside the previously activated outside/inside contours. Backfill progresses horizontally (-X direction) along the starting location side and upper (+Y) side of the cylinder until the opposite inside radius is reached. This is termed Inside Backfill Path 1. The backfill then moves to the lower (-Y) opposite side of the cylinder and progresses horizontally in the opposite (+X) direction (Inside Backfill Path 2) until the backfill reaches the activated segments from Inside Backfill Path 1. Lastly the backfill moves to the ending/starting locations of Backfill Path 1 and 2 and activates the segments in the left portion of the cylinder in the (-X) direction (Inside Backfill Path 3). Upon completion of a layer, the starting location rotates 90° counterclockwise, the outside and inside contour directions are switched, and the process is repeated for the next layer. This process continues until the wall thickness of the part is less than twice the constant wall thickness of upper portion of the part. The build path then switches to the upper build path which begins with an outside contour pass and finished with an alternate direction inside contour pass. It is noted that the initial starting location for the upper build path begins at 90° counterclockwise to the starting location of the last layer of the lower build path. Further, the initial direction of the contours is switched from the directions of the last contour layer of the lower build path. Upon completion of a layer, the starting location rotates 90° counterclockwise, the outside and inside contour directions are switched, and the process is repeated for the next layer. It is noted again that the implemented build path is a simplification of the G-CODE used for the experimentally fabricated cylinder. The G-CODE path for the experimentally fabricated cylinder is of much higher resolution due to the small melt pool size. Further, the contour fill and infill starting locations do not always align and the starting locations for these paths occur at more locations around the circumference of the part, as opposed to the four, 90° counterclockwise spaced starting locations implemented in the finite element model. The purely counterclockwise rotations of the starting points in the finite element build path is also an assumed simplification.

The deposition segments for the DED simulation were activated according to a deposition speed of 9 mm/s for the outside/inside contours and 22.2 mm/s for the infill. Once activated, the elements were held at melt temperature (1,375°C) for a duration of time that corresponds to the speed, direction, and size of the segment to mimic the advancing melt pool. The deposition segment size for the outside/inside contours was a 45° segment around the cylinder, two elements in width. The deposition time for each outside/inside contour segment was approximated as the arc length of the segment divided by the deposition speed. The deposition segment size for the infill was the full vertical length of elements (as illustrated in Figure 41(a)) whose centroid exists in each width of backfill for each backfill stage (within a tolerance of 1e-2 mm). This width was determined by the wall thickness of the layer. If twice the radial width of an element in a layer is less than the upper wall thickness of the part, then the width of the infill segment was the upper wall thickness. Otherwise, the width of the infill segment is twice the radial width of an element in the layer. The deposition time for each infill segment was approximated as the linear length (Minimum Y nodal coordinate to maximum Y nodal coordinate) of the segment divided by the deposition speed. It is noted that the deposition segment time for the DED simulation does not account for the height or volume of the layer which contributes to a source of error in the time estimation.

The deposition layers for the LPBF simulation were activated according to an approximate layer completion rate of 0.5 layer/min. Once activated, the elements were held at melt temperature (1,375°C) for a duration of time that corresponds to the completion of the layer. The layer completion time was calculated using the volume of elements in a layer with a volumetric rate derived from a 0.5 layer/minute rate, a 50-um layer thickness, and the cross-sectional area of the upper, constant wall thickness portion of the cylinder.

When the deposition time for a DED segment and LPBF layer completes, the melt temperature boundary condition is released, and the segment is allowed to cool according to the ambient environment and adjacent material.

The ambient environment was assumed to be air at 25°C with a film coefficient equal to $10\ \frac{W}{m^2K}$. Convection boundary conditions were applied to the interior and exterior edges of the cylinder via nodal loads, as well as to the top of each through-height layer via convection elements. The convection boundary conditions become active once the material is deposited. The convection boundary condition is then deactivated once a subsequent layer is deposited onto the active layer.

Heat transfer between the part and the baseplate is achieved through thermal contact elements and a thermal contact conductance which is assumed to be perfectly conductive. The entire baseplate is prescribed an 80°C initial temperature condition at the beginning of the analysis, and the bottom of the baseplate was prescribed a constant pre-heat temperature of 80°C. The bottom of the baseplate pre-heat temperature remains constant for the entire analysis. Convection boundary conditions, equivalent to those described above, were applied to the top of the baseplate (excluding the region where the cylinder is bonded to the baseplate) via nodal loads. No convection boundary conditions were applied on the outer edges of the baseplate. After the build process is completed, the part is allowed to cool for a duration of 2 hours.

5.2.2 Static Structural Model

This section introduces the static structural model used to predict the residual stress field and part distortion from the building process of the 316H SS cylinder using DED and LPBF. The static structural model receives the temperature fields from the transient thermal model as inputs during the simulated build process. The geometry, loads and boundary conditions, contact conditions, and material properties is discussed in detail.

5.2.2.1 Geometry

The geometry and mesh for the static structural model are equivalent to the transient thermal model (Section 5.2.1.1).

5.2.2.2 Material Properties

Temperature dependent mechanical material properties for 316L were employed in the analysis. The use of 316L SS material properties for 316H SS is suitable as their thermo-mechanical properties are similar. The baseplate was simulated using a purely linear elastic material model. The cylinder was simulated as an elastic-plastic material that employed the Von-Mises isotropic hardening material model. Temperature-dependent bilinear hardening curves were employed for the plasticity model. A tabulated list of the mechanical material properties is given in Table 21 (Nickel Institute, 2020, Sandmeyer Steel Company 2014). No extrapolation is made for materials beyond the reported temperatures.

Table 21. 316L SS mechanical material properties (Nickel Institute, 2020, Sandmeyer Steel Company 2014)

Temperature (K)	Youngs Modulus (GPa)	Yield Strength (MPa)	Hardening Slope (MPa)	Mean Coefficient of Thermal Expansion (cm/cm/°C)	Poisson Ratio
300.15	193	290	579.74	16.6	0.25
422.15	190	201	597.42	16.80	-
533.15	181	172	676.82	17.24	-
644.15	172	159	726.96	17.68	-
755.15	162	148	716.29	18.13	-
866.15	153	140	710.57	18.42	-
977.15	143	131	498.74	18.69	-
1089.2	132	110	181.31	18.96	-
1,273.15	-	-	-	19.40	-

5.2.2.3 Element Types

The 3D solid elements that comprise the 316H cylinder and baseplate were generated using SOLID185 elements. Default element key options were used for the SOLID185 elements.

The bonded contact between the 316H cylinder and baseplate was implemented using CONTA174 elements on the bottom of the 316H cylinder and TARGE170 elements on the top of the baseplate.

5.2.2.4 Loads and Boundary Conditions

The simulated build process for the static structural model is equivalent to the transient thermal model. The build process is simulated by activating a series of deposition segments or layers according to the fabrication process of interest. However, special care is necessary to ensure that the activated segments or layers are activated in a thermal strain-free condition. To achieve this, the temperatures at the end of each activation step are imported and solved for first, followed by the activation of the intended segment or layer in the following load step. This ensures that the activated segment/layer and adjacent edges of material are at the melt temperature during activation, providing a thermal strain-free condition. Thermal stresses are then generated from temperature changes in the material after activation and corresponding thermal expansion/contraction.

The baseplate was prescribed a thermal strain-free temperature of 25°C and was fixed in the out-of-plane direction along its bottom surface. Additional minimum boundary conditions were prescribed to the bottom surface of the baseplate to prevent rigid body translation/rotation. Bonded contact was employed to handle the contact between the part and baseplate.

The structural solution was obtained for all activation segments and corresponding temperature fields during the build process of the solution. A total of 20 equally space time solutions were obtained for the cool-down phase. An additional load step is implemented to ensure that the part and baseplate are brought to a uniform 25°C temperature. Finally, the baseplate is removed to achieve the final state of the fabricated part. Minimum boundary conditions were applied to the bottom of the part to prevent rigid body translation/rotation after the baseplate was removed.

Both the DED and LPBF fabrication processes were studied in the static structural model. Gravity was ignored.

5.2.3 Finite Element Model Results

This section presents the simulated results for the 316H cylinder fabricated through DED and LPBF fabrication processes. The simulated time for the build process of the geometry was 2.64 hours and 159.15 hours for the DED build and LPBF build, respectively. Figure 42 shows the layer-wise mean temperature in the part as a function of layer height. The first 100 fabrication steps correspond to the complete deposition of each layer in the fabrication process. As such, the mean temperature was calculated at the completion time for each layer. The fabrication steps beyond step 100 correspond to the cool down of the completed part. We observed that larger through-height temperature gradients and higher temperatures exist at layer completion in the LPBF build compared to the DED build. This is explained by the modeling approach for the LPBF build, in which the entire layer is activated at once at the melt temperature. Figure 43 shows an isometric view of the temperature field at completion of deposition (fabrication step 100). A relatively uniform temperature is observed for each layer along the circumference of the part, aside from the topmost layers of the DED build.

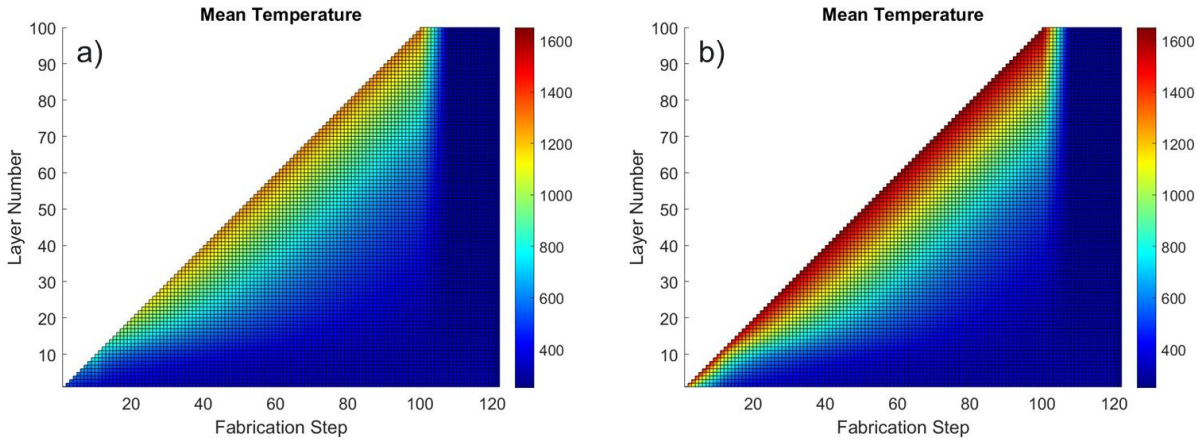

Figure 42. Layer-wise mean temperature (K). DED build (a) and LPBF build (b)

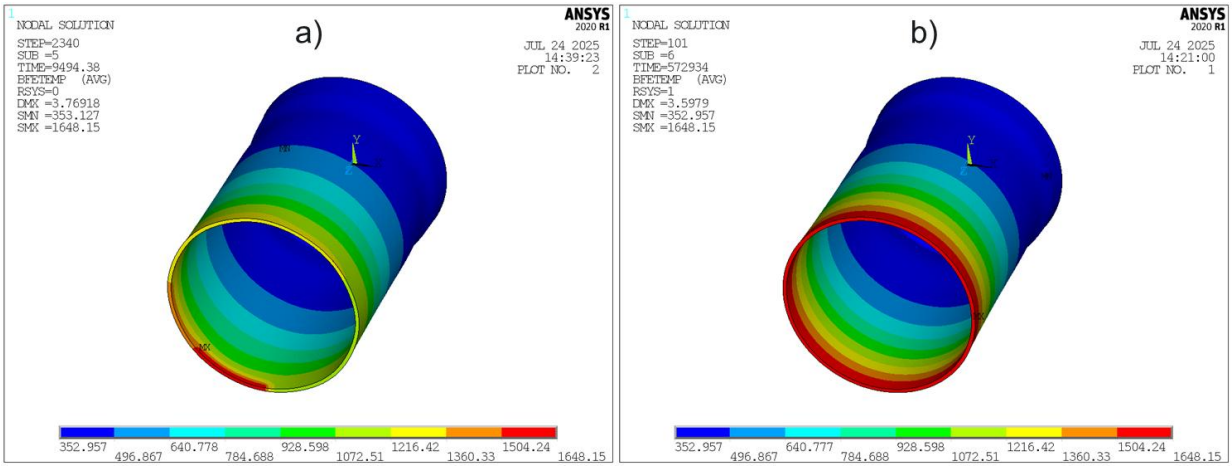

Figure 43. Part temperature (K) at completion of build (fabrication step 100). DED build (a) and LPBF build (b).

Because of the thin wall nature of the part, layer-wise hoop stress was monitored during the fabrication process. To determine if stress gradients exist through the wall thickness, layer-wise average hoop stress at the inner wall, outer wall, and total layer were calculated for each through-height layer. Figure 44 though Figure 46 illustrate the mean hoop stress field for each layer during the fabrication process at the inner wall, outer wall, and total layer, respectively. The first 100 fabrication steps correspond to the complete deposition of each layer in the fabrication process. As such, the mean stress fields were calculated at the completion time for each layer. The fabrication steps beyond step 100 correspond to the cool down of the completed part. The final step corresponds to the baseplate removal.

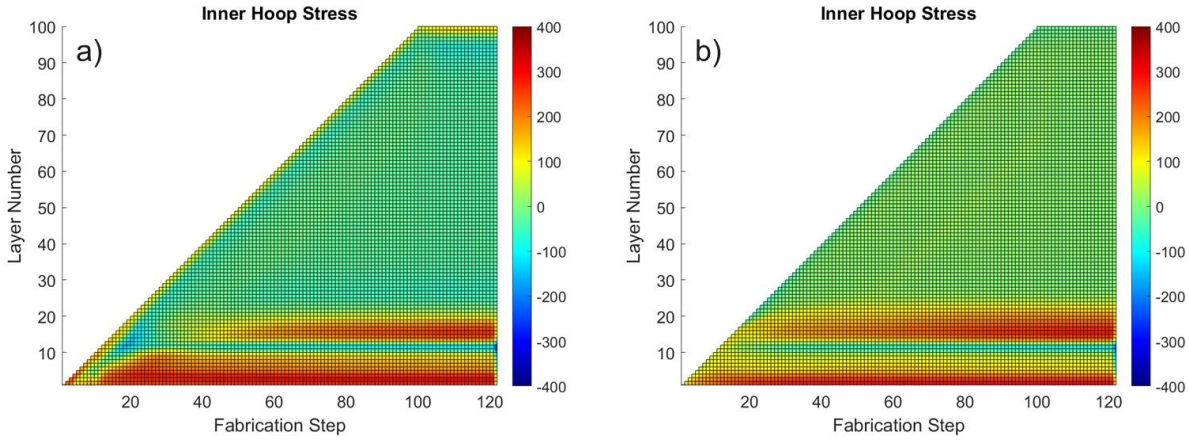

Figure 44. Layer-wise inner hoop stress (MPa). DED build (a) and LPBF build (b).

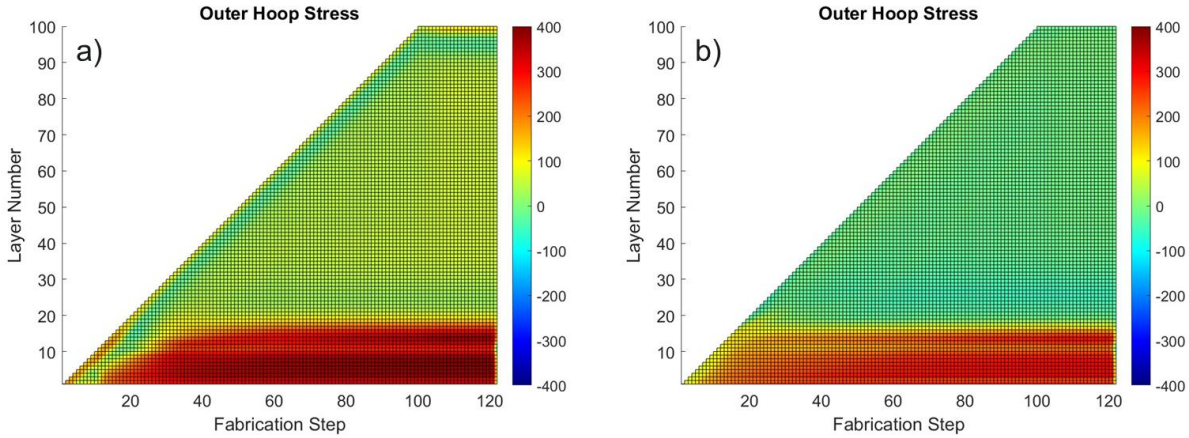

Figure 45. Layer-wise outer hoop stress (MPa). DED build (a) and LPBF build (b).

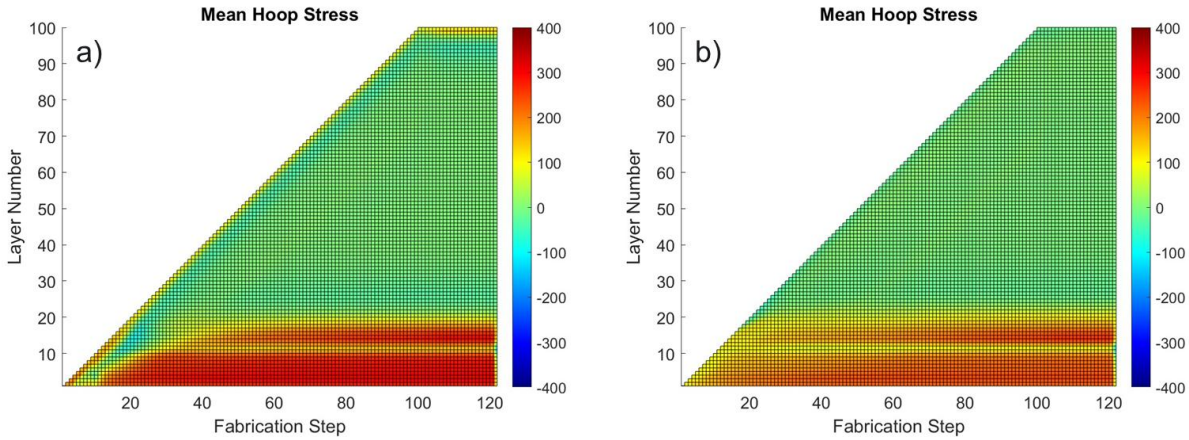

Figure 46. Layer-wise total hoop stress (MPa). DED build (a) and LPBF build (b).

We observed, however, that the DED build experiences more compressive behavior in the upper, inner-wall of the part, and more tensile behavior in the upper, outer wall of the part compared to the LPBF build. Further, higher tensile behavior is experienced in the lower region of the part in the DED build compared to the LPBF build. These differences suggest that the LPBF build results in a lower magnitude stress state compared to the DED build.

The overall global stress behavior between DED and LPBF builds follow similar trends, with varying magnitude. This suggests that the residual stress state in the part is also a function of part geometry. During the deposition and subsequent cooling, through-height hoop stress gradients are present with higher tensile behavior in the lower portion of the build, followed by reduced tensile behavior in the upper portion of the build. Both builds experience a local reduction in the tensile stress state in the lower region of the part near layer 11, which represents the transition between the lower, variable wall thickness region of the part and the upper, constant wall thickness region of the part. This local change in the stress state near layer 11 suggests that geometric changes can have localized stress states in these regions. The topmost layers in DED build experience elevated uniform tensile dominant behavior. The presence of through thickness hoop stress gradients are evident with increased tensile behavior occurring on the outer wall of the part compared to the inner wall, with the maximum stress occurring in the lower portion of the part after cooling, prior to baseplate removal. At the last fabrication step (baseplate removal), both the DED and LPBF builds experience a large reduction in the tensile stress state in the lower portion of the part, indicating a new equilibrium state from the release of the baseplate.

Contours of the hoop stress in the part at the completion of build (fabrication step 100), post-cooling pre-baseplate removal, and post cooling post-baseplate removal are shown in Figure 47 through Figure 49, respectively. The stress behavior through the height of the part for all three states follow the same trends previously discussed, with lower magnitude stress states observed in the LPBF build.

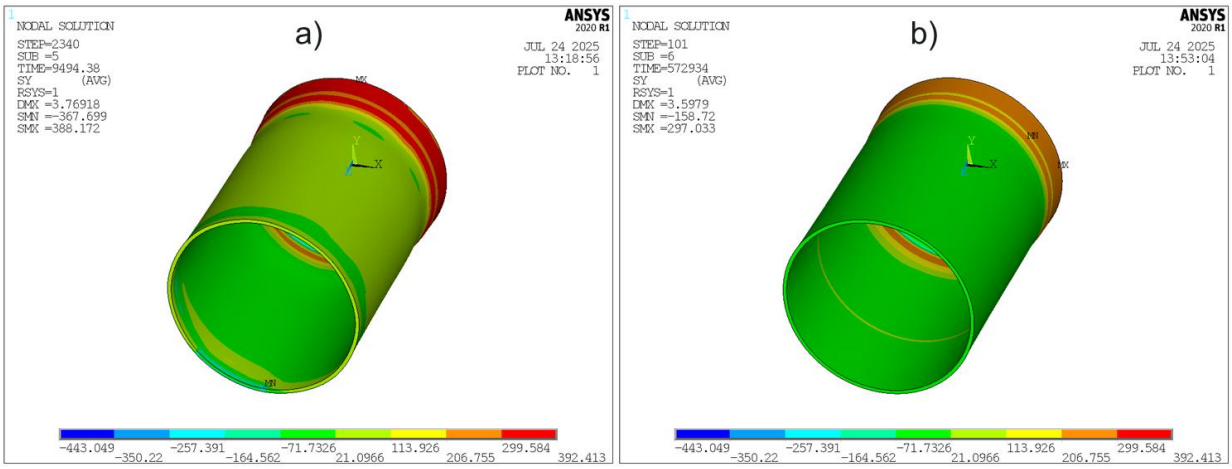

Figure 47. Part hoop stress (MPa) at completion of build (fabrication step 100). DED build (a) and LPBF build (b).

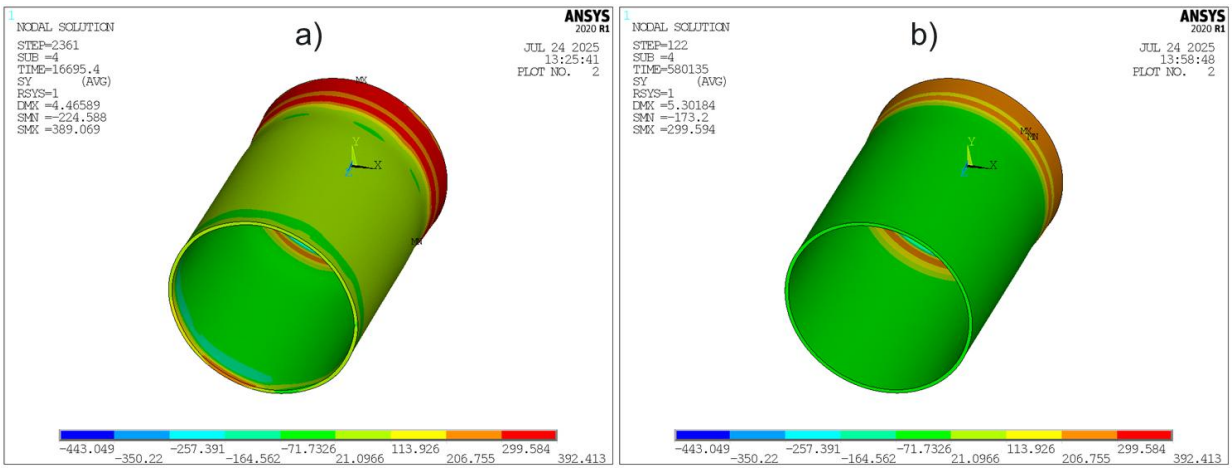

Figure 48. Part hoop stress (MPa) at post-cooling, pre-baseplate removal. DED build (a) and LPBF build (b).

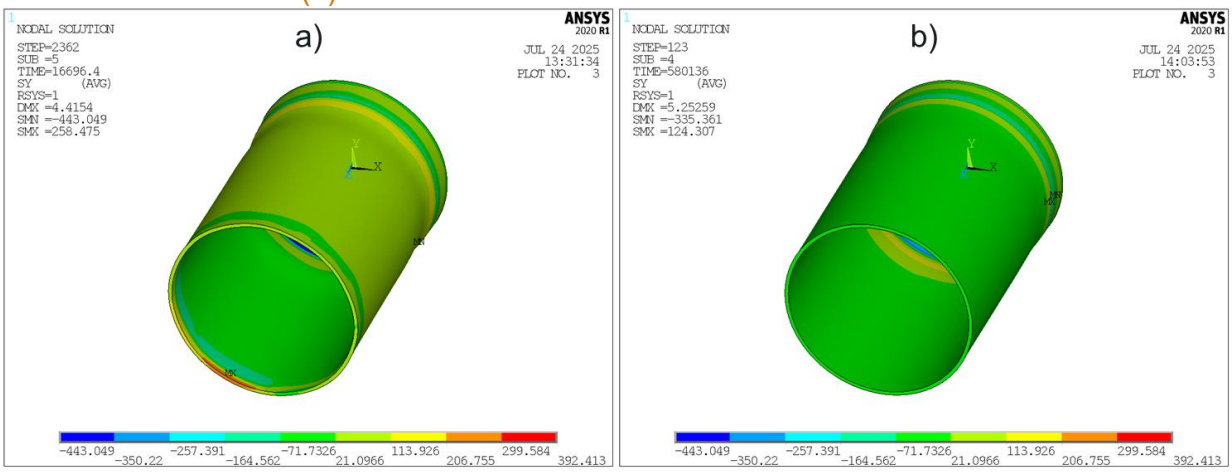

Figure 49. Part hoop stress (MPa) at post-cooling, post-baseplate removal. DED build (a) and LPBF build (b).

The effect of baseplate removal is shown in Figure 50 through Figure 52, which display the layer-wise average hoop stress at the inner wall, outer wall, and total layer for pre and post baseplate removal after post build cooling, respectively. The location of zero stress on the horizontal axis is indicated by a green dotted vertical line. As previously discussed, both the DED and LPBF printed parts experience a large reduction in the tensile stress state in the lower region of the part after baseplate removal, with the lower inner wall in a more compressive state compared to the lower outer wall. The localized stress state occurring near layer 11 is driven completely into compression. This shift in the stress state can be explained by the rigid/welded connection between the bottom of the part and the baseplate, which constrains the part from equilibrium prior to baseplate removal. The upper portion of the part experiences no change in the stress field due to increased distance from the point of constraint.

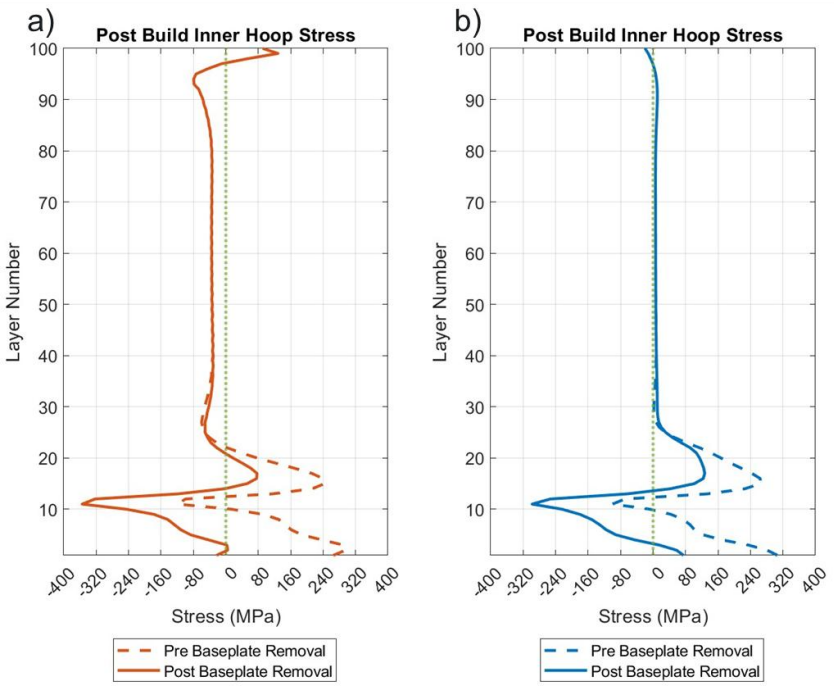

Figure 50. Post-cooling layer-wise inner hoop stress. DED build (a) and LPBF build (b).

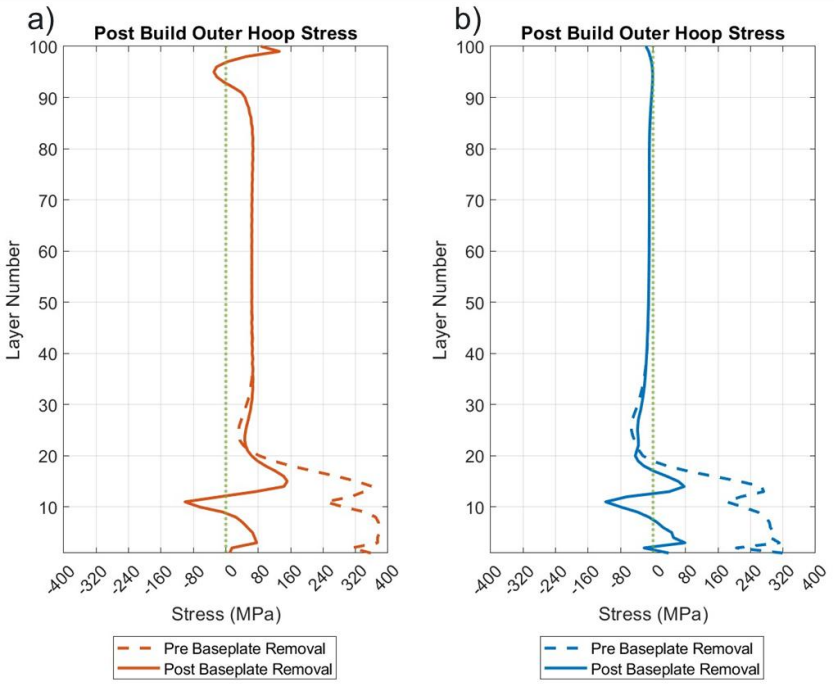

Figure 51. Post-cooling layer-wise outer hoop stress. DED build (a) and LPBF build (b).

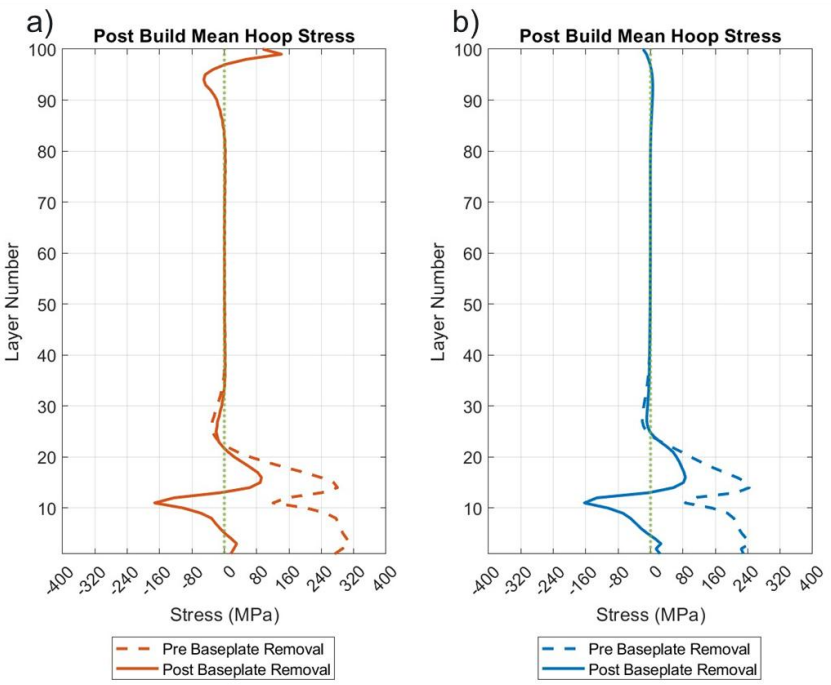

Figure 52. Post-cooling layer-wise total hoop stress. a) DED build and b) LPBF build

The comparative final stress states, both pre and post baseplate removal, are shown on the same axes in Figure 53. The location of zero stress on the horizontal axis is indicated by a green dotted vertical line. After baseplate removal, the DED and LPBF builds share similar stress states in the lower-most region of the part. However, in the upper region of the part, the LPBF build experiences a lower magnitude stress state compared to the DED build, with the DED build being more compressive stress in the inner wall, and more tensile stress at the outer wall. The DED build also experiences elevated tensile behavior in the top-most layers compared to the LPBF build.

Exaggerated final deformed shapes of the DED and LPBF manufactured 316H cylinder after baseplate removal is displayed in Figure 54 and Figure 55, which show a side profile and top view of the part. The contour displays the nodal displacement vector sum. The deformations in these graphics are amplified by 2× the actual deformation. These figures show that the DED build results in lower magnitude but more non-uniform distortion compared to the LPBF build. When the deformations are critical during the part build, this kind of analysis can help direct the fabrication process, build parameters, and deposition paths to create the desired final product.

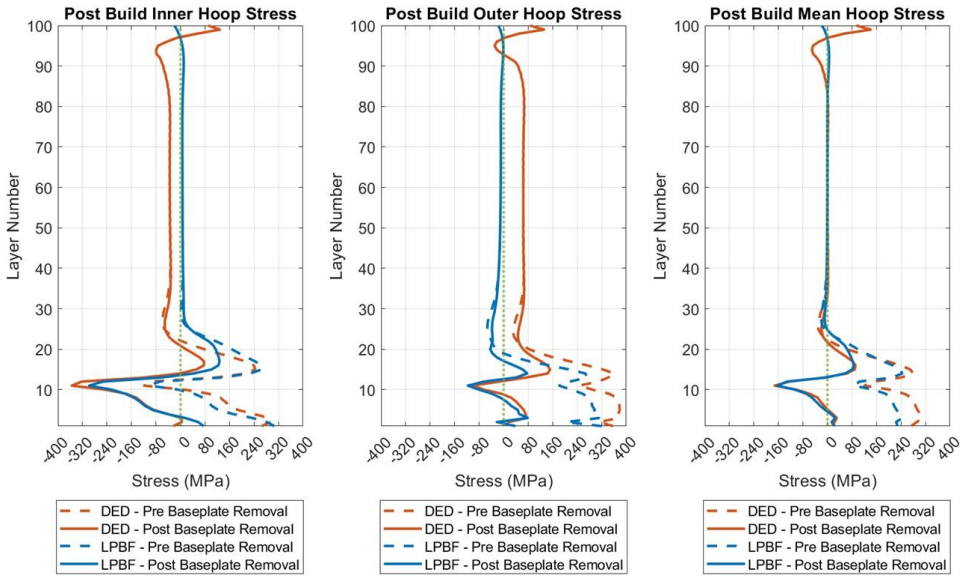

Figure 53. Post-cooling comparative hoop stress

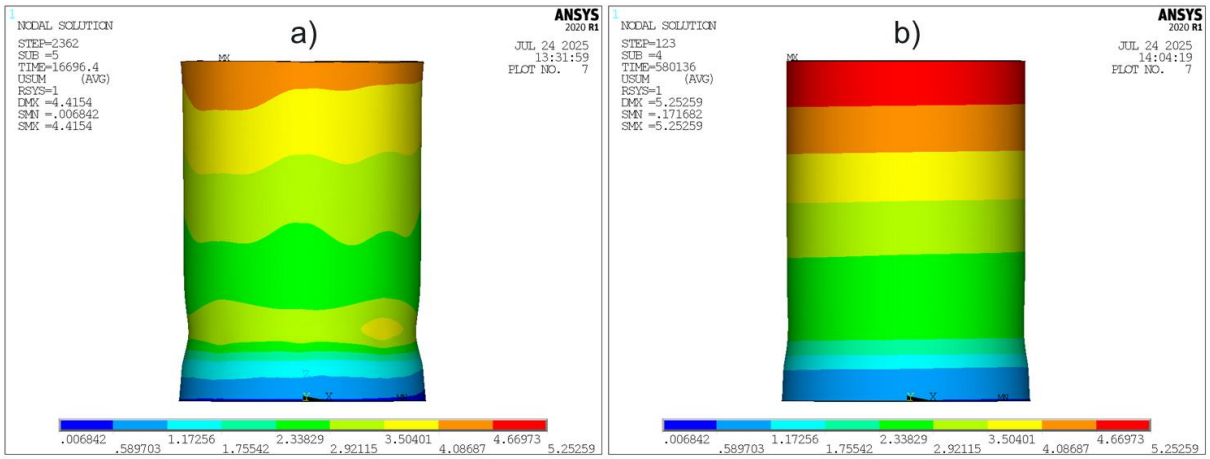

Figure 54. Deformed shape magnified 2x, side profile view. DED build (a) and LPBF build (b).

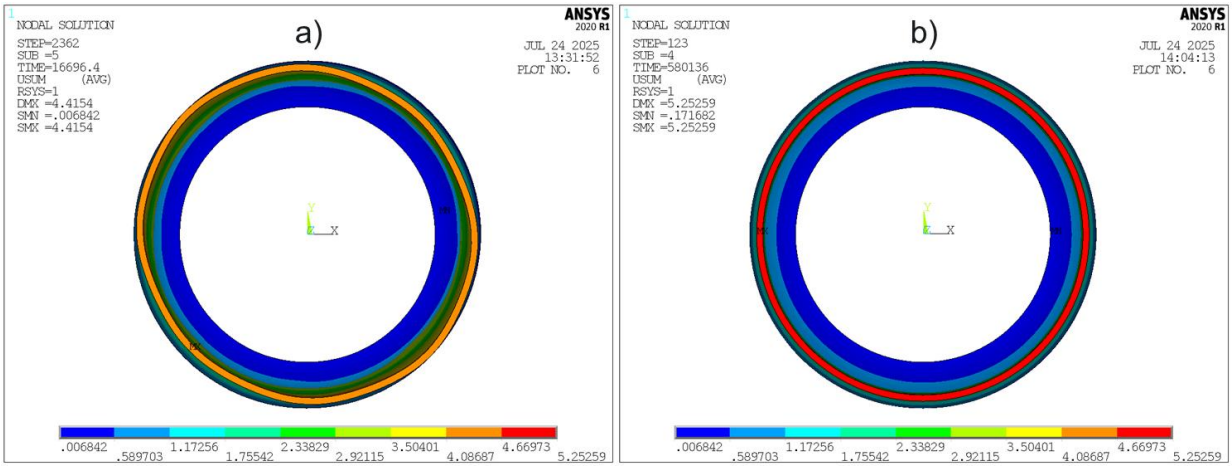

Figure 55. Deformed shape magnified 2x, top view. DED build (a) and LPBF build (b).

5.2.4 Comparison of Finite Element Model Residual Stresses and Experimental Residual Stresses for the DED Fabricated Cylinder

This section presents a comparison of the finite element model residual stress results from the experimentally obtained XRD residual stresses discussed in Section 2.3. The experimentally measured axial and hoop residual stresses of the 316H SS cylinder were recorded at four heights along four, 90° spaced sides of the cylinder. A total of four residual stress measurements were conducted at all locations at different etching depths. The mean etching depth of all measurement locations after the fourth etching was 0.67mm. Figure 56 shows a top view schematic of the residual stress measurement locations used in the finite element model. The finite element model nodal axial and hoop stress was interpolated at 104 equally spaced points along the height of the cylinder at the outside surface and at a depth of 0.67 mm from the outside surface at four, 90° spaced measurements sides. The results were obtained after the baseplate removal step. It is noted that the starting location for the build with respect to the experimentally measured sides is unknown. Therefore, a one-to-one location comparison is not possible, and the chosen sides used in the finite element model are assumed. Further, the experimental measurement locations were measured from the bottom of the cylinder, which may have undergone some material loss when cut from the baseplate. The finite element model assumes nominal dimensions of the cylinder. Therefore, some error in the height measurements could exist.

Figure 57 through Figure 60 show comparisons between the experimental and finite element model residual axial and hoop stress for all four etching measurements along the four sides. Included in the figures are the finite element model results at the outside surface and at a depth of 0.67 mm from the surface. The finite element model results are the same in all three figures. The finite element model results are similar at all four measurement sides for both the outside and 0.67mm depth locations, suggesting a uniform stress state around the circumference of the part (see also Figure 49a for a contour of hoop stress on the cylinder). The 0.67 mm depth location is less tensile compared to the outside surface along most of the height of the cylinder. The experimental results show significant variation between the four measurements sides as well as between etching measurements.

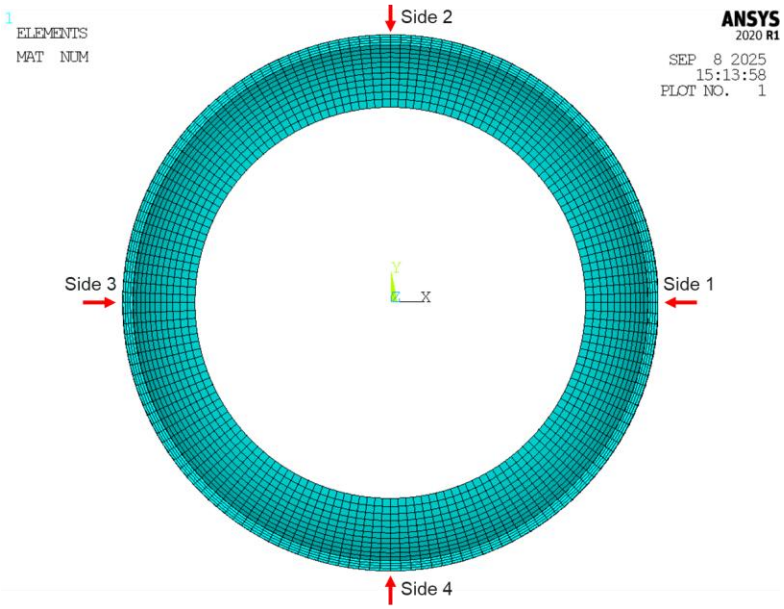

Figure 56. Top view schematic of residual stress measurement locations

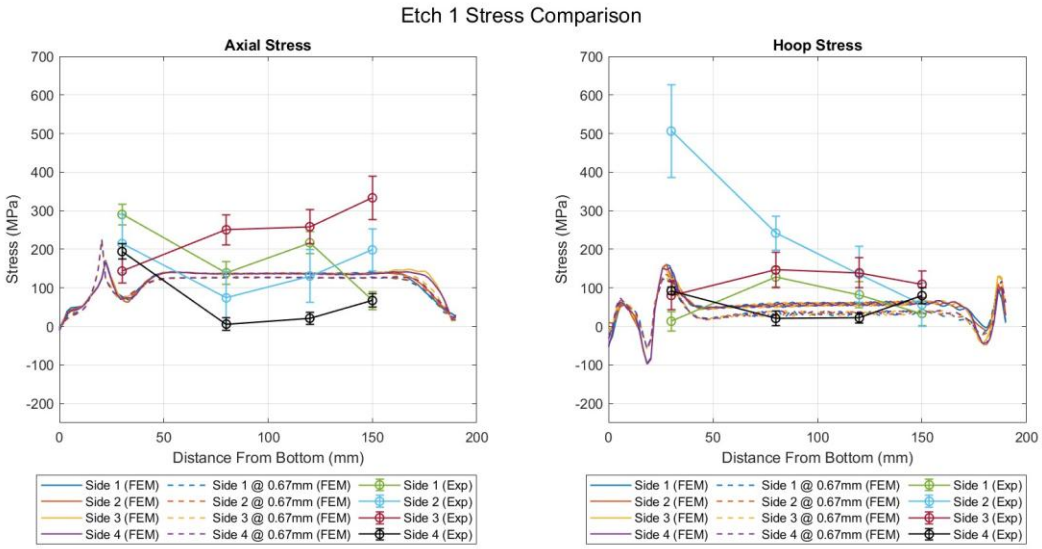

Figure 57. Etch 1 Stress Comparison: Axial Stress (Left) and Hoop Stress (Right)

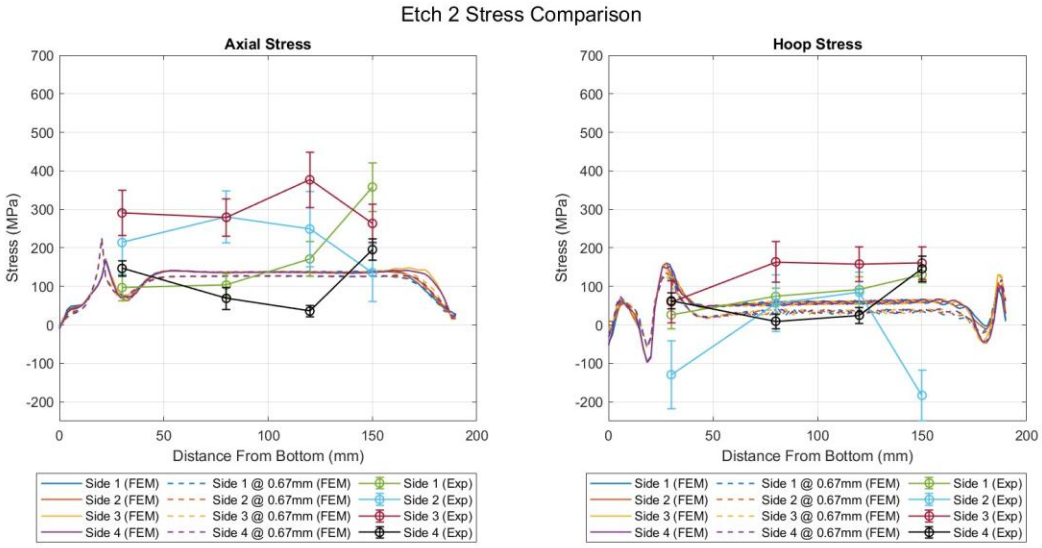

Figure 58. Etch 2 Stress Comparison: Axial Stress (Left) and Hoop Stress (Right)

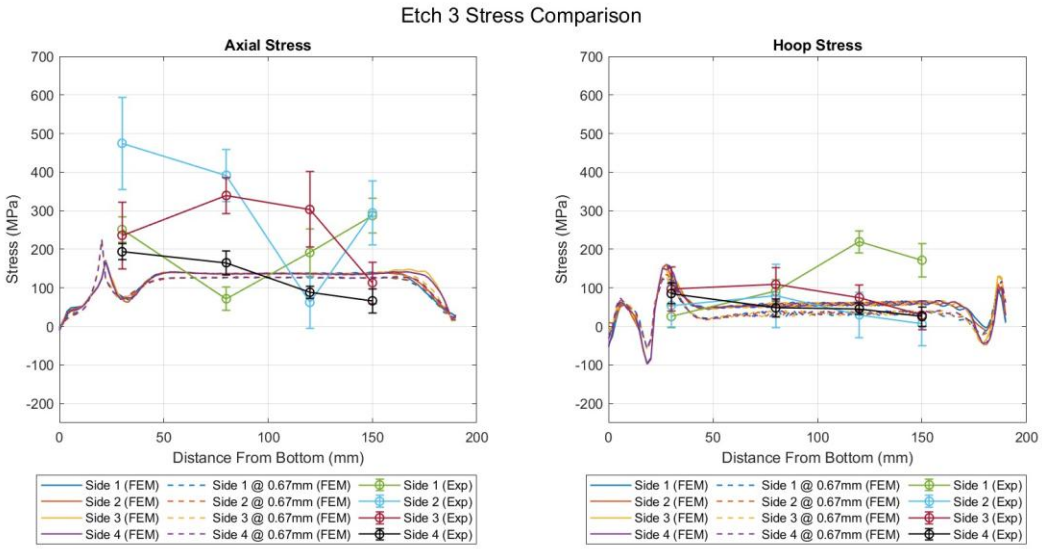

Figure 59. Etch 3 Stress Comparison: Axial Stress (Left) and Hoop Stress (Right)

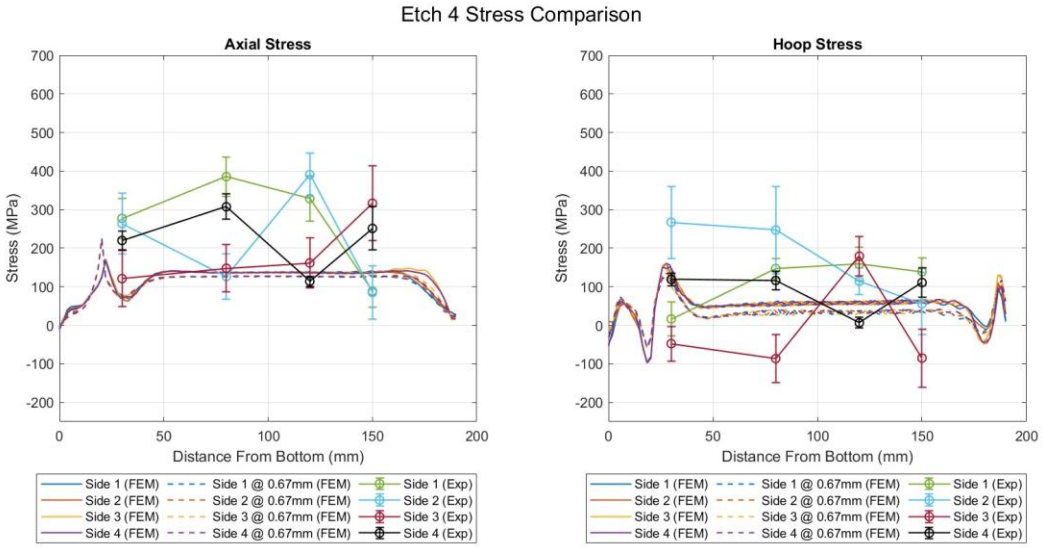

Figure 60. Etch 4 Stress Comparison: Axial Stress (Left) and Hoop Stress (Right)

The absolute difference between the experimental data and the side-averaged stress of all four sides of the finite element results were calculated to quantify a metric of difference between the data. The side-averaged mean was calculated at the outside surface and the 0.67mm depth location for both axial and hoop stress finite element results. The experimental height locations were interpolated in the side-averaged finite element data. Taking the side-averaged stress of all four sides was justified by the fact that the finite element stress variation between sides was small compared to the variation in the experimental data. Further, a one-to-one comparison is not possible due to uncertainty of the location of the experimental measurement “side” location with respect to the start of the build. Figure 61 through Figure 64 illustrate the axial and hoop stress difference between all four sides of the experimental data and the mean finite element stress data. The stress differences between the outside surface and 0.67mm depth location are

similar due to the small change in the finite element data at these locations. Tabulated data of the side averaged finite element results and experimental stress differences are displayed in Table 22 and Table 23 for axial and hoop stress, respectively. Notable global similarities between the finite element results and the experimental data include:

- A stress difference within ±50MPa for the side 1, etch 2, axial stress experimental data for the first three height measurements.
- A stress difference within ±72MPa for the side 4, etch 3, axial stress experimental data for the last three height measurements.
- A stress difference within ±50MPa for the side 3, etch 4, axial stress experimental data for the first three height measurements.
- A stress difference within ±50MPa for the side 4, etch 1, hoop stress experimental data at all height locations.
- A stress difference within ±74MPa for the side 4, etch 2, hoop stress experimental data for the first three height measurements.
- A stress difference within ±82MPa for the side 2, side 3, and side 4, etch 3, hoop stress experimental data at all height locations.
- A stress difference within ±84MPa for the side 4, etch 4, hoop stress experimental data at all height locations.

Evaluation of the stress difference at both the finite element side averaged outside surface and 0.67mm depth location yields a total of 128 stress difference data points. A total of 31 out of 128 (24.2%) axial stress difference data points were within ±50MPa of the side-averaged finite element axial stress data. A total of 51 out of 128 (39.8%) hoop stress difference data points were within ±50MPa of the side-averaged finite element hoop stress data. While some relative similarity is observed in the data sets listed above, there still exists large variations in the remaining experimental data. Further insights into the stress profile of the experimentally fabricated cylinder could be obtained from deeper etching measurements, as well as more measurement locations along the height and circumference of the part. This additional data would aid in validating the finite element model results and inform the modeling methodology.

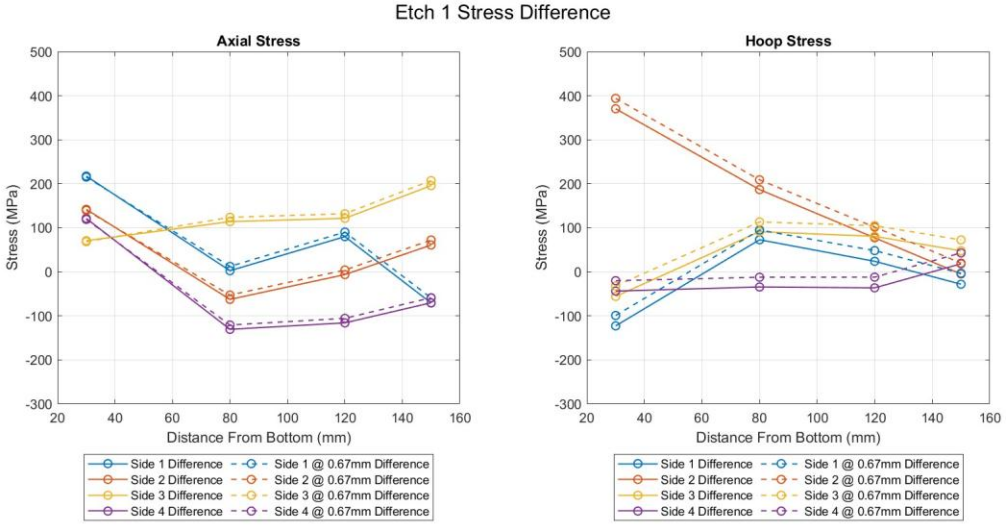

Figure 61. Etch 1 Stress Difference: Axial Stress (Left) and Hoop Stress (Right)

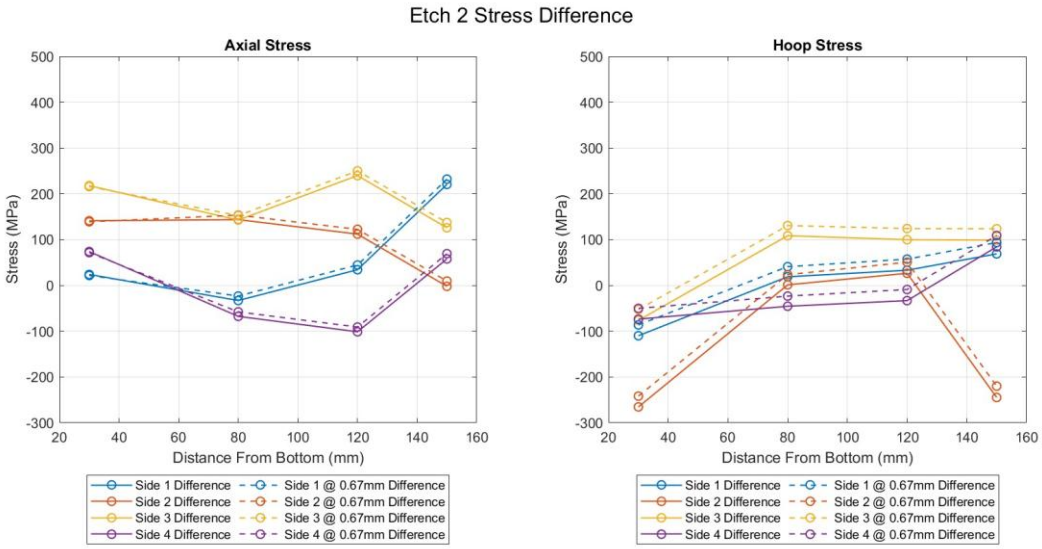

Figure 62. Etch 2 Stress Difference: Axial Stress (Left) and Hoop Stress (Right)

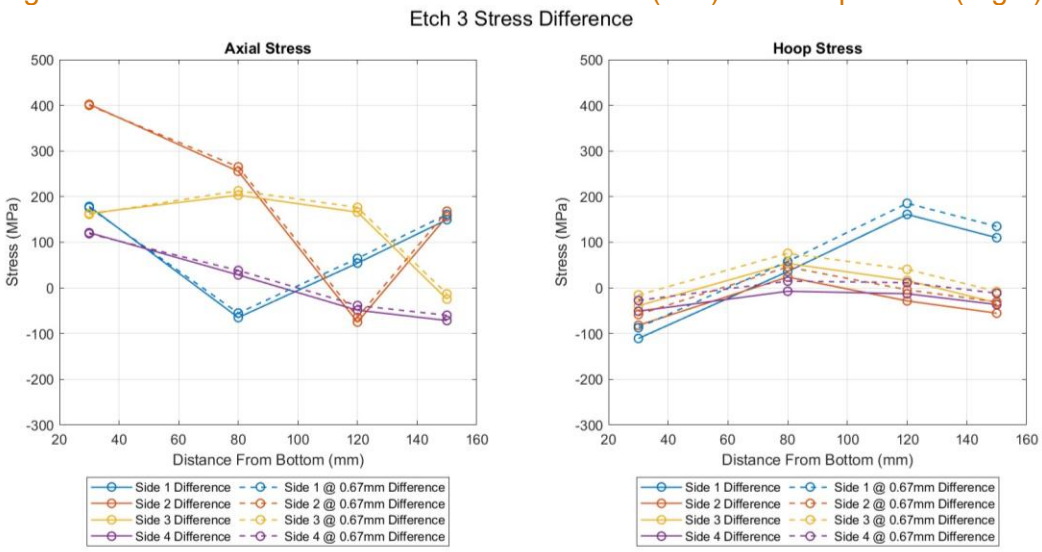

Figure 63. Etch 3 Stress Difference: Axial Stress (left) and Hoop Stress (right)

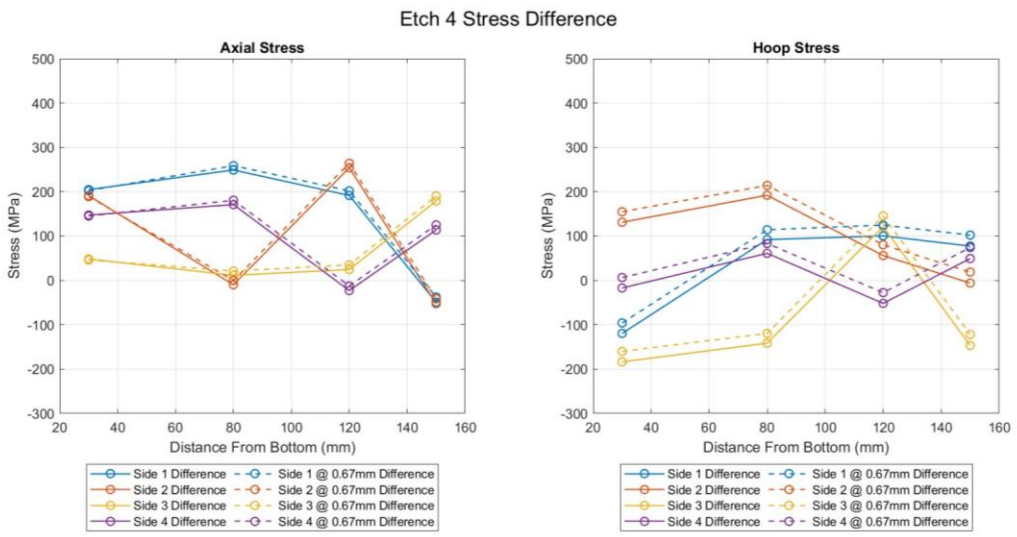

Figure 64. Etch 4 stress difference: axial stress (left) and hoop stress (right)

Table 22. Axial stress difference summary

Distance From Bottom (mm)	Finite Element Side Averaged Axial Stress (MPa)		Side 1 Experimental Difference (MPa)		Side 2 Experimental Difference (MPa)		Side 3 Experimental Difference (MPa)		Side 4 Experimental Difference (MPa)	
Etch 1	**Outside Surface**	**0.6mm Depth**	**Outside Surface**	**0.6mm Depth**	**Outside Surface**	**0.6mm Depth**	**Outside Surface**	**0.6mm Depth**	**Outside Surface**	**0.6mm Depth**
30	72.62	74.86	217.51	215.27	142.03	139.79	70.80	68.56	121.42	119.18
80	136.36	126.59	2.58	12.35	-62.53	-52.76	114.14	123.91	-130.50	-120.73
120	136.90	126.54	80.01	90.37	-6.21	4.15	121.58	131.94	-115.87	-105.51
150	137.53	126.08	-70.71	-59.26	60.91	72.36	195.84	207.29	-70.22	-58.77
Etch 2	**Outside Surface**	**0.6mm Depth**	**Outside Surface**	**0.6mm Depth**	**Outside Surface**	**0.6mm Depth**	**Outside Surface**	**0.6mm Depth**	**Outside Surface**	**0.6mm Depth**
30	72.62	74.86	23.90	21.66	141.15	138.91	217.91	215.67	73.89	71.65
80	136.36	126.59	-32.99	-23.22	143.63	153.40	142.69	152.46	-67.60	-57.83
120	136.90	126.54	34.24	44.60	111.99	122.35	239.73	250.09	-101.28	-90.92
150	137.53	126.08	220.58	232.03	-2.03	9.42	125.82	137.27	57.82	69.27
Etch 3	**Outside Surface**	**0.6mm Depth**	**Outside Surface**	**0.6mm Depth**	**Outside Surface**	**0.6mm Depth**	**Outside Surface**	**0.6mm Depth**	**Outside Surface**	**0.6mm Depth**
30	72.62	74.86	178.55	176.31	402.14	399.90	163.39	161.15	121.14	118.90
80	136.36	126.59	-64.66	-54.89	255.42	265.19	203.11	212.88	28.64	38.41
120	136.90	126.54	54.48	64.84	-74.65	-64.29	166.10	176.46	-48.66	-38.30
150	137.53	126.08	149.67	161.12	156.70	168.15	-24.41	-12.96	-71.15	-59.70
Etch 4	**Outside Surface**	**0.6mm Depth**	**Outside Surface**	**0.6mm Depth**	**Outside Surface**	**0.6mm Depth**	**Outside Surface**	**0.6mm Depth**	**Outside Surface**	**0.6mm Depth**
30	72.62	74.86	204.63	202.39	191.11	188.87	48.33	46.09	147.32	145.08
80	136.36	126.59	248.95	258.72	-9.85	-0.08	11.46	21.23	170.93	180.70
120	136.90	126.54	191.57	201.93	253.82	264.18	24.61	34.97	-22.85	-12.49
150	137.53	126.08	-49.01	-37.56	-52.59	-41.14	178.96	190.41	113.70	125.15

Table 23. Hoop stress difference summary

Distance From Bottom (mm)	Finite Element Side Averaged Hoop Stress (MPa)		Side 1 Experimental Difference (MPa)		Side 2 Experimental Difference (MPa)		Side 3 Experimental Difference (MPa)		Side 4 Experimental Difference (MPa)	
Etch 1	**Outside Surface**	**0.6mm Depth**	**Outside Surface**	**0.6mm Depth**	**Outside Surface**	**0.6mm Depth**	**Outside Surface**	**0.6mm Depth**	**Outside Surface**	**0.6mm Depth**
30	135.90	112.32	-122.69	-99.11	370.38	393.96	-55.76	-32.18	-43.64	-20.06
80	55.00	32.86	72.91	95.05	186.89	209.03	91.28	113.42	-34.31	-12.17
120	58.14	33.87	24.03	48.30	77.37	101.64	80.68	104.95	-36.30	-12.03
150	61.50	36.73	-28.03	-3.26	-4.84	19.93	47.80	72.57	18.34	43.11
Etch 2	**Outside Surface**	**0.6mm Depth**	**Outside Surface**	**0.6mm Depth**	**Outside Surface**	**0.6mm Depth**	**Outside Surface**	**0.6mm Depth**	**Outside Surface**	**0.6mm Depth**
30	135.90	112.32	-109.90	-86.32	-265.31	-241.73	-76.30	-52.72	-73.67	-50.09
80	55.00	32.86	18.82	40.96	1.23	23.37	108.53	130.67	-45.51	-23.37
120	58.14	33.87	33.13	57.40	26.45	50.72	99.83	124.10	-33.25	-8.98
150	61.50	36.73	68.87	93.64	-244.70	-219.93	98.89	123.66	84.18	108.95
Etch 3	**Outside Surface**	**0.6mm Depth**	**Outside Surface**	**0.6mm Depth**	**Outside Surface**	**0.6mm Depth**	**Outside Surface**	**0.6mm Depth**	**Outside Surface**	**0.6mm Depth**
30	135.90	112.32	-110.47	-86.89	-81.62	-58.04	-38.85	-15.27	-50.78	-27.20
80	55.00	32.86	36.03	58.17	24.06	46.20	53.87	76.01	-7.10	15.04
120	58.14	33.87	161.14	185.41	-28.23	-3.96	16.52	40.79	-12.52	11.75
150	61.50	36.73	110.08	134.85	-55.10	-30.33	-32.39	-7.62	-36.18	-11.41
Etch 4	**Outside Surface**	**0.6mm Depth**	**Outside Surface**	**0.6mm Depth**	**Outside Surface**	**0.6mm Depth**	**Outside Surface**	**0.6mm Depth**	**Outside Surface**	**0.6mm Depth**
30	135.90	112.32	-119.50	-95.92	131.17	154.75	-183.60	-160.02	-17.09	6.49
80	55.00	32.86	92.07	114.21	192.02	214.16	-141.53	-119.39	61.11	83.25
120	58.14	33.87	100.44	124.71	56.00	80.27	121.08	145.35	-51.81	-27.54
150	61.50	36.73	77.44	102.21	-6.01	18.76	-146.62	-121.85	49.29	74.06

6 Joint Summary Report for the Generation IV International Forum Policy Group on the Benchmark Experimental Work

In addition to the benefits for the AMMT program, this work also includes global collaboration in coordinating and sharing data through the Generation IV International Forum (GIF) Advanced Manufacturing Materials Engineering Working Group (AMME-WG). As mentioned in the FY24 milestone report (van Rooyen et al., 2024), this work can be used to demonstrate the benefits of advanced manufacturing (AM) processes and gain knowledge, without sharing competitive information and therefore demonstrate integrated material and advanced AM development for accelerated deployment.

In collaboration with the other GIF member country members of the GIF-AMME-WG, experimental data of different variations of 316 SS are shared by the GIF-AMME WG members, and this will provide a new database and comparative dataset for the international industry and will benefit the larger nuclear stakeholders by understanding the variations and the possible impact it may have on the different reactor type applications. The alloy variants that are currently pursued by the international team through the GIF-AMME WG's benchmark study are 316L, 316H, 316H (low N), and 316L (low N). The benchmark study consists of two main tasks: 1) a modeling and simulation task and 2) the experimental manufacturing and associated characterization part. The same product forms as shown earlier in Figure 3 are used in the benchmark study activities.

The bulk of the experimental work this past year consisted of the PNNL-AMMT work as described in this report, as well as the data collection started from France and Switzerland on small block characterization results of 316L SS LP-DED and commitment received from Canada for the printing of the expanded elbow in the following year. Additionally, also contributing towards the AMME WG's objectives, an iNERI project titled "Assessment of the Small Punch Test for High Temperature Qualification of Additive Manufactured Components" was established between U.S. Investigating Organization and Principal Investigators (Pacific Northwest National Laboratory PNNL) Isabella Van Rooyen/Argonne National Laboratory (ANL) Mark Messner) and Euratom (JRC/Igor Simonovski). The main objective of the project is to explore to what extent and how the small punch test can be used to support the qualification of AM components operating at high temperatures. In the project small punch tensile and creep tests will be conducted on specimens extracted from bars and, if available, from components or witness specimens. The primary candidate material is 316H SS produced from LPBF. The work may provide further knowledge on how these small tests can be used for acceleration for not only qualification, but also research and development activities. This work can be expanded to include 316H SS LP-DED samples as well. No formal joint AMME WG report has been produced this FY year yet on various 316 SS components characterization results.

The initial work by the PNNL-AMMT team on modeling the 316L SS cylinder was used for collaborative work with members from Canada, France, Europe Union, ANL, and PNNL. This work resulted in a joint presentation and conference proceedings paper (Lucian Ivan 2025) at the National Energy Agency sponsored "Regulatory Frameworks and Technical Approaches for Qualification and Through-Life Performance of Materials in Advanced Reactors" held at the Nuclear Regulatory Commission in June 2025. The Modeling and simulation task team also prepared a database of available software packages and methods for advanced manufacturing components and is available now for only the AMME-WG members. It is envisaged with more validation, this database may be made available for the GIF-community as an open database,

however it is not yet planned for the next few years. The above-mentioned paper also addresses the approach and some of the results in achieving this. Below is the abstract of the paper:

> *"Qualifying new advanced manufacturing technologies (AMTs) for use with nuclear design codes can be a lengthy and complex process, which can hinder broader adoption. However, advancements in modelling and simulation (M&S) methodologies offer industrial users of AMTs the ability to generate critical data that could accelerate the process, potentially making M&S an essential and integral part of the qualification process. To enable the wider adoption of M&S approaches for qualification, an industry-focused database has been developed by an international working group to identify well-suited computational methods and software tools for predicting thermomechanical history and residual mechanical properties of components made by advanced manufacturing according to several features, such as manufacturing processes, prediction property, and code availability. However, to support the qualification process, it is necessary to demonstrate the benefits of such M&S tools using benchmark problems and to clearly establish their modelling requirements. This work reports initial findings related to the assessment of a benchmark case for model evaluation involving an experimentally fabricated part. The as-built properties of a geometry-agnostic 316 stainless steel component are predicted using two physics-based approaches for the direct-energy-deposition fabrication process. The overarching goal of this work is to establish a comprehensive database of simulation tools that, when combined with validated benchmark studies, will enable the selection of appropriate M&S approaches for nuclear qualification and provide a set of good practices for their utilization."*

The GIF AMME-WG full collection of work will be evaluated during the in-person meeting planned in collaboration with the International Energy Agency during June 2026. During this invited technical consultancy meeting, decisions will be made on the readiness and maturity of data received from collaborators and the envisaged deliverables.

7 Summary and Future Work

The project aims to use DED to manufacture complex microreactor components that are traditionally costly and difficult to produce through conventional methods. The selected component is an expanded elbow pipe that provides a smooth transition from larger to smaller pipe at a 90° bend, reducing space requirements and improving fluid flow. Thirteen different microreactor designs were identified as potential candidates for this expanded elbow component. Because of equipment limitations, the full-size design specifications (12-inch to 6-inch inner diameter) were scaled down to 40% (4.8-inch to 2.4-inch inner diameter) while maintaining geometric proportions and demonstrating proof of concept for realistic piping applications.

- For process parameter optimization, 16 cube samples were fabricated using varied process parameters including laser powers from 400-700W and scan speeds from 600-900 mm/min. The results achieved relative densities between 99.16-99.97%, with laser powers of 500W and 700W consistently yielding densities above 99.8%. The key finding revealed that laser power has a significantly greater impact on material density compared to scan speed, with recommended parameter ranges of 500-550W with 600-700 mm/min or 650-700W with 650-900 mm/min for optimal density results.
- Non-destructive evaluation using Archimedes method achieved density measurements with less than 0.2% standard deviation, while ultrasonic testing calculated elastic properties including Young's modulus ranging from 153–208 GPa and bulk modulus from 124-172 GPa. Grain sizes ranged from 208-523 μm with larger grains correlating to higher laser power, and a distinctive "honeycomb" cellular structure was observed with cell sizes between 3.23–6.17 μm that increased with higher laser power settings.
- XRD measurements identified both compressive stress (up to -47.6 MPa) and tensile stress (up to +19.2 MPa) in the fabricated samples. Large cylinder analysis measured through-thickness stress profiles up to 600 μm depth using electro-etching techniques, revealing that hoop stress was generally lower than axial stress with stress patterns varying by location. Vickers hardness testing showed increased hardness with scan speed (except at 500 W), with optimal performance in the 500—600 W laser power range, although no direct correlation was found between hardness and Young's modulus measurements.
- X-ray computer tomography analysis of small tubes achieved greater than 99% density with 9.5 μm voxel resolution, confirming that higher volumetric energy density correlated with decreased porosity. Wire DED demonstration successfully printed a 316L SS cylinder using 800 W laser power and 16.8 mm/s wire feed rate, although high thermal gradients and build plate warpage were observed, indicating areas for process improvement in future applications.
- Flow-3D simulations were developed to predict porosity before experimental fabrication, with simulated porosity values (0.035–0.048%) generally lower than experimental measurements (0.030–0.840%). A corrector model using machine learning techniques was developed to bridge the simulation-experiment gap, achieving prediction errors below 1%. However, the model's generalizability is limited by the small dataset of 16 points, indicating the need for expanded experimental validation across broader parameter ranges and material variations.
- Support structure optimization addressed the challenge where support volume (569,592 mm^3) exceeded the actual part volume (547,790 mm^3) for the elbow component. Through parameter refinement focusing on support diameter, spacing, and density, build time was reduced from 349 hours to 142 hours while maintaining structural integrity. The

build configuration was strategically oriented for re-coater stability and gas flow clearance, with process parameters found in the literature showing optimal volumetric energy density ranges of 52–95 J/mm³ across different LPBF systems.

The comprehensive study demonstrates that both LP-DED and LPBF manufacturing processes are viable for producing complex microreactor components with properties comparable or superior to wrought materials. Process optimization guidelines have been established with specific parameter recommendations, and computational tools have been validated for predictive manufacturing. The successful demonstration of the expanded elbow pipe concept, even at reduced scale, provides a foundation for full-scale implementation in actual microreactor applications, supporting the broader goal of enabling advanced nuclear energy systems through AM technologies.

Residual stress characterization of the LP- DED fabricated 316H SS shows significant axial and hoop stress variation between the measurement locations and etching depth. The side-averaged finite element axial and hoop stress data at the outside surface and at a 0.67 mm depth from the DED structural simulation were compared to the experimental data. The side-averaged data included four, 90°-spaced sides, and was evaluated at the height locations used in the experimental data. The use of side-averaged data was justified by the relatively uniform stress profile predicted by the model around the circumference of the cylinder. The comparison between the structural finite element results and the experimental data shows some notable global similarities:

- A stress difference within ±50MPa for the side 1, etch 2, axial stress experimental data for the first three height measurements
- A stress difference within ±72MPa for the side 4, etch 3, axial stress experimental data for the last three height measurements
- A stress difference within ±50MPa for the side 3, etch 4, axial stress experimental data for the first three height measurements
- A stress difference within ±50MPa for the side 4, etch 1, hoop stress experimental data at all height locations
- A stress difference within ±74MPa for the side 4, etch 2, hoop stress experimental data for the first three height measurements
- A stress difference within ±82MPa for the side 2, side 3, and side 4, etch 3, hoop stress experimental data at all height locations
- A stress difference within ±84MPa for the side 4, etch 4, hoop stress experimental data at all height locations.

Evaluation of the stress difference at both the finite element side-averaged outside surface and 0.67mm depth location yields a total of 128 stress difference data points. A total of 31 out of 128 (24.2%) axial stress difference data points were within ±50MPa of the side-averaged finite element axial stress data. A total of 51 out of 128 (39.8%) hoop stress difference data points were within ±50MPa of the side-averaged finite element hoop stress data. While some relative similarity is observed in the data sets listed above, there still exists large variations in the remaining experimental data. Further insights into the stress profile of the experimentally fabricated cylinder could be obtained from deeper etching measurements, as well as more measurement locations along the height and circumference of the part. This additional data would aid in validating the finite element model results and informing the modeling methodology.

8 Publications and Presentations

8.1 Presentations

1. Isabella van Rooyen, James Fitzpatrick, Nathan Barrett, CJ Taylor Mason, Subhashish Meher, Daniel Yoon, Robert Montgomery, Chris Hutchinson, Mohan Nartu, Pratikshya Meher, Ankit Roy, “Benchmark Geometric Study on 316H and 316L Components Manufactured by Powder DED,” GIF AMME-WG in-person meeting, Baden Switzerland, April 8 -11, 2025, PNNL-SA-210216.
2. Robert Montgomery, Isabella van Rooyen, Chris Hutchinson, Richard Jacob, Nicholas Conway, “Life Cycle NDE for Advance Manufactured Components,” GIF AMME-WG in-person meeting, Baden Switzerland, April 8 -11, 2025, PNNL-SA-209797.

8.2 Publications

1. Lucian Ivan, Mark Messner, Daniel Yoon, James Fitzpatrick, Taylor Mason, Karl-Fredrik Nilsson, Celine Cabet, Isabella J. van Rooyen, "A case study assessment of qualification acceleration informed by physics-based modelling," Regulatory Frameworks and Technical Approaches for Qualification and Through-Life Performance of Materials in Advanced Reactors, Conference Paper, June 2025. (In-Review)
2. Daniel Yoon, Subhashish Meher, Nicholas Conway, Chris Hutchinson, Robert Montgomery, John Snitzer, Xiaoyuan Lou, Isabella van Rooyen, “Microstructural and Mechanical Property Evaluation of DED-Manufactured 316H Stainless Steel Geometries for Nuclear Applications.” (In draft)

9 References

Ablyaz, T. R., I. V. Osinnikov, A. A. Shiryaev, K. R. Muratov, and E. V. Smolentsev. 2022. "Residual Stress after Electric Discharge Machining." *Russian Engineering Research* 42 (8): 850-852. https://doi.org/10.3103/s1068798x22080044.

Alamri, F., I. Barsoum, S. Bojanampati, and M. Maalouf. 2025. "Prediction of Porosity, Hardness and Surface Roughness in Additive Manufactured Alsi10mg Samples." *PLoS One* 20 (3): e0316600. https://doi.org/10.1371/journal.pone.0316600. PMCID: PMC11892887.

AlFaify, A., J. Hughes, and K. Ridgway. 2018. "Controlling the Porosity of 316l Stainless Steel Parts Manufactured Via the Powder Bed Fusion Process." *Rapid Prototyping Journal* 25 (1): 162-175. https://doi.org/10.1108/rpj-11-2017-0226.

Alsalla, H. H., C. Smith, and L. Hao. 2018. "Effect of Build Orientation on the Surface Quality, Microstructure and Mechanical Properties of Selective Laser Melting 316l Stainless Steel." *Rapid Prototyping Journal* 24 (1): 9-17. https://doi.org/10.1108/rpj-04-2016-0068.

Amar, E., V. Popov, V. M. Sharma, S. Andreev Batat, D. Halperin, and N. Eliaz. 2023. "Response Surface Methodology (Rsm) Approach for Optimizing the Processing Parameters of 316l Ss in Directed Energy Deposition." *Materials (Basel)* 16 (23). https://doi.org/10.3390/ma16237253. PMCID: PMC10707294.

An, D., Y. Xiao, X. Liu, H. Zhao, X. Li, and J. Chen. 2023. "Formation of Two Distinct Cellular Structures in 316l Stainless Steel Fabricated by Micro-Laser Beam Powder-Bed-Fusion." *Materials Research Letters* 12 (1): 42-49. https://doi.org/10.1080/21663831.2023.2292076.

Aversa, A., G. Marchese, and E. Bassini. 2021. "Directed Energy Deposition of Aisi 316l Stainless Steel Powder: Effect of Process Parameters." *Metals* 11 (6). https://doi.org/10.3390/met11060932.

Bartlett, J. L., and X. Li. 2019. "An Overview of Residual Stresses in Metal Powder Bed Fusion." *Additive Manufacturing* 27: 131-149. https://doi.org/10.1016/j.addma.2019.02.020.

Caminero, M. Á., A. Romero Gutiérrez, J. M. Chacón, E. García-Plaza, and P. J. Núñez. 2022. "Effects of Fused Filament Fabrication Parameters on the Manufacturing of 316l Stainless-Steel Components: Geometric and Mechanical Properties." *Rapid Prototyping Journal* 28 (10): 2004-2026. https://doi.org/10.1108/rpj-01-2022-0023.

Carlton, H. D., A. Haboub, G. F. Gallegos, D. Y. Parkinson, and A. A. MacDowell. 2016. "Damage Evolution and Failure Mechanisms in Additively Manufactured Stainless Steel." *Materials Science and Engineering: A* 651: 406-414. https://doi.org/10.1016/j.msea.2015.10.073.

Chen, S.-g., H.-j. Gao, Y.-d. Zhang, Q. Wu, Z.-h. Gao, and X. Zhou. 2022. "Review on Residual Stresses in Metal Additive Manufacturing: Formation Mechanisms, Parameter Dependencies, Prediction and Control Approaches." *Journal of Materials Research and Technology* 17: 2950-2974. https://doi.org/10.1016/j.jmrt.2022.02.054.

Choo, H., L. P. White, X. Xiao, C. C. Sluss, D. Morin, and E. Garlea. 2021. "Deformation and Fracture Behavior of a Laser Powder Bed Fusion Processed Stainless Steel: In Situ

Synchrotron X-Ray Computed Microtomography Study." *Additive Manufacturing* 40. https://doi.org/10.1016/j.addma.2021.101914.

DelRio, F. W., R. M. Khan, M. J. Heiden, P. G. Kotula, P. A. Renner, E. K. Karasz, and M. A. Melia. 2023. "Porosity, Roughness, and Passive Film Morphology Influence the Corrosion Behavior of 316l Stainless Steel Manufactured by Laser Powder Bed Fusion." *Journal of Manufacturing Processes* 102: 654-662. https://doi.org/10.1016/j.jmapro.2023.07.062.

Era, I. Z., M. Grandhi, and Z. Liu. 2022. "Prediction of Mechanical Behaviors of L-Ded Fabricated Ss 316l Parts Via Machine Learning." *Int J Adv Manuf Technol* 121 (3-4): 2445-2459. https://doi.org/10.1007/s00170-022-09509-1. PMCID: PMC9188360.

Garlea, E., H. Choo, C. C. Sluss, M. R. Koehler, R. L. Bridges, X. Xiao, Y. Ren, and B. H. Jared. 2019. "Variation of Elastic Mechanical Properties with Texture, Porosity, and Defect Characteristics in Laser Powder Bed Fusion 316l Stainless Steel." *Materials Science and Engineering: A* 763. https://doi.org/10.1016/j.msea.2019.138032.

Huang, Y.-C., S.-Y. Chang, and C.-H. Chang. 2009. "Effect of Residual Stresses on Mechanical Properties and Interface Adhesion Strength of Sin Thin Films." *Thin Solid Films* 517 (17): 4857-4861. https://doi.org/10.1016/j.tsf.2009.03.043.

International, A. 2021. *Standard Test Method for Residual Stress Measurement by X-Ray Diffraction for Bearing Steels*. West Conshohocken, PA: ASTM International.

Jardon, Z., J. Ertveldt, M. Hinderdael, and P. Guillaume. 2021. "Process Parameter Study for Enhancement of Directed Energy Deposition Powder Efficiency Based on Single-Track Geometry Evaluation." *Journal of Laser Applications* 33 (4). https://doi.org/10.2351/7.0000516.

Kan, W. H., L. N. S. Chiu, C. V. S. Lim, Y. Zhu, Y. Tian, D. Jiang, and A. Huang. 2022. "A Critical Review on the Effects of Process-Induced Porosity on the Mechanical Properties of Alloys Fabricated by Laser Powder Bed Fusion." *Journal of Materials Science* 57 (21): 9818-9865. https://doi.org/10.1007/s10853-022-06990-7.

Kartikeya Sarma, I., V. Srinivas, and S. Kanmani Subbu. 2021. "Effect of Process Parameters on Micro Hardness, Bulk Hardness and Porosity of Lenstm Deposited Ss 316l Alloy." *Materials Today: Proceedings* 46: 2616-2624. https://doi.org/10.1016/j.matpr.2021.02.268.

Leicht, A., M. Rashidi, U. Klement, and E. Hryha. 2020. "Effect of Process Parameters on the Microstructure, Tensile Strength and Productivity of 316l Parts Produced by Laser Powder Bed Fusion." *Materials Characterization* 159. https://doi.org/10.1016/j.matchar.2019.110016.

Lim, J. S., W. J. Oh, C. M. Lee, and D. H. Kim. 2021. "Selection of Effective Manufacturing Conditions for Directed Energy Deposition Process Using Machine Learning Methods." *Sci Rep* 11 (1): 24169. https://doi.org/10.1038/s41598-021-03622-z. PMCID: PMC8683500.

Liu, Q., J. Lu, Z. Luo, J. Yi, M. He, Y. Zhao, and S. Wang. 2023. "Enhancing Corrosion Resistance of Additively Manufactured 316l Stainless Steel by Fabricating Pillar Arrays." *Materials & Design* 230. https://doi.org/10.1016/j.matdes.2023.111940.

Lu, X., M. Chiumenti, M. Cervera, J. Li, X. Lin, L. Ma, G. Zhang, and E. Liang. 2021. “Substrate Design to Minimize Residual Stresses in Directed Energy Deposition Am Processes.” *Materials & Design* 202. https://doi.org/10.1016/j.matdes.2021.109525.

Majumdar, J. D., A. Pinkerton, Z. Liu, I. Manna, and L. Li. 2005. “Microstructure Characterisation and Process Optimization of Laser Assisted Rapid Fabrication of 316l Stainless Steel.” *Applied Surface Science* 247 (1-4): 320-327. https://doi.org/10.1016/j.apsusc.2005.01.039.

Mercelis, P., and J. P. Kruth. 2006. “Residual Stresses in Selective Laser Sintering and Selective Laser Melting.” *Rapid Prototyping Journal* 12 (5): 254-265. https://doi.org/10.1108/13552540610707013.

Moon, J. H., S. M. Baek, S. G. Lee, Y. Seong, A. Amanov, S. Lee, and H. S. Kim. 2018. “Effects of Residual Stress on the Mechanical Properties of Copper Processed Using Ultrasonic-Nanocrystalline Surface Modification.” *Materials Research Letters* 7 (3): 97-102. https://doi.org/10.1080/21663831.2018.1560370.

Piscopo, G., A. Salmi, and E. Atzeni. 2021. “Influence of High-Productivity Process Parameters on the Surface Quality and Residual Stress State of Aisi 316l Components Produced by Directed Energy Deposition.” *Journal of Materials Engineering and Performance* 30 (9): 6691-6702. https://doi.org/10.1007/s11665-021-05954-3.

Romano, S., A. Brückner-Foit, A. Brandão, J. Gumpinger, T. Ghidini, and S. Beretta. 2018. “Fatigue Properties of Alsi10mg Obtained by Additive Manufacturing: Defect-Based Modelling and Prediction of Fatigue Strength.” *Engineering Fracture Mechanics* 187: 165-189. https://doi.org/10.1016/j.engfracmech.2017.11.002.

Ronneberg, T., C. M. Davies, and P. A. Hooper. 2020. “Revealing Relationships between Porosity, Microstructure and Mechanical Properties of Laser Powder Bed Fusion 316l Stainless Steel through Heat Treatment.” *Materials & Design* 189. https://doi.org/10.1016/j.matdes.2020.108481.

Röttger, A., K. Geenen, M. Windmann, F. Binner, and W. Theisen. 2016. “Comparison of Microstructure and Mechanical Properties of 316 L Austenitic Steel Processed by Selective Laser Melting with Hot-Isostatic Pressed and Cast Material.” *Materials Science and Engineering: A* 678: 365-376. https://doi.org/10.1016/j.msea.2016.10.012.

Salmi, A., G. Piscopo, A. N. Pilagatti, and E. Atzeni. 2024. “Evaluation of Porosity in Aisi 316l Samples Processed by Laser Powder Directed Energy Deposition.” *Journal of Manufacturing and Materials Processing* 8 (4). https://doi.org/10.3390/jmmp8040129.

Schroeder, S. C., J. Frankel, and A. Abbate. 1995. *The Relationship between Residual Stress and Hardness and the Onset of Plastic Deformation.* US Army Armamend Research, Development and Engineering Center Watervliet, VY.

Sharma, V. M., V. Popov, A. R. Farkoosh, D. Isheim, D. N. Seidman, and N. Eliaz. 2024. “Process Parameter Optimization of Directed Energy Deposited Qt17-4+ Steel.” *Advanced Materials Technologies* 9 (15). https://doi.org/10.1002/admt.202400024.

Sun, C., P. He, Z. Hu, and X. Liang. 2024. “Metallurgical Characteristics of 316l Stainless Steel by Laser Additive Manufacturing.” *Intelligent and Sustainable Manufacturing* 1 (2): 10012-10012. https://doi.org/10.35534/ism.2024.10012.

Suryawanshi, J., K. G. Prashanth, and U. Ramamurty. 2017. “Mechanical Behavior of Selective Laser Melted 316l Stainless Steel.” *Materials Science and Engineering: A* 696: 113-121. https://doi.org/10.1016/j.msea.2017.04.058.

Tan, Z. E. E., J. H. L. Pang, J. Kaminski, and H. Pepin. 2019. “Characterisation of Porosity, Density, and Microstructure of Directed Energy Deposited Stainless Steel Aisi 316l.” *Additive Manufacturing* 25: 286-296. https://doi.org/10.1016/j.addma.2018.11.014.

van Rooyen, I. J., J. F. Fitzpatrick, N. P. Barrett, C. Mason, S. Meher, D. Yoon, R. O. Montgomery, C. A. Hutchinson, and M. S. K. K. Y. Nartu. 2024. *Benchmark Study Matrix for Microreactor Geometries Relevant to Multiple Developers.* Pacific Northwest National Laboratory (PNNL), Richland, WA (United States) United States. https://www.osti.gov/biblio/2481593

Wang, X. 2024. “Cell Structure in Steels Induced by Additive Manufacturing.” *Materials Science and Technology* 41 (1): 3-16. https://doi.org/10.1177/02670836241255257.

Wei, H. L., T. Mukherjee, W. Zhang, J. S. Zuback, G. L. Knapp, A. De, and T. DebRoy. 2021. “Mechanistic Models for Additive Manufacturing of Metallic Components.” *Progress in Materials Science* 116. https://doi.org/10.1016/j.pmatsci.2020.100703.

Westphal, E., and H. Seitz. 2025. “Porosity and Density Measurement of Additively Manufactured Components: A Comparative Analysis of Measurement Methods across Processes and Materials.” *Materials Science in Additive Manufacturing* 4 (2). https://doi.org/10.36922/msam025090010.

Wood, P., T. Libura, Z. L. Kowalewski, G. Williams, and A. Serjouei. 2019. “Influences of Horizontal and Vertical Build Orientations and Post-Fabrication Processes on the Fatigue Behavior of Stainless Steel 316l Produced by Selective Laser Melting.” *Materials (Basel)* 12 (24). https://doi.org/10.3390/ma12244203. PMCID: PMC6947212.

Xiao, W., Y. Liu, J. Huang, S. Zou, Z. Ren, S. Liu, and Y. Wang. 2025. “Process Parameter Optimization for Laser Directed Energy Deposition B4c/Al Neutron Absorbing Material Via Taguchi Method.” *Optics & Laser Technology* 184. https://doi.org/10.1016/j.optlastec.2025.112507.

Zhang, M., C.-N. Sun, X. Zhang, P. C. Goh, J. Wei, D. Hardacre, and H. Li. 2017. “Fatigue and Fracture Behaviour of Laser Powder Bed Fusion Stainless Steel 316l: Influence of Processing Parameters.” *Materials Science and Engineering: A* 703: 251-261. https://doi.org/10.1016/j.msea.2017.07.071.

Zhang, X., Y. Chen, S. A. Mantri, L. Gao, E. Listwan, J. Listwan, M. McMurtrey, N. Mohale, and C. Massey. 2024a. *Fy24 Integrated Results for High-Temperature Mechanical Testing of Lpbf 316h Stainless Steel.* Argonne National Laboratory (ANL), Argonne, IL (United States). Center for Nanoscale Materials (CNM); Idaho National Laboratory (INL), Idaho Falls, ID (United States); Oak Ridge National Laboratory (ORNL), Oak Ridge, TN (United States) United States. https://www.osti.gov/biblio/2447990

https://www.osti.gov/servlets/purl/2447990.

Zhang, X., S. A. Mantri, G. I. Vukovic, J. Listwan, D. Rink, and E. Listwan. 2023. *Development of Process Parameters and Post-Build Conditions for Qualification of Lpbf 316 Ss.* Argonne National Laboratory (ANL), Argonne, IL (United States) United States. https://www.osti.gov/biblio/2005163

https://www.osti.gov/servlets/purl/2005163.

Zhang, X., M. D. McMurtrey, L. Wang, R. C. O'Brien, C.-H. Shiau, Y. Wang, R. Scott, Y. Ren, and C. Sun. 2020. "Evolution of Microstructure, Residual Stress, and Tensile Properties of Additively Manufactured Stainless Steel under Heat Treatments." 72. https://doi.org/10.1007/s11837-020-04433-9

Journal Name: JOM. Journal of the Minerals, Metals & Materials Society; Journal Volume: 72; Journal Issue: 12. PMCID: Sponsor Org.: Idaho National Laboratory - Laboratory Directed Research and Development (LDRD); USDOE Office of Science (SC), Basic Energy Sciences (BES). Scientific User Facilities Division; USDOE Office of Nuclear Energy (NE).

Zhang, Z., P. Mativenga, W. Zhang, and S. Q. Huang. 2024b. "Deep Learning-Driven Prediction of Mechanical Properties of 316l Stainless Steel Metallographic by Laser Powder Bed Fusion." *Micromachines (Basel)* 15 (9). https://doi.org/10.3390/mi15091167. PMCID: PMC11434083.

Zhou, C., J. Wang, S. Hu, H. Tao, B. Fang, L. Li, J. Zheng, and L. Zhang. 2020. "Enhanced Corrosion Resistance of Additively Manufactured 316l Stainless Steel after Heat Treatment." *Journal of The Electrochemical Society* 167 (14). https://doi.org/10.1149/1945-7111/abc10e.

Pacific Northwest National Laboratory

902 Battelle Boulevard
P.O. Box 999
Richland, WA 99354

1-888-375-PNNL (7665)

www.pnnl.gov